Characteristic low-temperature behaviors and grain boundary state of FCC nanocrystalline metals

Terigele Xi

February 2018

Characteristic low-temperature behaviors and grain boundary state of FCC nanocrystalline metals

Terigele Xi

Doctoral Program in Materials Science

Submitted to the Graduate School of

Pure and Applied Sciences

In Partial Fulfillment of Requirements

for the Degree of Doctor of Philosophy in

Engineering

at the

University of Tsukuba

TABLE OF CONTENTS

Chapter 1 General Introduction

1.1 Polycrystalline and nanocrystalline materials

Most metallic materials are polycrystalline and crystallites with different crystallographic orientations are consolidated in polycrystalline (*p*-, here after) materials. The size of the crystallites (grain size) in *p*-metals is typically larger than ~1 μm. At the interfaces between two adjacent crystallites in *p*-materials, the atoms lost the long-range periodic order in order to accommodate the misfit between the crystallites with different orientation. These types of interfaces are called "grain boundaries" (Fig. 1-1). The segment shared by three crystallites is a "triple junction". The thickness of grain boundary in *p*-metals is believed to be a few atomic distance [1]. In *p*-materials, the volume fraction of grain boundaries is negligible small (see Fig. 1-1). Except for several phenomena such as the grain boundary segregation and grain boundary corrosion, the role of grain boundaries on the macroscopic properties can be ignored because of the negligible small amount. When the grain size decreases, the volume fraction of grain boundaries as well as the triple junctions increase and go beyond a few percent at the grain size below 100 nm as shown in Fig. 1-1. It is expected that the effect of the grain boundaries is reflected on the macroscopic properties such as the fine-grained *p*-materials. Hence *p*-materials with the grain size of below ~100 nm are called nanocrystalline (*n*-, here after) materials [2, 3] and are expected to show characteristic properties different from *p*-counterparts. .

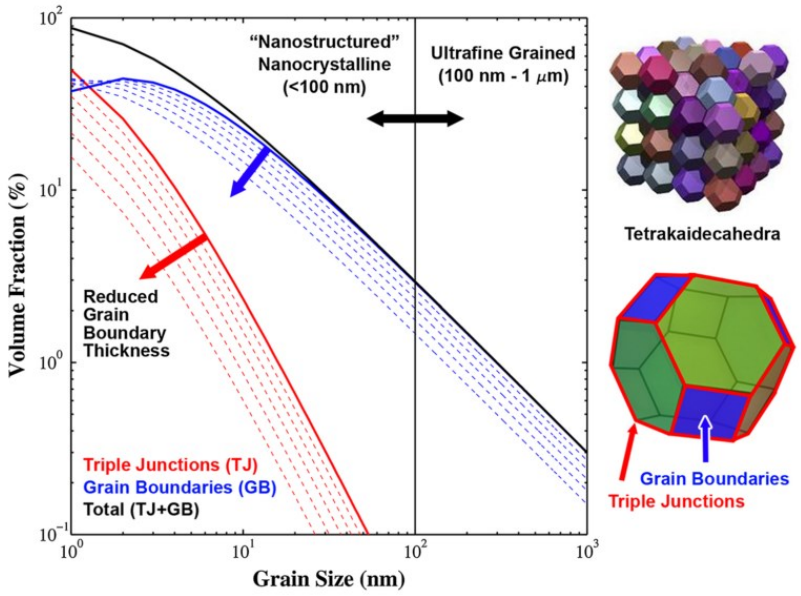

Fig. 1-1. Change in volume fraction of grain boundaries and triple junctions as a function of grain size. The volume fraction is calculated by space-filling of tetrakaidecahedra grains with a grain boundary thickness of 1 nm (thick lines). In the plot, the dotted lines show the results by changing the grain boundary thicknesses from 0.9 nm to 0.5 nm in increments of 0.1 nm [2].

Remarkable scientific works on *n*-materials were studied by Gleiter and the concept and properties of *n*-materials were originally published in 1989 [4]. The two-dimensional model of *n*-materials proposed by Gleiter is shown in Fig. 1-2. Many attentions have been attracted to *n*-materials because of various novel properties different from those of *p*-materials. For example, in the case of *p*-metals, the most prominent and technologically important feature is the increase in strength with reducing the grain size. This behavior is known as the Hall-Petch relation. The strength and hardness much higher than those of the *p*-counterparts were reported for *n*-metals [5-7]. However, when the grain size decreased to less than ~15 nm, the increase of strength of *n*-metals showed saturation or even decreased as shown in Fig. 1-3. This phenomenon is called the "inverse Hall-Petch effect". In the dislocation pile-up model for strengthening [5], the population of dislocations in grain decreases with decreasing the grain size, and the number of dislocations piled up near the grain boundary is also decreased. Then the stress accumulation by the dislocation pile-up is not enough for the forefront dislocation to overcome the grain boundary. By further decrease in the grain size below ~15nm, the grain boundary cannot act as the barrier for the dislocations and shear propagation becomes started; it leads to the saturation or even decrease in the strength [8]. In addition to the mechanical properties, *n*-materials exhibit unique properties like the high electrical restively, and so on.

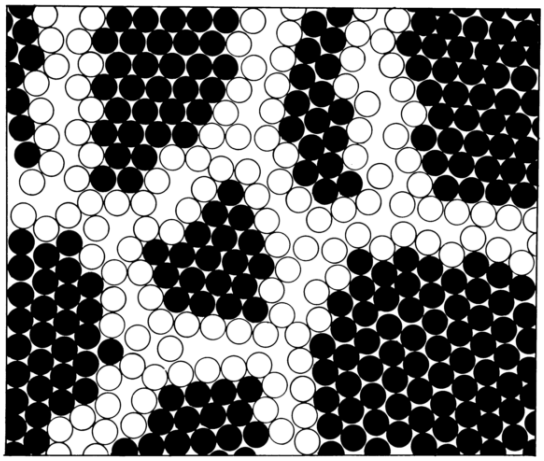

Fig. 1-2. Atomic structure of *n*-material in two dimensional model. The structure was computed by using the Morse potential of gold. Atoms in grain boundaries and those crystalline parts are indicated by filled black and open circles, respectively [4].

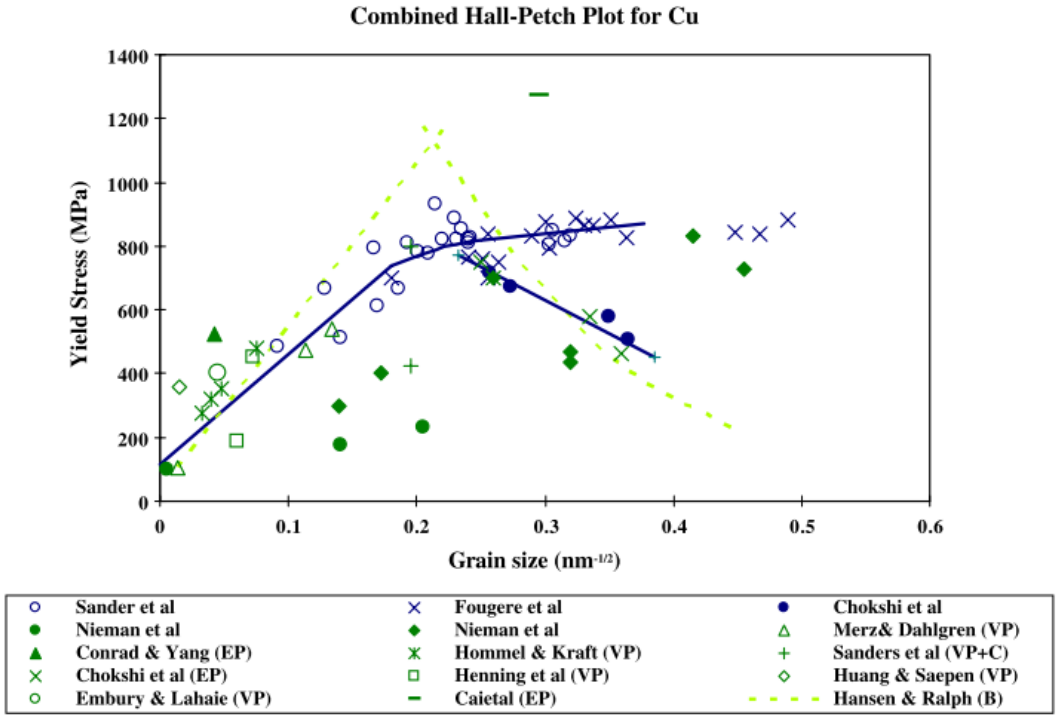

Fig. 1-3. Yield stresses reported for Cu are plotted against the inverse squre root of grain size. The plot suggests that the positive slope turns to zero or negative at the grain size of ~20 nm [2].

1.2 Preparation methods of *n*-materials

The preparation methods of *n*-materials could be classified into two main types, top-down and bottom-up methods [4, 5]. In the top-down method, bulk (coarse-grained) materials are broken down to nanostructures. In the bottom-up method, *n*-materials are prepared by unifying ultrafine particles or building atoms and molecules with nanostructures[5]. The followings are typical examples of the methods:

High-energy ball milling is a method to reduce the grain size by severe plastic deformation induced by milling[5, 9]. Coarse-grained power samples are strongly milled by using hard balls and the grain size decreases with the ball milling time. The bulk samples can be formed from nanocrystalline powders by compaction. It is simple and easy, however, impurity contaminations from the balls and vessel and residual porosity contained in compacted samples are drawbacks of this method [10].

Severe plastic deformation (SPD) is a method to prepare bulk *n*-materials or ultra-fine-grained materials by severe plastic deformation [10]. The *n*-materials prepared by SPD often contain a large amount of high angel grain boundaries [11, 12].

Crystallization amorphous solid by annealing can yield porosity-free *n*-materials [13]. The prepared nanostructure could be controlled by the annealing condition but the formed nanotexture is restricted by the original amorphous materials. .

Electrodeposition is a method to prepare *n*-metal film on a substrate by electrochemical plating [14]. By controlling the preparation conditions such as the potential and temperature, *n*-materials of pure metals and alloys with the grain size as small as 20 nm can be prepared. The low cost and high production rates are suitable for industrial application [5]. However, the process in the solution may cause contamination by gases and surfactants. Lu et al. prepared *n*-Cu with the unique nano-twined structure by the electrodeposition method in the adequate condition [15].

Inert gas condensation and compaction, in this method, nanoparticles prepared by the inert-gas condensation are compacted to form a pellet of *n*-material. A mother material is evaporated in an inert-gas atmosphere and nanoparticles are formed by condensation of the vapor. The nanoparticles are collected and then compacted to the pellet [4]. This method was widely used in the early stage of studying *n*-materials. It is difficult to obtain the fully dense *n*-materials by mechanical compaction of nanoparticles and tiny pores and cracks were included in the compacted samples [5].

1.3 Grain boundary

As mentioned in section 1.1, *n*-materials show different properties compared with *p*-counterparts because of the much increased volume fraction of the grain boundary regions. It is very important to understand the behaviors of the grain boundaries to investigate the *n*-materials. In the case of *p*-materials, crystal-like nature of the grain boundaries is suggested for some grain boundaries [16]. The grain boundaries in *p*-materials can be divided into two types from the misorientation angel between neighboring two grains, low angle grain boundary (misorientation angel < ~15 degree) and high angle grain boundary (misorientation angel > ~15 degree). The atom arrangement of the low angle grain boundary can be explained by the dislocation model where the dislocations periodically align along the grain boundary (the middle in Fig. 1-5). The atomic structure of the high angel grain boundary was explained by the amorphous cement model in the early state [17], however, contradicted issues were reported from the direct observations by scanning transmission electron microscopy (STEM) [18, 19]. Recently, the structure of the high angle grain boundaries can also be explained by periodic arrangements of structural units (structural unit model[20, 21]).

The grain boundary energy is a function of the misorientation angel. The grain boundaries with higher misorientation angles are often structurally more disordered, but the energy is not always lower for the grain boundaries with smaller misorientation angles. As shown in Fig. 1-4 [22], some drops of the grain boundary energy are existed and the grain boundaries at these angles have specific structures like the twin grain boundary. The sketches of the high angle grain boundary, low angle grain boundary and twin grain boundary are shown in Fig. 1-5 [23]. Further, as mentioned above, the atomic structures of some grain boundaries in *p*-materials show periodicity in the structural units [20, 21].

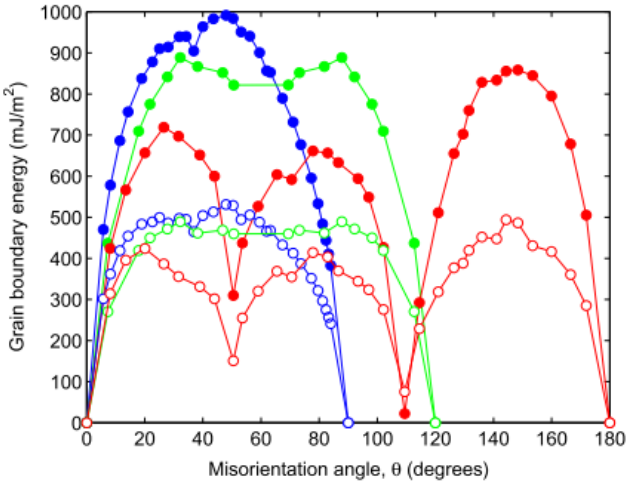

Fig. 1-4. Change in grain boundary energy by misorentation angle. The energy of symmetric tilt grain boundaries was calculated from atomistic computer simulations. The rotation axes of tilt is <100> (blue), <110> (red) and <111> (green) direction. Open and closed circles indicate the results for Al and Cu, respectively [22].

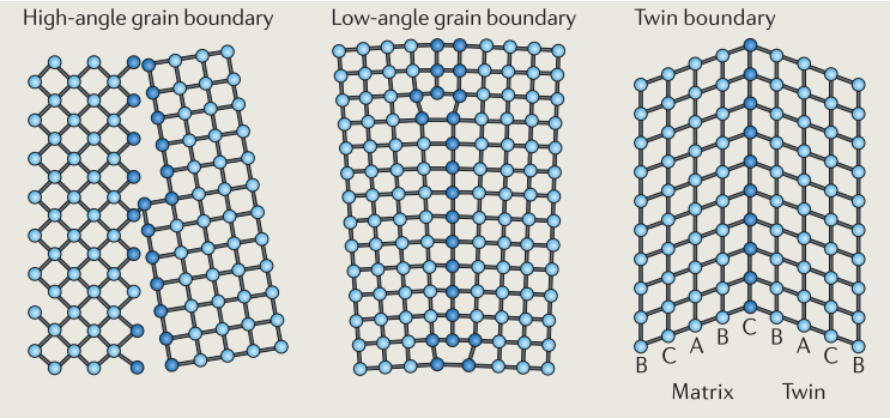

Fig. 1-5. Atomistic sketches of high-angle grain boundary (left), low-angle grain boundary (middle) and twin boundary (right) [23].

The structure or state of grain boundary may depend on the size of the grains and preparation condition [24]. By reducing the grain size, the grain boundary structure would be more complicated because the grain boundaries accommodate the misfits not only the adjacent grains but also neighboring ones. As a consequence, the grain boundaries in *n*-materials become more complicated and unstable than those in *p*-materials. In addition, as described above, the *n*-materials are prepared by various non-equilibrium methods. It results in the increase in the grain boundary energy and more disordered state in the grain boundary regions, or formation of the grain boundary in a "non-equilibrium" state [11, 12].

The atomic structure of grain boundary in *n*-materials has not fully clarified yet. The direct observation of the grain boundaries in *n*-materials could be achieved by TEM and STEM, however, it is pointed out that a grain growth or relaxation are occurred during the sample preparation in [25]. Computer simulation is a powerful technique to investigate the structure and stability of the grain boundaries, provides useful and helpful information of the grain boundaries. From the simulations of *p*-metals, the first-order transition of order-disorder in the grain boundaries below melting point [26] and the reversible structural transformation in Cu Σ5(310) grain boundary [27] were reported. Further, dynamics similar to those of glass-forming liquids was suggested for the grain boundaries in *p*-metals [24]. For *n*-materials, the liquid-like state of grain boundaries was reported for *n*-Si and *n*-metals from the molecular dynamics simulations [28-30]. Although the early model of amorphous cement for high angle grain boundary was not suit for polycrystalline, it may suit for *n*-materials as described from simulation [17]. Recently, the glass transition of grain boundaries was suggested from the confocal optical microscope observation of colloidal crystals with the diameter of 600 nm [31]. However, no experimental results have been reported to support the amorphous state or glass-like characters of the grain boundaries in metals.

The properties of *n*-materials can be governed by the grain boundary structure. Controlling the property by altering the grain boundary structure is named as "grain boundary engineering" [32].

Lu group reported that *n*-Cu with nanotwinned structure synthesized by pulsed electrodeposition method exhibited ultrahigh strength (about 10 times higher than that of conventional Cu) and high electrical conductivity [15]. The energetically stable twin boundary blocked the dislocation motion effectively leading to the strengthening [23]. They also reported that the hardness of *n*-alloy in Ni-Mo system was increased by grain boundary stabilization and Mo segregation [33].Therefore, the study of grain boundaries of *n*-materials is very important to understand the noble properties of *n*-materials and to expand the application field of *n*-materials.

1.4 Research background

As mentioned in section 1.3, the direct observation of the grain boundaries in *n*-materials is very difficult. On the other hand, the characteristic behaviors of the grain boundaries were indirectly detected from various experiments.

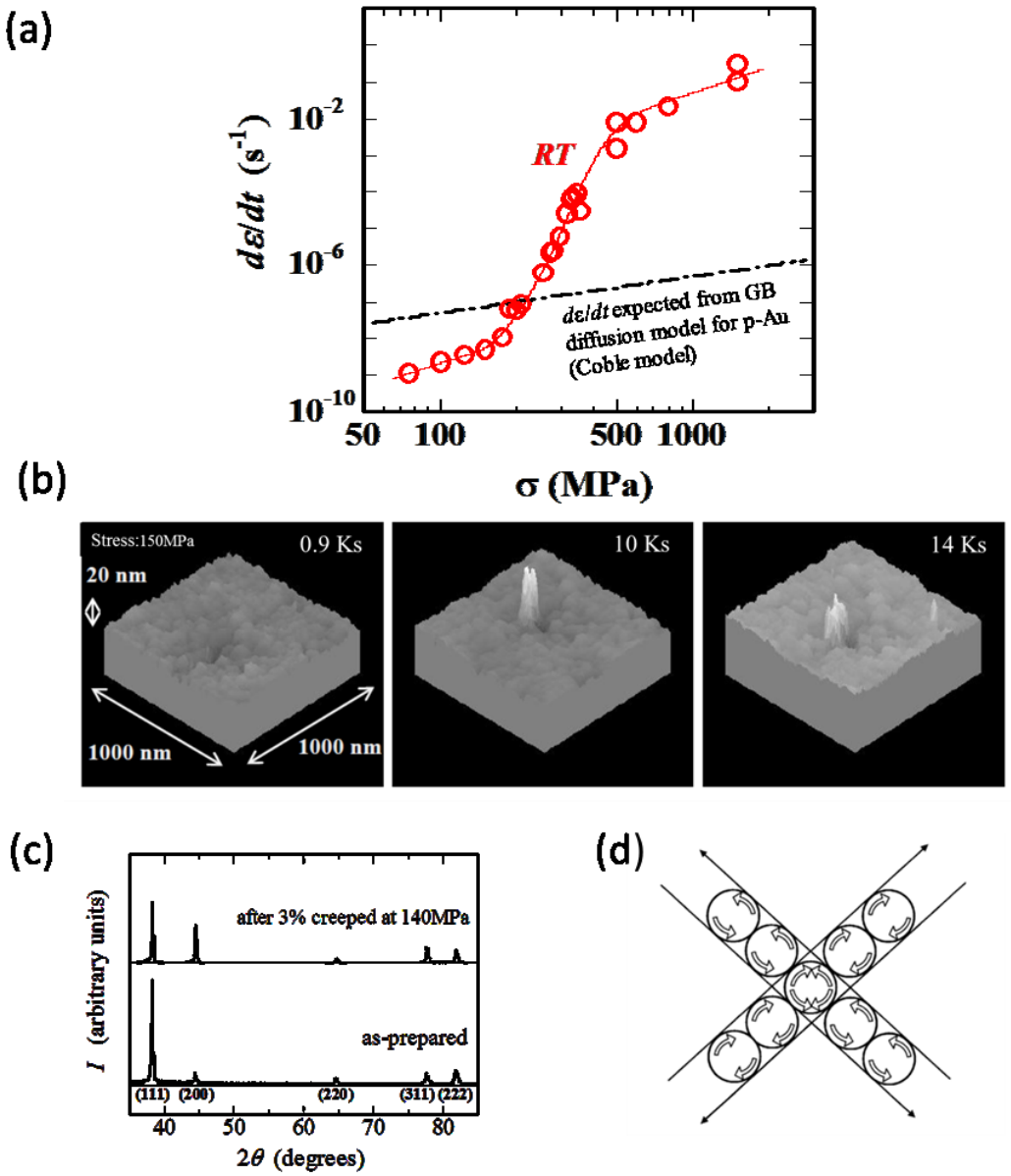

Fig. 1-6. (a) Steady-state creep rate observed for *n*-Au as a function of stress. The dash line is theoretical value for *n*-Au with the mean grain size of 35 nm predicted by Coble's model at room temperature [40]. (b). *In situ* STM images of *n*-Au observed during creep test at 150 MPa after 0.9 Ks, 10 Ks and 14 Ks [40]. (c) XRD patterns observed for *n*-Au in as-prepared state and after creep deformation of 3% at 140 MPa [34]. (d). Model of grain-boundary slips associated with grain rotations and anchoring due to crossing of slips [34].

Yagi et al. [34] conducted the creep test for *n*-Au at room temperature. Fig. 1-6 (a) shows the creep rate as a function of applied stress. When the applied stress above ~30 MPa, creep deformation started. From ~200 MPa, the creep rate increased sharply. The increase of creep rate from ~150 MPa was attributed to the creep deformation caused by the grain boundary slips. The creep rate that predicted from the coble model that used for the grain boundary diffusion in *p*-Au is depicted in Fig. 1-6(a) [35]. Furthermore, Fig. 1-6 (b) shows the in-situ STM observation of *n*-Au during creep. Some grains moved up from the surface then sunk to the surface level after 4 ks. During such motion, the grains were still connected with each other and the *n*-structure was maintained. On the other hand, the strongly (111) preferred orientation after deformation turned to the random orientation, but no grain growth was observed (Fig. 1-6 (c)). These observations suggested that above ~150 MPa, the grain boundaries become viscoelastic and the creep deformation progresses by sliding of grains with rotational motion as shown in Fig. 1-6 (d).

The change in the grain boundary state by temperature was also reported from the internal friction measurement (details will be discussed in Section 2.3.1). For internal friction due to the grain boundary in *p*-metal, a pioneer work was conducted by Kê at 1947. He measured the internal friction of *p*-Al and single crystalline Al. As shown in Fig. 1-7, an internal peak was observed in *p*-Al at around 563 K but not in single crystal Al. The origin of this peak was attributed to the grain boundary sliding motion, in other words, the viscous nature of the grain boundary [36].

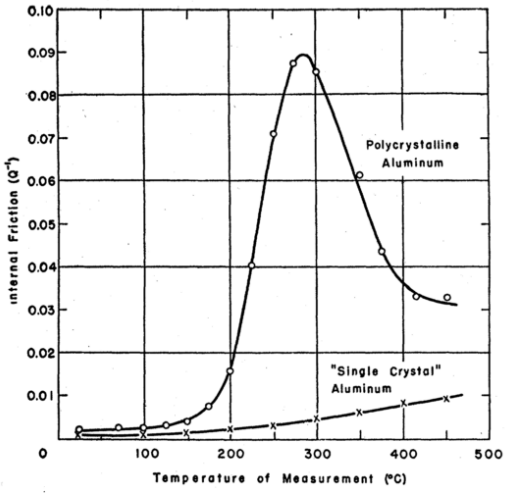

Fig. 1-7. Internal friction as a function of temperature observed for polycrystalline and single crystal aluminum [36].

For *n*-Au, it was reported that the internal friction showed an anomalous large increase above 200 K ($Q^{-1}_{>200K}$) as shown in Fig. 1-8 [37]. It was found that $Q^{-1}_{>200K}$ was repeatedly observed for cool-down and warm-up below 350 K but the amount decreased with grain growth after heating above 350 K. Furthermore, the Young's modulus of *n*-Au decreased above ~200K [38]. These observations suggested that some anelastic process of grain boundaries was thermally activated

above ~200 K in *n*-Au [39]. An endothermic tendency of *n*-Au compared with *p*-Au was reported above ~200 K [40] and it disappeared after grain growth. These results indicate that the grain boundaries of *n*-Au turned from elastic to anelastic or viscoelastic states above ~200 K. As mentioned before, the state change or phase transformation in grain boundary was predicted from the computer simulation [26, 41], however, the state change in the grain boundaries in *n*-metals has not been established experimentally yet.

As mentioned before, the property and behavior of the grain boundary was varied by the preparation condition. As shown in Fig. 1-8, *n*-Au prepared by the gas deposition method (see 2.1) showed different internal friction spectra. In the figure, type-H was prepared at higher deposition rate of the nanoparticles and type-L at lower deposition rate. This result indicated that the grain boundary state is varied by the preparation condition.

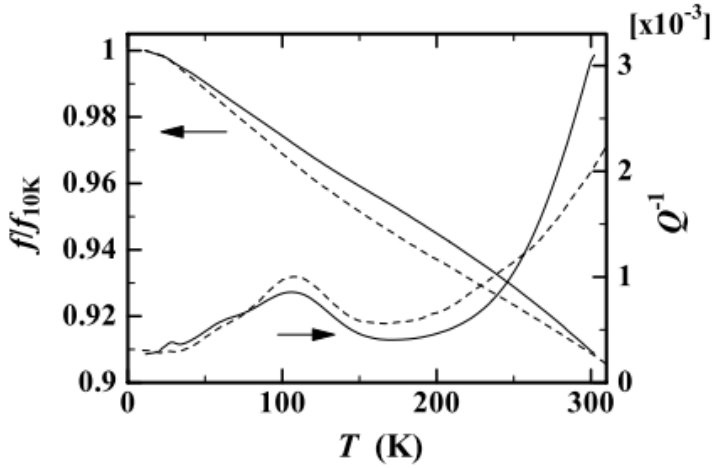

Fig. 1-8. Temperature spectra of the internal friction observed for type-L *n*-Au (dashed lines, f_{10K}=340 Hz) and type-H *n*-Au (solid lines, f_{10K}=400 Hz) [37]. For details, see text.

1.5 Purpose

As mentioned above, if $Q^{-1}_{>200K}$, the rapid increase in internal friction observed for *n*-Au above 200 K, reflects a state change in the grain boundaries from ideal elastic to anelastic or viscoelastic, corresponding variations are also expected for other physical properties. For the state change in the grain boundaries, the reversible structural transition by temperature was suggested from several computer simulations. Further, amorphous nature or glass-like behavior of the grain boundaries were also reported from the computer simulations. However, no experimental results have been reported to support the amorphous state or glass-like characters of the grain boundaries in metals. On the other hand, it was observed that two types of *n*-Au prepared by the gas-deposition method with different deposition rate exhibited slightly different in textures, thermal stabilities and anelastic properties. Therefore, the purpose of the present study is (1) to understand the behavior of the grain boundaries in *n*-metals below room temperature and (2) to clarify the effect of the deposition rate on texture and grain boundary state of *n*-metals prepared by the gas deposition method. Anelastic, electrical and thermal experimental measurements for different types of *n*-Au and *n*-Ag will be conducted in this study.

This thesis is comprised of five chapters. In Chapter 1, a background of *n*-materials and previous results of *n*-metals are explored. Chapter 2 shows the experimental methods used in the present study. Chapter 3 is devoted to the observed experimental results. In Chapter 4, the glass transition like behavior of grain boundary and the effect of the deposition rate on texture and various properties are discussed from the experimental results. Finally, the conclusion is presented in Chapter 5.

Chapter 2 Experimental procedures

2.1 Gas deposition method

N-materials can be fabricated by various methods as introduced in Chapter 1. For studying the intrinsic properties of grain boundary of nanocrystalline, it is necessary to fabricate the *n*-sample with high purity and high density. In the present study, *n*-samples with high density and high purity were prepared by gas deposition method. Details of gas deposition apparatus will be illustrated below.

2.1.1 Gas deposition apparatus

The schematic figure of gas deposition apparatus is shown in Fig. 2-1. The gas deposition apparatus is mainly consisted of a deposition chamber, an evaporation chamber, a He gas purification system, and an evacuation system. The deposition and evaporation chambers are connected by a thin tube (transfer tube).

Before the sample preparation, the two chambers were evacuated to a high vacuum ($<10^{-5}$ torr) by using a turbomolecular pump (TMP) over 10 hours to eliminate residual gases. In addition, the transfer tube and carbon crucible in evaporation chamber were heated in vacuum. In the gas deposition method, the ultrafine metal nanoparticles are prepared in the helium atmosphere and the nanoparticles are deposited on a substrate by using helium gas jet flow. To avoid the oxidation and contamination of the nanoparticles, the high purity helium gas was circulated by using the gas purification system. The gas purification system is composed of a physical absorption column (filled with molecular sieves cooled at liquid nitrogen temperature) and a chemical absorption pump (SORB-AC® Cartridge Pump with St 101 getter alloy, SAES Getters). The purity of He gas was monitored by a zirconia oxygen analyzer (Toray), and the oxygen concentration is kept below 0.01 ppm (the purity of He gas is regarded as more than 99.9999%) during the sample preparation. The collected He gas was compressed at ~ 5 atm and then purified.

After the oxygen concentration in He gas became less than 0.01 ppm, the fabrication process of *n*-metals was started. During the fabrication process, the helium pressure of the deposition chamber was maintained at ~0.1 kPa by using a mechanical booster pump (MBP) and a rotary pump. The helium pressure in the evaporation chamber was maintained at ~66.7 kPa by using a rotary pump. In the evaporation chamber, a base metal of gold (99.9999% purity) or silver (99.99999% purity) in a carbon crucible was heated up to high temperature by a high frequency induction heater and metal nanoparticles were formed just above the crucible (similar to inert-gas condensation method). The lower end of the transfer tube was located about 2.5 cm above the crucible and a helium gas jet flow is formed by the pressure difference between the evaporation

chamber (~66.7 kPa) and the deposition chamber (~0.1 kPa). Most of the metal nanoparticles were sucked into the transfer tube and then transferred to the deposition chamber by the helium gas jet flow. Residual nanoparticles which were not sucked into the transfer are eliminated by the exhausting helium gas flow to the rotary pump. The upper end of the transfer tube was located about 2-3 mm below a glass substrate (0.2 mm thick) in the deposition chamber and the metal nanoparticles transferred from the evaporation chamber were directly deposited on the substrate. The glass substrate was set on a computer-controlled X-Y stage made of copper and we can draw a desired figure by the metal nanoparticles within 25×25 mm^2 square. The temperature of the helium gas above the crucible was considerably high and the transfer tube was also heated to avoid stacking of the nanoparticles inside of the pipe. In order to suppress unnecessary grain growth due to the hot helium gas flow, the X-Y stage is cooled by thermally connecting to a cold finger filled with the liquid nitrogen. The substrate temperature measured by a thermocouple was below 260 K during the deposition of the metal nanoparticles. Exhausting He gas in deposition chamber would be recycled by MBP and RP, and then flew to He purification system again for purification and circulated to evaporation chamber. In the present study, ribbon-shaped *n*-Au and *n*-Ag samples were prepared by moving the X-Y stage with the pattern as shown in Fig. 2-2 (moving speed of the stage = ~2-5 mm/s). After preparation, the samples were peeled off form the substrate carefully using the surface tension of water. Samples used in our study were mainly in the ribbon shape with the length of ~20 mm width of ~ 1 mm and thickness of ~ 0.05 mm. Slab-shaped samples with the length of ~9 mm width of ~4 mm and thickness of ~0.073 mm were also prepared for DSC measurement by changing the drawing pattern.

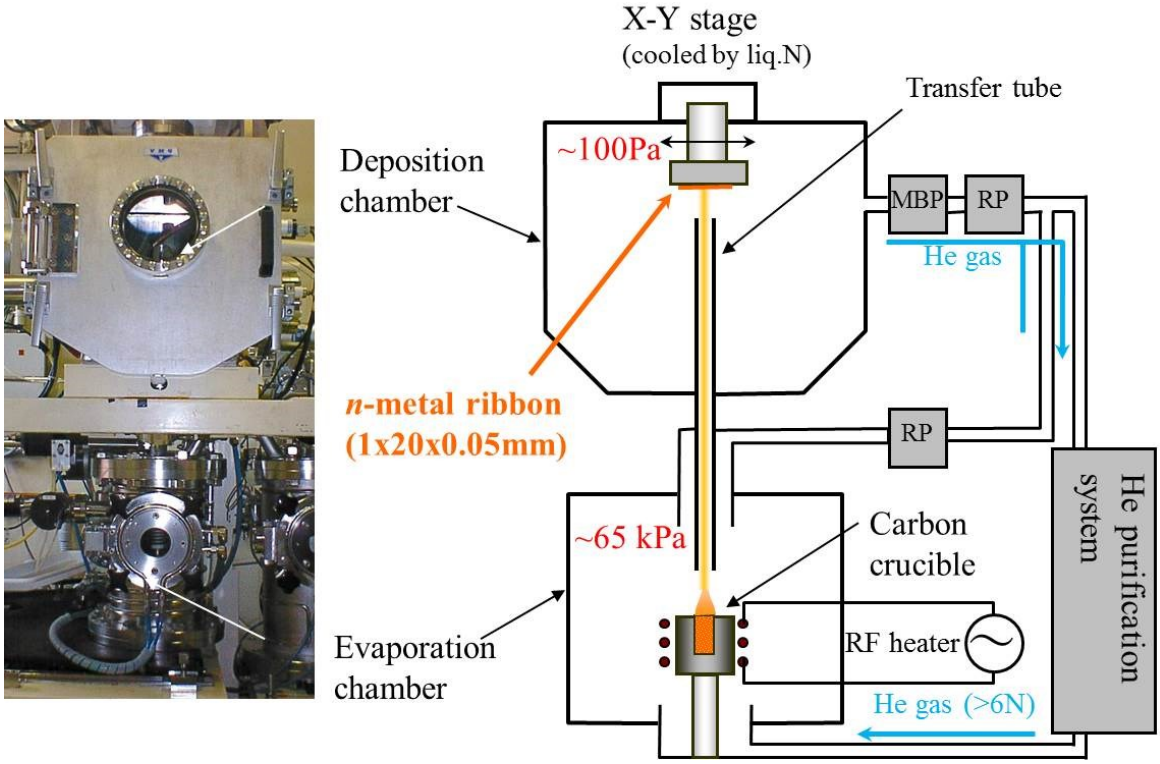

Fig. 2-1. Schematic diagram of gas deposition apparatus (right) and the photograph of deposition chamber and evaporation chamber (left).

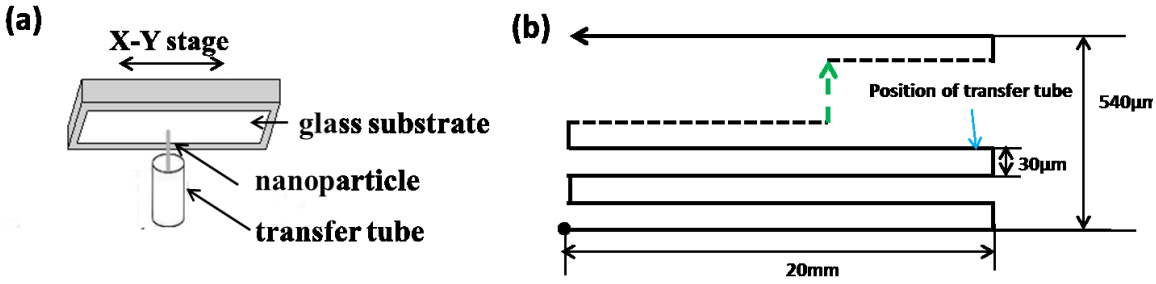

Fig. 2-2. (a) Schematic drawing of the transfer tube, glass substrate and X-Y stage in the deposition chamber. (b) Drawing pattern programed for preparation of ribbon-shaped samples.

2.1.2 Control of deposition rate of nanoparticle by base metal temperature

In the gas deposition method, metal nanoparticles formed by the inert-gas condensation process were directly deposited on the substrate by using He gas jet flow and a nanocrystalline metal film was prepared. The mean grain size and the grain boundary state are important factor for the characteristics of the prepared *n*-metals. The mean grain size was mainly determined by the size of nanoparticles and the grain boundary state depended on the deposition rate of the nanoparticles. In the inert-gas condensation process, the size and formation rate of the nanoparticles are governed by the vapor pressure of the base metal and the pressure of the inert-gas. However, in the gas deposition method, the He gas pressure in the evaporation chamber was maintained to 66.7 kPa in order to generate the He gas jet flow for transfer and deposition of the nanoparticles. The vapor pressure of metals was increased exponentially with the increase of temperature. The vapor pressures of Ag and Au were calculated from the thermodynamic data reported [42]. The relationships between vapor pressure and temperature are illustrated in Fig. 2-3. Fig. 2-4 shows the change in the temperature of silver base metal by the input power to the induction heater. The base metal temperature was measured by using an infrared thermometer. The similar relationship to Fig. 2-4 was reported for the case of gold[43]. In the sample preparation, the base metal temperature was controlled by adjusting the input power to the induction heater.

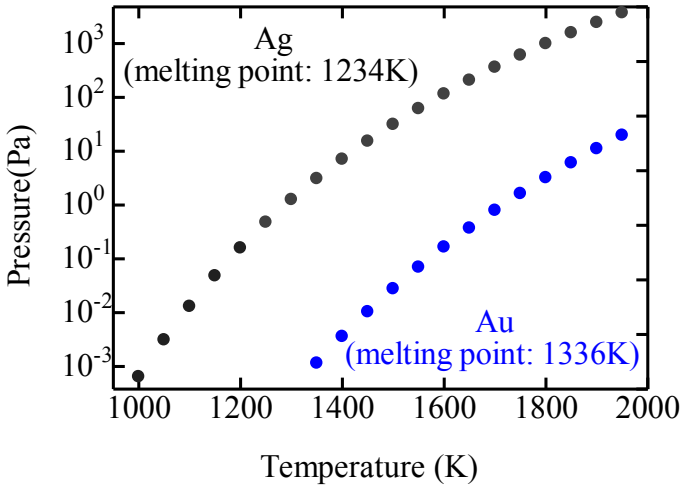

Fig. 2-3. Evaporation pressure of Ag (grey) and Au (blue) as a function of temperature [42].

The deposition rate, defined by the amount of deposited nanoparticle on the substrate in a unit time, is calculated in the following equation;

$$deposition\ rate(nm/s) = \frac{m_{sample}}{\rho_{sample}} / S_{tb}/t_{total}$$

where m_{sample} is the weight of the sample, ρ_{sample} is the density of the sample, S_{tb} is the cross sectional area of transfer tube (π mm^2) and t_{total} is the elapsed time for the sample preparation. The deposition rates of *n*-Au and *n*-Ag as a function of temperature are shown in Fig. 2-5.

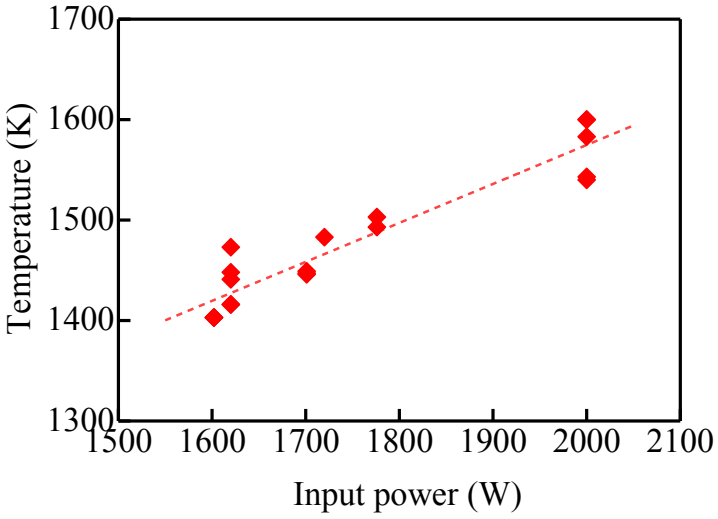

Fig. 2-4. Change in Ag temperature by input power to induction heater.

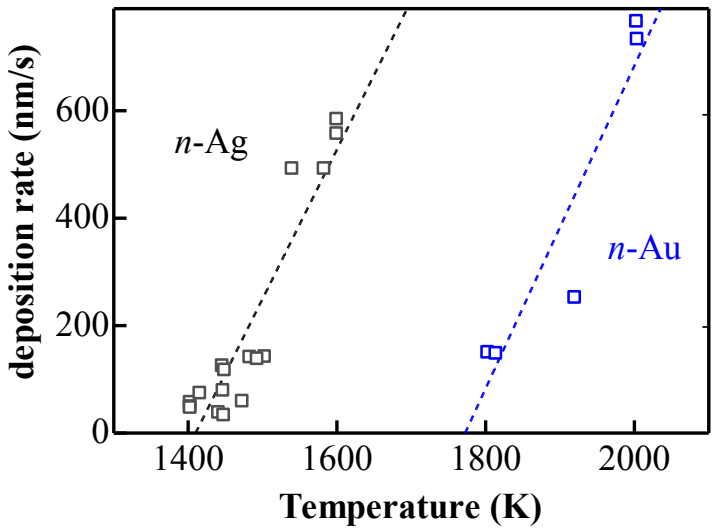

Fig. 2-5. Deposition rate observed for Ag (grey) and Au (blue) as a function of base metal temperature.

2.1.3 Preservation

It was reported that a rapid grain growth of *n*-Pd was occurred at room temperature[44]. For avoiding unnecessary grain growth, the samples were kept in a refrigerator at ~260 K in the early stages of the present study. However, the grain growth was found for some of samples after keeping at ~260 K for more than a few months (see section 3.1.6 for details). In order to prevent the grain growth, the samples were sealed in evacuated quartz tube (~10^{-3} Pa) and then kept in liquid nitrogen.

2.2 Texture analysis

The texture of *n*-samples was investigated by using the X-ray diffraction method. The texture of *n*-samples was investigated by using the X-ray diffraction method. STM was also used to investigate the grain size.

2.2.1 X-ray diffraction (XRD)

The texture such as the grain size, lattice parameter and microstrain was studied by using an X-ray diffractometer (X'PertPro, Phillips) with the CuK_{α} radiation (40 kV, 30 mA). The measurement was performed as the X-ray scattering vector being normal to the specimen flat surface.

The X-ray diffraction pattern was taken in the angle range from 30° to 105°. The position and width of (111), (200), (220), (311), (222) and (400) reflections were determined by the XRD data analyzing software, Jade. The lattice parameter of *n*-metals was estimated from the peak positions by applying Nelson-Riley method [45]. The mean grain size and microstrain were estimated from the peak position and peak width by applying Halder-Wagner method [46]. The details of the analysis are shown in below.

I. Nelson-Riley method

In the diffractometer method, the position of reflection peak will show slight deviation from the true position when the specimen position is misaligned from the 2θ/θ axis along the scattering vector. In Nelson-Riley method, the effect of deviation in the position is corrected by extrapolation to the reflection condition at 2θ=180°. The deviation in the lattice parameter from the true value could be expressed as;

$$\Delta a/a = K\{(\cos^2\theta/\sin\theta) + (cos^2\theta/\theta)\},\ \text{K= const.}$$

where θ is the Bragg angle. The lattice constant estimated from the (hkl) reflection, $a_{(hkl)}\left(= d_{(hkl)}/(h^2+k^2+l^2)^{0.5}\right)$, is plotted against $(\cos^2\theta/\sin\theta) + (cos^2\theta/\theta)$ and the value of a extrapolated at θ=90° indicates the true lattice parameter eliminating the geometrical condition of the sample position.

II. Halder-Wagner method

A broadening of the reflection peak is induced by the decrease in the grain size and the increase in the microstrain of the crystallites. The integral breadth related with small grain size, β^s, can be

expressed by Scherrer equation as;

$$\beta^S = \frac{K\lambda}{Dcos\theta}$$

where K is Scherrer constant (K value as 0.97 used in our study), λ is wave length of X-ray and D is the grain size. The integral breadth due to microstrain, β^D, on the other hand, could be expressed as;

$$\beta^D = 4\varepsilon \cdot \tan\theta$$

where ε is the root mean squre of microstrain. When both the small grain size and the microstrain are contributed to the peak broadening, the observed integral breadth β could be expressed as;

$$\frac{\beta^S}{\beta} = 1 - \left(\frac{\beta^D}{\beta}\right)^2$$

$$\left(\frac{\beta}{tan\theta}\right)^2 = \frac{K\lambda}{D} \cdot \frac{\beta}{tan\theta sin\theta} + 16\varepsilon^2$$

When $(\beta/\tan\theta)^2$ is plotted against $\beta/\tan\theta \sin\theta$ and a straight line is determined, the grain size could be obtained from the slope and microstrain from the intercept.

III. Low-temperature X-Ray diffraction measurement

The lattice parameter reflected the dimension of unit cells in a crystal lattice. Lattice parameter exhibits a contraction with decreasing temperature and expansion with increasing temperature. In order to clarify the low temperature characteristic properties of *n*-metals, the XRD measurement at 50 - 300 K was conducted by using the beamline 8A or 8B at the Photon Factory, KEK.

The ribbon-shaped sample was cut into small triangle chips and glued on a quartz rod (Ø: 1mm). The sample was set on the Gonio stage and cooled down by spraying cold helium (or nitrogen) gas. The temperature could be controlled in the range between ~50 - 300 K. The energy of X-ray was set to 11 keV and the reflection pattern was taken by a 2D imaging plate (Debye-Scherrer camera). The exposure time was typically 3 min and the sample was rotated along the omega axis by 3° during the X-ray exposure. The observed Debye-Scherrer ring was converted to the one-dimensional pattern (Fig. 2-6).

In order to obtain the accurate wave length, the diffraction ring of CeO_2 power was measured at room temperature and the converted 1D pattern was analyzed by Nelson-Riley method. The literature value of 5.411102 Å [47] was used for the lattice parameter of CeO_2. Furthermore, the lattice parameters of the *n*-samples were estimated by applying Nelson-Riley method to the reflection peaks.

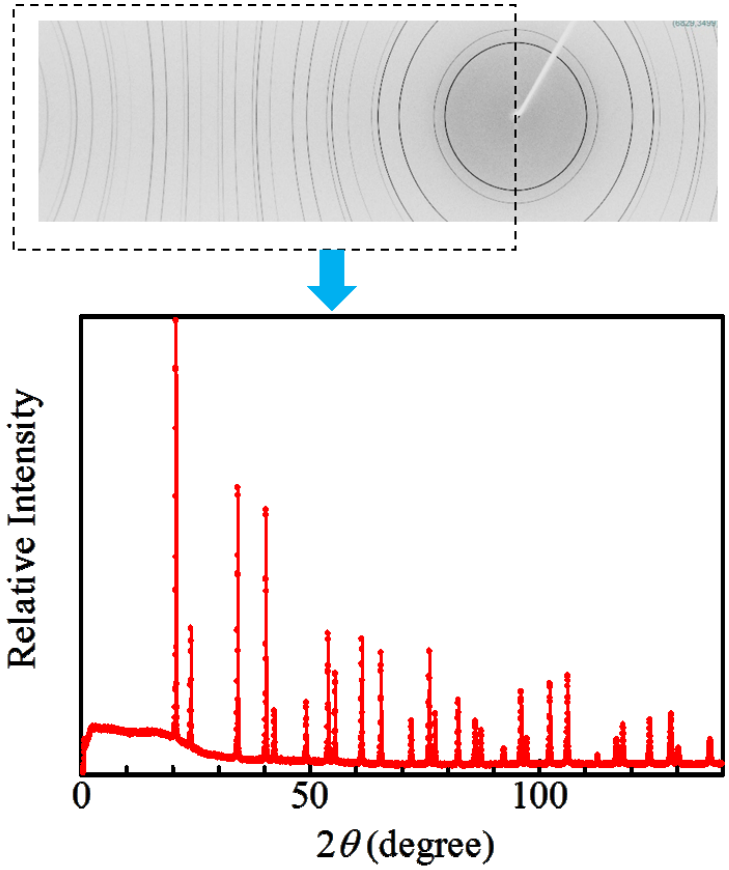

Fig. 2-6. Debye-Scherrer ring (up) and converted one-dimensional XRD pattern (bottom) of CeO_2.

2.2.2 Density

The density of *n*-sample was measured by Archimedes method. The weight of sample was once measured in the air and it was recorded as the dry weight (M_D). Then the sample was hanged on a tiny and thin quartz hook (diameter= ~10 μm) and immersed in ethanol (purity 99.5%). The total weight of the sample and the quartz hook in ethanol was measured and recorded as the wet weight (M_W). Finally, the weight of only the quartz hook in ethanol was measured and recorded as the hook weight (M_H). These measurements were conducted at 293 K.

The volume of the sample is calculated by the follow equation;

$$V_{sample} = \{M_D - (M_W - M_H)\}/\rho_{ethanol}.$$

The density of the sample could be estimated by the follow equation;

$$\rho_{sample} = M_D/V_{sample}.$$

The weight of the sample used for the density measurement was about 20 - 40 mg. It is noted that the density measured for *p*-Au of about 10 mg was agreed with the literature value (19.3 g/cm^3) within 1% accuracy.

2.3 Measurement

2.3.1 Internal friction

When a constant stress is applied to solid materials within the elastic limit, they show not only an instantaneous elastic deformation but also a time-dependent deformation. The amount of the latter is specific for the material and the time-dependent elastic behavior is called anelasticity. When the alternating stress is applied to the anelastic material, a part of the elastic energy is dispersed. If the alternating stress is switched off, the vibration of the materials would decrease in passing time (free decay of the vibration). In this case, the ratio of the dispersed energy against the elastic stored energy per one cycle is defined as "internal friction", Q^{-1};

$$Q^{-1} = \Delta W / 2\pi W$$

where W is the elastic stored energy and ΔW is the dispersed elastic energy [48]. Since structural changes such as atomic movements and structural transitions in solid can be reflected on the anelasticity, the internal friction measurement is considered as a powerful tool to investigate the behaviors of lattice defects.

There are several techniques to measure internal friction [49]. In our study, internal friction was measured by using flexural resonant vibration excited by electrostatic technique. An electrostatic force was applied to the reed-shaped sample in order to excite the resonant vibration. After switching of the electrostatic force, the free decay of the reed vibration is monitored and internal friction was calculated from the logarithmic decrement of vibration amplitude, A;

$$A_t = A_0 exp(-\delta \cdot f_0 t) exp(i\omega_0 t),$$

where A_0 and f_0 are the vibration amplitude and frequency at resonance, respectively, ω is the circular frequency, δ is the logarithmic decrement. The logarithmic decrement δ is determined as:

$$\delta = \ln(A_m / A_{m+1}),$$

where A_m and A_{m+1} are the vibration amplitudes in the m th and m+1 th cycles. Then, internal friction calculated from δ as;

$$Q^{-1} = \delta / \pi$$

$$= \ln(A_m / A_{m+1}) / \pi.$$

The resonant frequency is the function of the dynamic modulus and shape of the sample;

$$f = (0.1614t/L^2) \cdot \sqrt{(E/\rho)}$$

where L, t, ρ and E are the length, thickness, density and dynamic Young's modulus of the sample, respectively.

In the internal friction measurement by the electrostatically excited technique, a direct voltage, V, is imposed in addition to the alternating driving force. The apparent resonant frequency is changed by V in the following equation;

$$f/f_0 = 1 - \alpha V^2.$$

The real resonant frequency could be estimated by extrapolation of the frequency to V=0 in the V^2-f plot. The schematic drawing of the internal friction measurement in the present study is shown in Fig. 2-7. The ribbon-shaped *n*-metal sample was cut into a reed specimen with the length of 5-8 mm, the width of ~2 mm. As shown in Fig. 2-8, one end of the reed specimen was clamped by U-shaped *p*-Au film (thichness of ~0.06 mm) and then fixed on a copper specimen holder by a copper band. In order to hold the reed specimen rigidly, an L-shaped stainless steel fitting was used. After the *n*-specimen was mounted on Cu bed for the internal friction measurement, the electrode position was adjusted as the distance between the specimen and electrode at 0.1- 0.5 mm. An electrostatic force was applied to the reed specimen by adding the alternating drive voltage to the electrode, and the resonant vibration of the reed with a constant amplitude was excited by a positive feedback system where the amplitude and phase of the drive voltage was controlled by an automatic-gain-controlled amplifier. The thickness and length of the reed specimen was adjusted as the resonant vibration with the frequency being 100 Hz to 2K Hz. The vibration of the reed specimen was monitored through the change in the capacitance between the electrode and the reed specimen due to the displacement. The electrode was connected to the one end of a cavity resonator of which the resonant frequency was tuned to be about 100 MHz. A VHF transmitter with the oscillating frequency of ~100 MHz (carrier wave) was connected to another end of the cavity resonator. When the distance between the reed and electrode was changed, the frequency of the carrier wave was modulated through the change in the capacitance (frequency modulation (FM) of the carrier wave). Then, the vibration of the reed was monitored by a FM receiver and the resonant frequency of the reed specimen was recorded. In the internal friction measurement, the driving voltage for the resonant vibration excitation was cut off and the free decay curve of the vibration was monitored. The vibration of the reed specimen was converted to digital data by a high-speed A/D converter and the data were analyzed by a computer. The temperature of the reed sepcimen was monitored by a copper-constantan thermocouple attached near the Cu specimen holder. The Cu bed with the specimen was put into a cryostat and evacuated below 10^{-6} Torr during the internal friction measurement. In order to cool down the specimen, He gas was filled into the cryostat (~200 Torr) and the outside of the cryostat was cooled by liquid He or liquid nitrogen. When the

temperature reached to the desired temperature, the He gas was evacuated and made the chamber in vacuum again. Then the specimen was warmed up by using an electric heater.

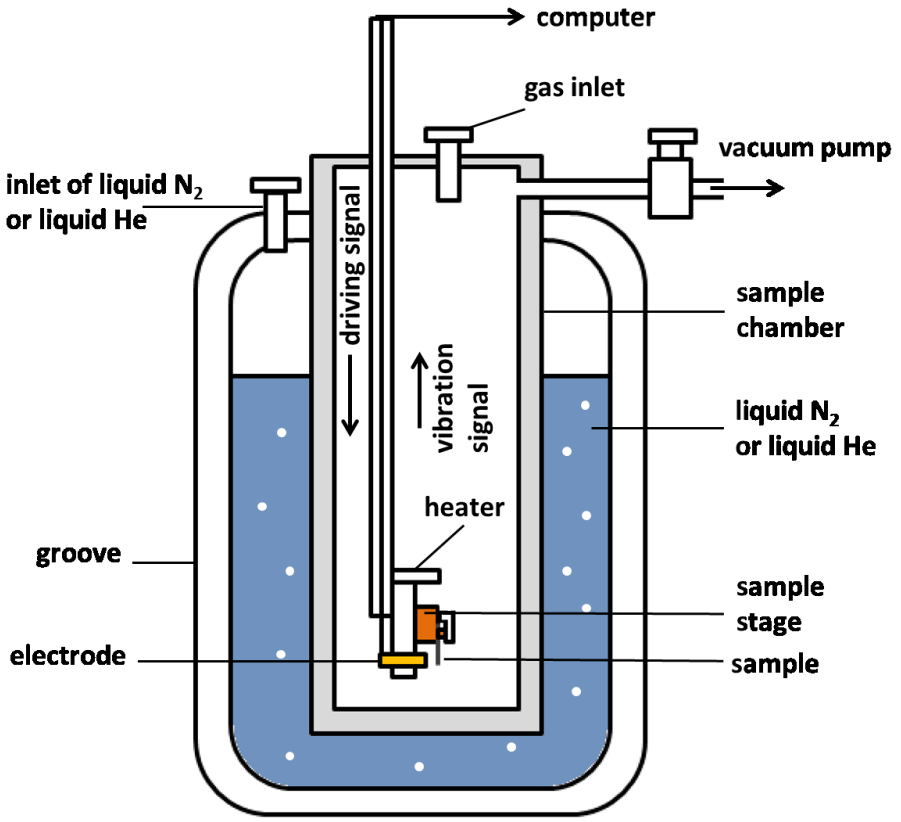

Fig. 2-7. Schematic drawing of the measurement apparatus of internal friction.

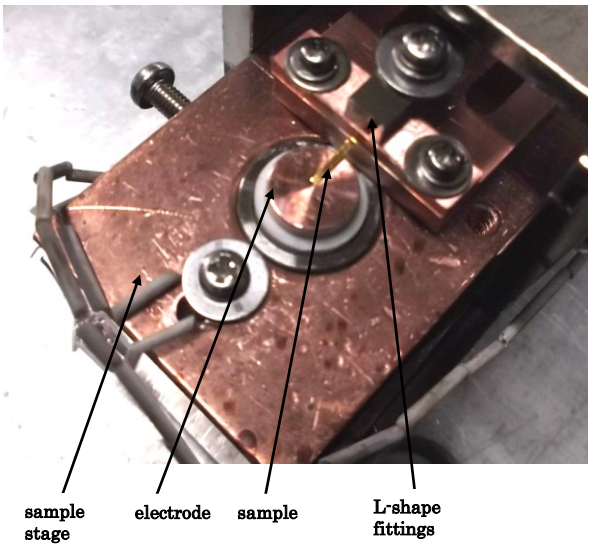

Fig. 2-8. Photograph of the *n*-Au reed specimen fixed on the Cu specimen holder. The Cu specimen holder is mounted on the Cu bed with the electrode for the excitation/detection of the specimen vibration.

2.3.2 Electrical resistivity

Free electrons in metals are scattered by lattice defects and behaviors of the lattice defects sometimes are reflected on the electrical resistivity of metals. In the present study, the electrical resistivity of *n*-metals was measured by the four-terminal method. Thin cooper wires (ϕ 0.1 mm) were attached on the sample by using epoxy-based silver paste. The temperature of the sample was measured by thermocouple which was fixed on the stage. The electrical resistivity was measured at a current of 100-200 mA in a vacuum chamber ($<10^{-2}$ Pa) at the temperature range between 50 and 300 K.

The electrical resistivity was calculated from the equation listed below:

$$\rho = R\frac{\mathrm{H} \times \mathrm{D}}{l}$$

where l is distance between the voltage terminals, H and D is the thickness and the width of sample, respectively. The size of the sample was measured from the optical microscope observation. The values of l, H and D used in our study were 3-5 mm, ~100 μm and 1-2 mm, respectively.

2.3.3 DSC

When a material shows a phase transition at a certain temperature, anomalies could be observed in the heat flow. The differential scanning calorimetry (DSC) is a sensitive and powerful technique to investigate phase or structural changes of the materials. In the present study, a heat-flux DSC (X-DSC7000, Seiko Instruments Inc.) was used. The DSC measurement was performed from 140 to 300 K. During the measurement, Ar gas was supplied to the sample chamber with the flow rate of 50 ml/min and Ar gas cooled by liquid N_2 was used to cool the sample. The sample was cut into small pieces and set in an aluminum pan carefully not to overlap the small sample pieces. The total weight of the sample pieces was ~ 5 mg. The heating and cooling rates were 20 K/min.

Chapter 3 Results

As mentioned in Chapter 1, characteristic property changes at low temperatures were reported for *n*-Au. In order to clarify whether these characteristic changes are common for *n*-FCC metals, we prepared *n*-Ag by using gas deposition method and measured various properties. It was also reported that two types of *n*-Au were prepared with the difference deposition rate. Similarly, in the case of *n*-Ag, two types of samples were prepared by the change in the deposition rate; samples prepared at the deposition rate below ~200 nm/s (type-L) and those above ~400 nm/s (type-H). The characteristics of *n*-Ag and *n*-Au samples used in the present study are listed in Table 3-1. The experimental results of texture, anelastic property, thermal property and electrical property will exhibit in this chapter.

Table 3-1. Characteristics (grain size, lattice variation, microstrain and relative density to the *p*-counterpart (*p*-Au: 19.3 g/cm^3; *p*-Ag: 10.5 g/cm^3) and deposition rate of *n*-Ag and *n*-Au prepared by the gas deposition method. In order to clear, specimens were classified by Ag and Au, where initial capitals "S" and "G" mean Ag and Au, and the last capitals "H" and "L" mean type-H and type-L, respectively.

sample		*d*(nm)	$\triangle a/a_0$(%)	Microstrain (%)	ρ/ρ(%)	Deposition rate (nm/s)
n-Ag	S1L	29	-0.019	0.01	1.00	59
	S2L	33	-0.032	0.2	1.0	142
	S3L	31	-0.04	0.06±0.01	0. 95±0.04	80
	S4L	30	-0.005	0.12	0.96±0.04	74
	S5L	20	-0.07	0.102	0.97±0.03	201
	S5L*	70	0.05	0.03		
	S6L	34	-0.14	0.12	0.98±0.02	124
	S7H	26	-0.02	0.04	0.99±0.01	722
	S8H	28	-0.05	0.09	0.98±0.02	517
n-Au	G1L	28±2	-0.13±0.02	0.1±0.01	0.98±0.02	202
	G2L	31	0.006	0.12	0.99	150
	G3L	48	-0.008	0.037	0.98	169
	G4L	31±1	-0.02	0.09±0.01	1.00±0.01	161
	G5L	38	-0.094	0.082	0.98	215
	G6L	36	-0.07	0.14	0.99	271
	G7L	40±2	0.018	0.07±0.01	1.01±0.01	112
	G7L†	55±2	0.08	0.04		
	G8L	32	0.02	0.12	0.99	231
	G9H	31	0.014	0.01	0.99	1500
	G10H	29	-0.05	0.038	0.98	766
	G11H	31	-0.015	0.03	0.99	388

*: annealing at 700K for 3 h. †: annealing at 923K for 30 min

3.1 Texture of *n*-Ag and *n*-Au, and effect of the deposition rate

3.1.1 (111) preferred orientation in the as-prepared state

Ribbon-shaped *n*-Ag samples were deposited on a glass substrate and the ribbons were peeled off from the substrate. The surface toward the glass substrate side is called "substrate side", and the opposite side "free surface side". The XRD diffraction measurements were mainly performed for the substrate side of the sample by using the diffractometer. Examples of the diffraction patterns of type-L and type-H *n*-Ag are shown in Fig. 3-1-1. Compared with the XRD pattern of *p*-Ag with random orientation (see Fig. 3-1-1(c)) [50], the relative intensity of (111) reflection of both type-L and type-H *n*-Ag was much larger than *p*-Ag. It suggests that most of the crystallites aligned as the (111) planes were parallel to the sample surfaces ((111) preferred orientation). It was reported that for *n*-Au, both type-L and type-H showed the strong (111) preferred orientation [51]. For Ag and Au, the surface energy decreases in the sequence of the (110), (100) to (111) planes [52]. The strong (111) preferred orientation of *n*-Ag and *n*-Au indicates that the nanoparticles deposited align as the (111) plane being parallel to the substrate surface in order to reduce the surface or interface energy.

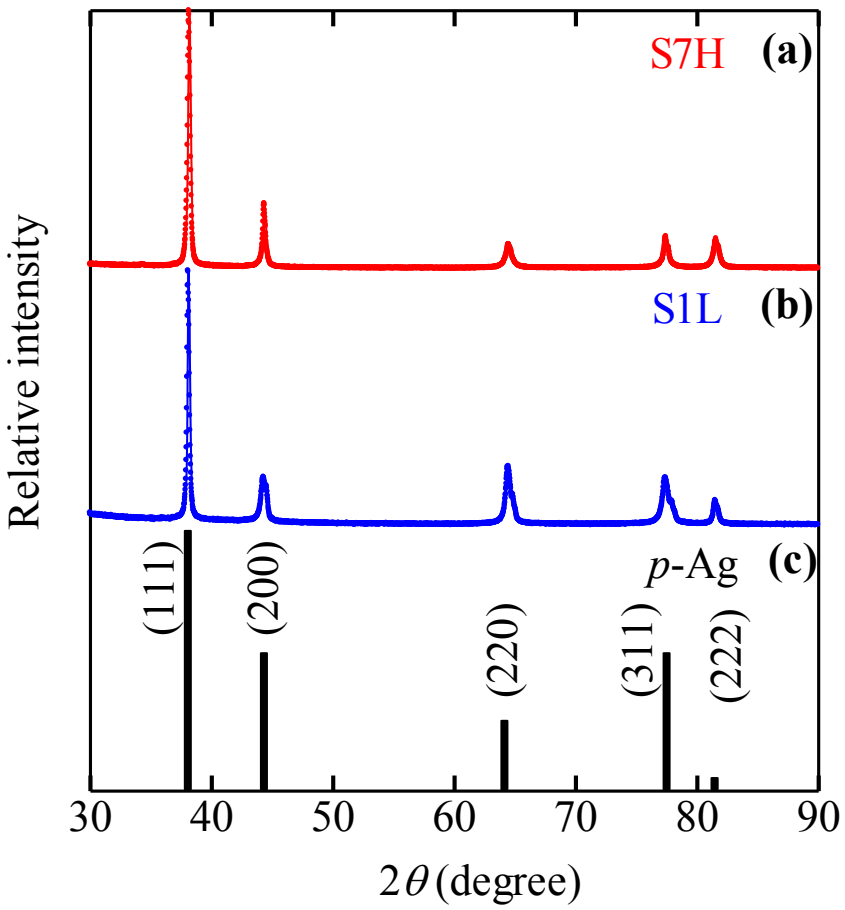

Fig. 3-1-1. XRD spectra of (a) type-H *n*-Ag and (b) type-L *n*-Ag. The positions and the relative intensities for reflections of randomly-oriented *p*-Ag in literature [50] are indicated in (c).

In the XRD pattern of *n*-Au prepared by the gas deposition method, the relative intensity of (200) reflection was lower for type-L than for type-H; almost no (200) reflection was observed for some of type-L *n*-Au [43]. For *n*-Ag, the relative intensity of (200) reflection is higher than that of *n*-Au (see Fig .3-1-1 and Fig .3-1-8). Similar to *n*-Au, intensity of (200) reflection of type-L was slightly lower compared to that of type-H as shown in Fig. 3-1-2.

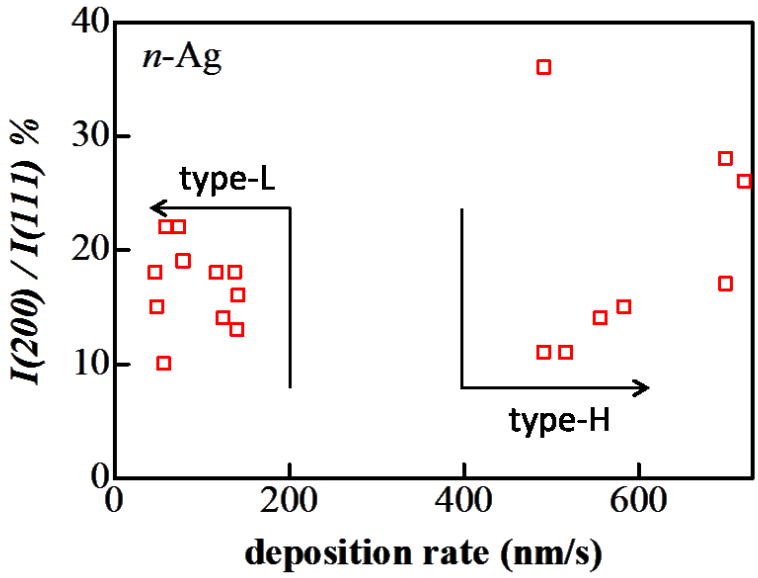

Fig. 3-1-2. Deposition rate dependence in peak intensity ratio between (111) and (200) reflections (I(200)/I(111)) of *n*-Ag.

3.1.2 Density, grain size, lattice parameter and microstrain in the as-prepared state

The relative density (ρ/ρ_0, where ρ_0 is the density of *p*-Ag: 10.5 g/cm^3) as a function of deposition rate is plotted in the Fig. 3-1-3 (a). The relative density of some of type-L *n*-Ag was ρ/ρ_0 = ~96%. The *n*-Ag samples with the lower densities appeared to be too thin and light (~2-8 mg) to measure the density accurately. To improve the accuracy, we prepared type-L samples with enough weight (~10 mg) by increasing the pass number during the deposition. The relative densities of these type-L *n*-Ag samples were above ~ 98% (red symbols in Fig. 3-1-3(a)). It was reported that the relative density of bulk *n*-Ag cold-pressed from milled *n*-Ag powder was about 90 – 95% [53]. Further, the relative density of *n*-Ag prepared by inert gas condensation followed by in situ warm compaction was about 97% [54]. The slightly low relative density comparing with *p*-Ag was attributed to atomic misfit in grain boundaries [55].

The grain size, microstrain and lattice parameter are plotted as a function of deposition rate in Figs. 3-1-3 (b), (c) and (d), respectively. As mentioned in section 2.2.1, the grain size and microstrain were estimated from the Halder-Wanger plots and the results are shown in Fig. 3-1-4. Furthermore, the direct observation of sample surface was conducted by STM (NaioSTM) under the constant current mode (bias voltage: 50 mV, tunnel current: 1 nA) in the atmosphere. As shown in Fig. 3-1-5, the grain size of *n*-Ag estimated from the STM observation was ~30 nm and showed a good agreement with 33 nm from the XRD analysis. The microstrain was estimated from the intercept of Halder-Wanger plots. The microstrain of *n*-Ag was roughly ~0.1% but the microstrain of type-L appeared to be slightly higher than that of type-H (Fig. 3-1-3(c)). From Fig. 3-1-3(d), the lattice parameters of type-L and type-H *n*-Ag were smaller than the value of *p*-Ag. No systematic deposition rate dependence was observed for the lattice parameters of type-L and type-H *n*-Ag.

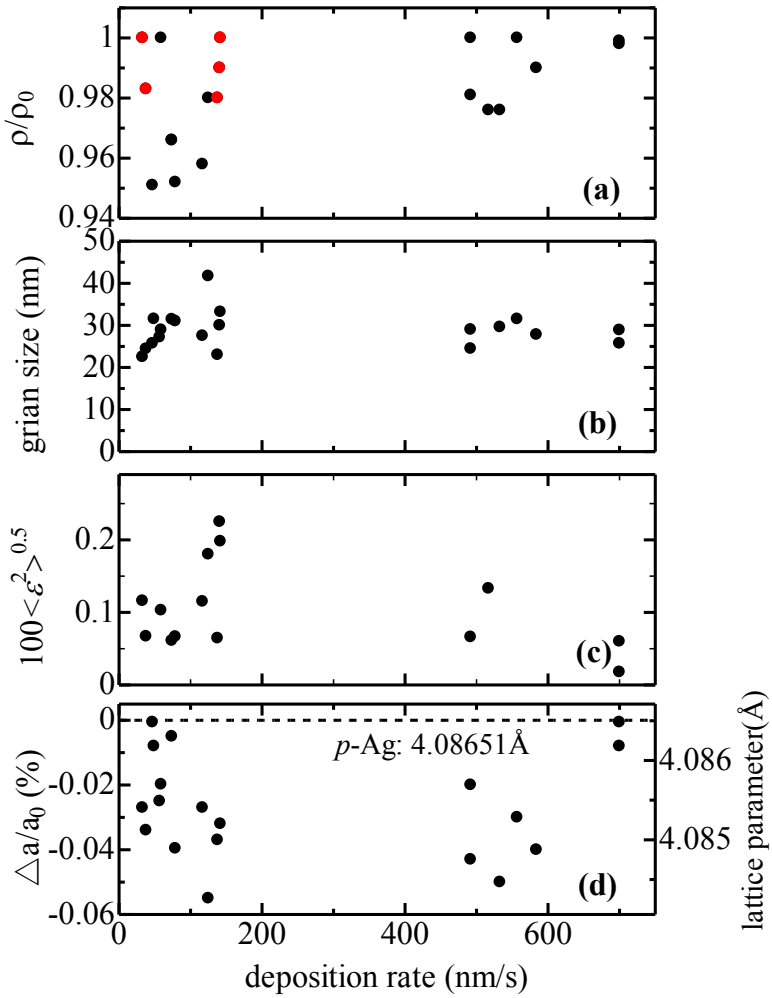

Fig. 3-1-3. (a) Relative density, (b) grain size,(c) microstrain strain as well as (d) lattice contraction as a function of deposition rate. The red dots in (a) are the results that calculated from the sample prepared in specific condition. For details, see text.

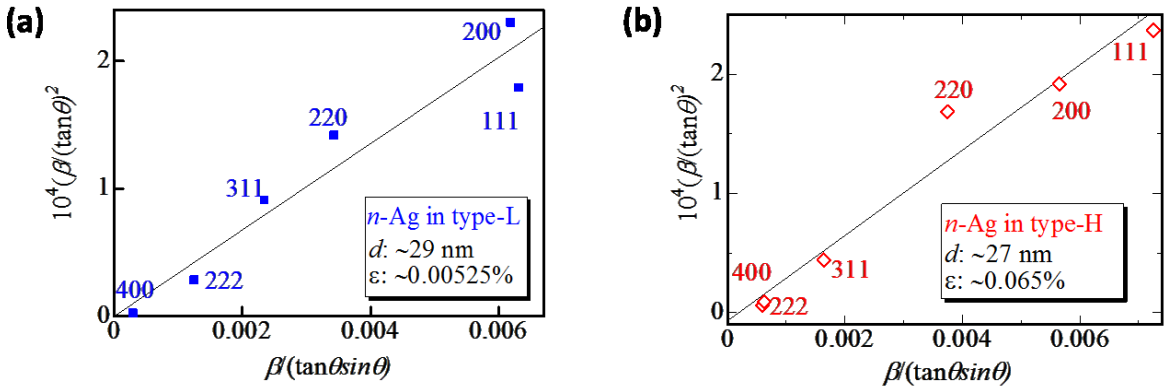

Fig. 3-1-4. Halder-Wanger plots of (a) type-L *n*-Ag (S1L) and (b) type-H *n*-Ag (S7H). The corresponding XRD patterns were shown in Fig. 3-1-1.

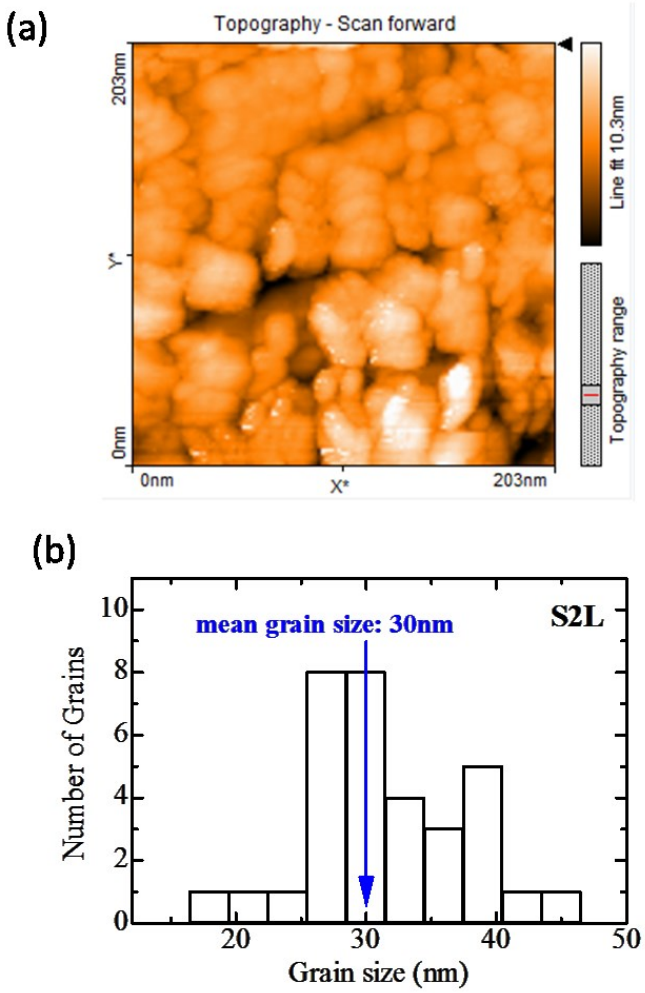

Fig. 3-1-5. (a) STM images (203 ×203 nm^2) of *n*-Ag (S2L, deposition rate: 142 nm/s) surface. (b) The grain size distribution of S2L. The mean grain size estimated from STM is about 30 nm.

3.1.3 Change in texture of *n*-Ag by annealing

In order to study the thermal stability, *n*-Ag was annealed in vacuum at elevated temperatures. Fig. 3-1-6 shows the XRD patterns of *n*-Ag after the annealing. As shown in the Fig. 3-1-6 (a), the (111) preferred orientation of type-L *n*-Ag (S5L) was maintained by annealing at 700 K and relative intensity of (200) reflection increased above half of that of (111) reflection. On the other hand, the (111) preferred orientation of type-H *n*-Ag (S7H) changed to (100) one by annealing at 400 K. The (100) preferred orientation showed a further progress by annealing at 700 K.

The changes of grain size, microstrain and lattice parameter in *n*-Ag by annealing were also investigated. In Fig. 3-1-7 (a), the grain size is plotted as a function of annealing temperature. The grain size of type-L *n*-Ag (S1L) annealed at 400 K was same to that in the as-prepared state. After annealing at 500 K, grain size increased from ~ 29 nm to ~57 nm. The grain size of S5L increased from ~20 nm to ~70 nm after annealing at 700 K. In the case of type-H *n*-Ag (S7H), the grain growth was observed after annealing at 400 K. Furthermore, in some type-H *n*-Ag samples, the grain growth was occurred even at room temperature (see section 3.1.6).It suggests that the thermal stability of type-H *n*-Ag is lower than that of type-L *n*-Ag. The rapid grain growth at room temperature was also reported for *n*-Pd [44]. The lower grain growth temperature of type-H *n*-Ag suggested that the higher grain boundary energy is stored in type-H than type-L. However, as shown in Fig. 3-1-7 (b), the microstrain of both type-H and type-L similarly decreased by annealing. The thermal stability of the nanocrystalline structure is also governed by the geometrical distribution of the various grain boundaries (see section 4.3). Fig. 3-1-7 (c) shows the change in the lattice parameter by annealing. The lattice parameters of both type-H and type-L were recovered to the value of *p*-Ag by annealing.

For type-L *n*-Ag (S1L) with low density, the peak splitting was observed for (111), (200), (220), (311) and (222) reflections. This peak splitting indicated that the crystallites with different lattice parameters were existed; ones with the lattice parameter almost same to that of *p*-Ag and others contracted by about 0.019%. The grain size, microstrain and lattice parameter were estimated from the reflections corresponding to the crystallites with the lattice contraction. The results are shown in Fig. 3-1-7, suggesting that the annealing behavior of S1L was quite similar to other type-L *n*-Au samples. At the present, however, the origin of the peak splitting is not clear.

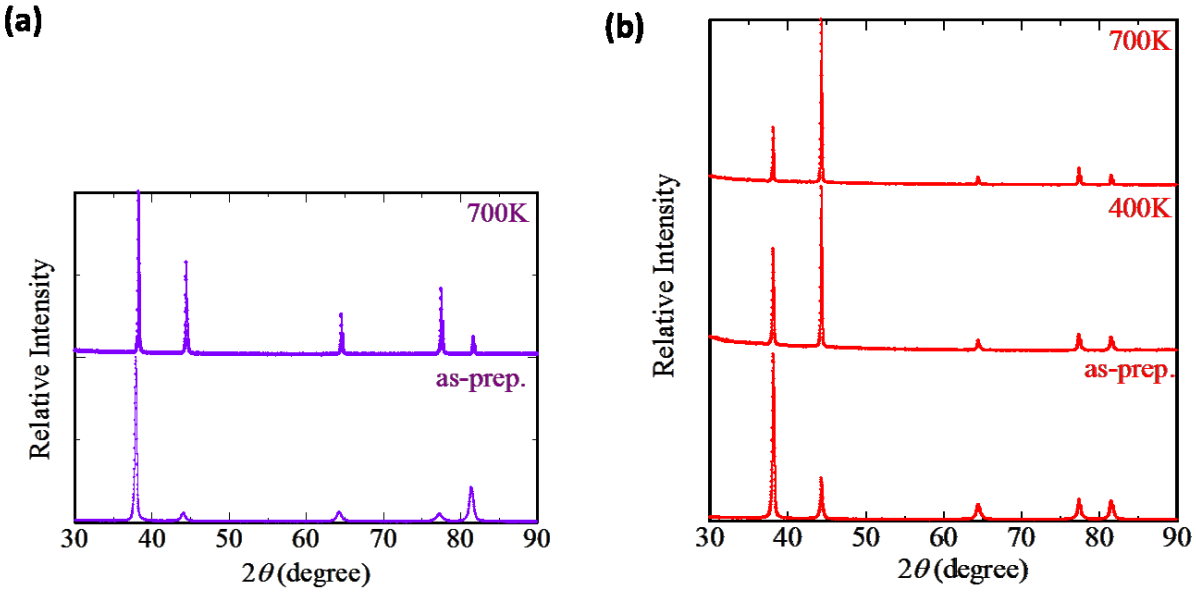

Fig. 3-1-6.(a) XRD pattern of type-L *n*-Ag (S5L, purple) obtained in the as-prepared state and after annealing at 700 K for 3 h. (b) XRD pattern of type-H *n*-Ag (S7H, red) obtained in the as-prepared state and after annealing at 400 K and 700 K for 30 min. The conditions are written on the figure.

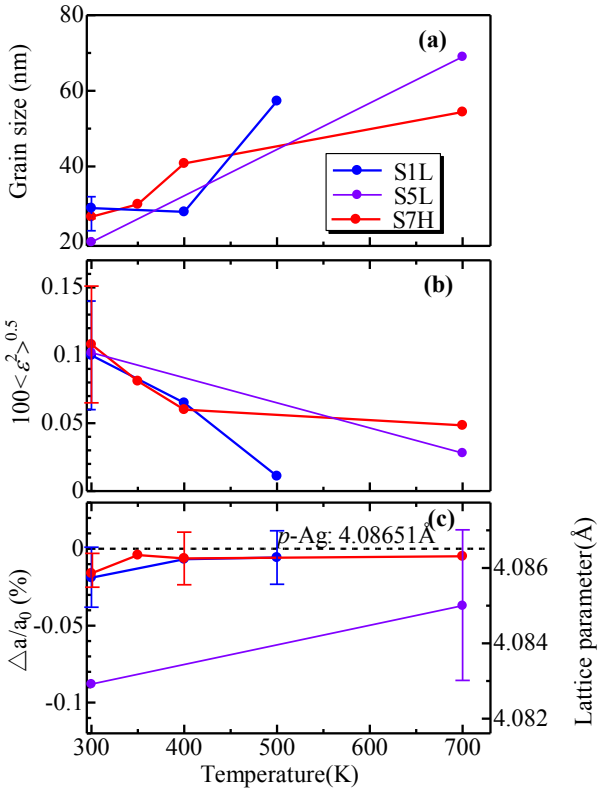

Fig. 3-1-7. Changes in (a) grain size, (b) microstrain and (c) lattice contraction from *p*-Ag (lattice parameter is shown on the right-axis) by annealing at elevated temperatures for 30 m. The data of type-L are plotted by blue (S1L) and purple (S5L) symbols, and type–H *n*-Ag (S7H) red symbols, respectively.

3.1.4 Texture of *n*-Au and change by annealing

For *n*-Au, type-H and type-L were fabricated at the deposition rate above 300 nm/s and below 300 nm/s, respectively. The XRD patterns of type-L and type-H *n*-Au are shown in the Fig. 3-1-8. Both type-L and type-H *n*-Au showed the strong (111) preferred orientation in the as-prepared state. However, the relative intensity of (200) reflection for type-H was higher than that of type-L. The similar (111) preferred orientation and the slight difference in the degree of the (111) preferred orientation between type-L and -H were reported for *n*-Au by Sakai [43, 51, 56].

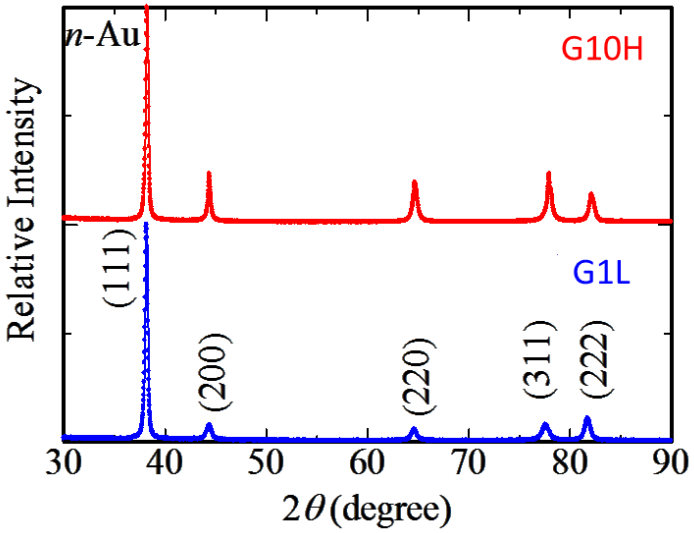

Fig. 3-1-8. XRD spectra of type-H *n*-Au (G10H, red) and type-L *n*-Au (G1L, blue).

The deposition rate dependence in the relative density (ρ/ρ_0, where ρ_0 is density of *p*-Au: 19.4 g/cm^3) of *n*-Au is shown in the Fig. 3-1-9 (a). The relative densities of both type-H *n*-Au and type-L *n*-Au were above 98%. As shown in the Fig. 3-1-9 (b), the grain size of most samples were in the range from ~25 nm to ~35 nm but some of type-L samples were above 40 nm. The microstrain of n-Au was around 0.1% and no obvious deposition rate dependence was observed as shown in Fig. 3-1-9 (c). The deposition rate dependence in the lattice parameter is shown in Fig. 3-1-9 (d), where the lattice parameters of most type-L samples were smaller than *p*-Au. But the lattice parameters of some *n*-Au samples were larger than *p*-Au. These slight larger lattice parameters in *n*-Au may due to the excess free volume in the grain boundaries (see the next section).

Texture changes of type-H and type-L *n*-Au by annealing are shown in Fig. 3-1-10. After annealing at 400 K, the relative intensity of (200) reflection of type-L became stronger than as-prepared state but still maintained the (111) preferred orientation. For type-H, the relative intensity of (200) reflection became much larger and the (111) preferred orientation turned to the (100) one after annealing at 400 K. The changes in the mean grain size of *n*-Au by annealing are shown in Fig. 3-1-11. The apparent grain growth was observed for both type-L and type-H *n*-Au after annealing at

400 K but the type-H *n*-Au appeared to start the grain growth at 350 K. In the previous study [51], it was reported the type-L *n*-Au was thermally more stable than type-H *n*-Au and the type-L *n*-Au maintained (111) preferred orientation by annealing at 700 K. In the present study, type-L *n*-Au samples were prepared near the threshold deposition rate of 300 nm/s. As a consequence, some type-L samples show the characters of type-H *n*-Au in the present study [51].

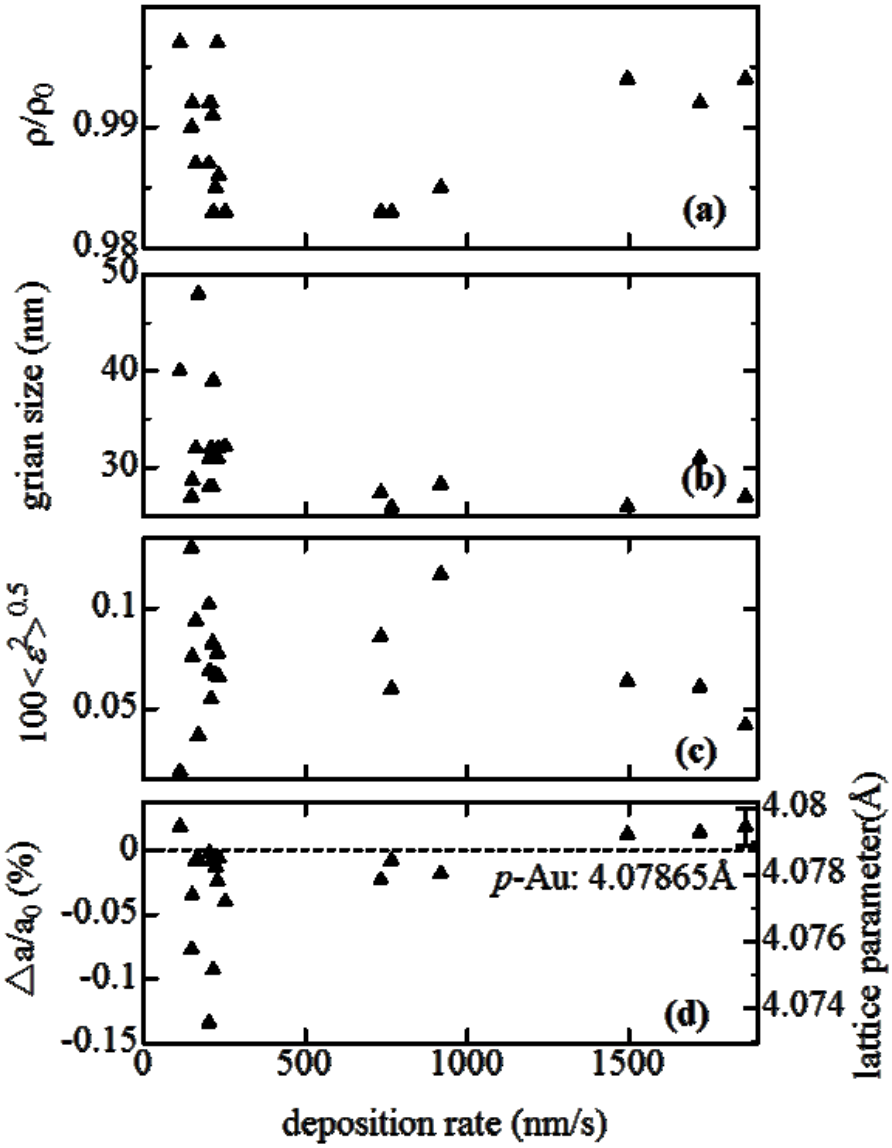

Fig. 3-1-9. (a) Relative density, (b) grain size, (c) microstrain as well as (d) lattice parameter of *n*-Au samples used in present study as a function of deposition rate.

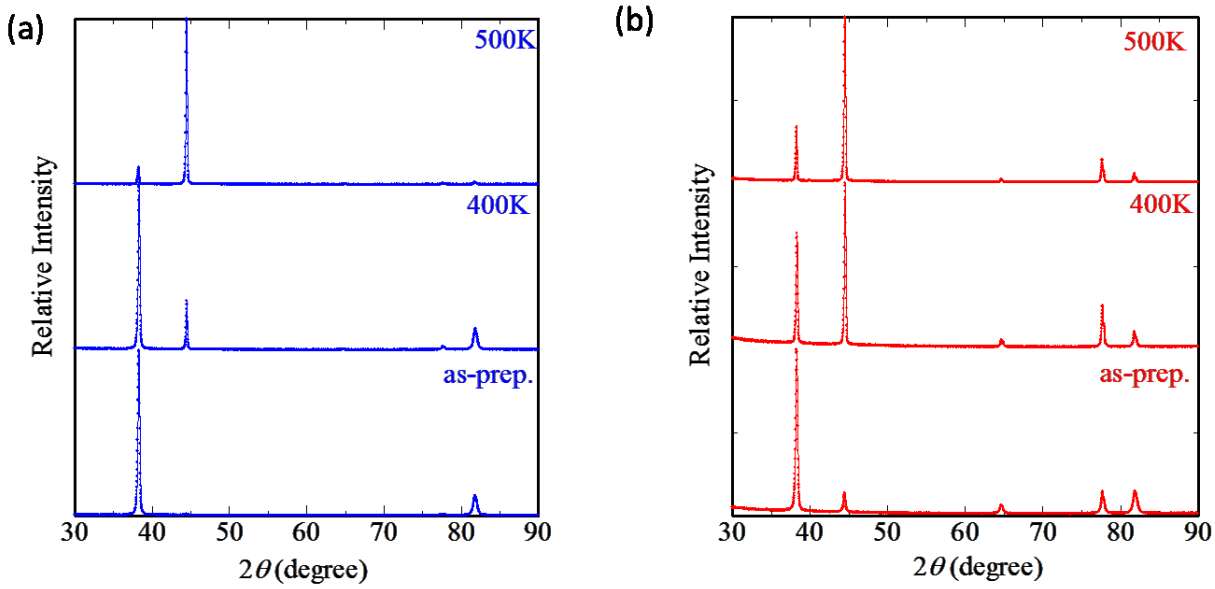

Fig. 3-1-10. (a) XRD pattern of type-L *n*-Au (G2L, blue) obtained in the as-prepared state and after annealing at 400 K and 500 K for 30 min. (b) XRD pattern of type-H *n*-Au (G10H, red) obtained in the as-prepared state and after annealing at 400 K and 500 K for 30 min.

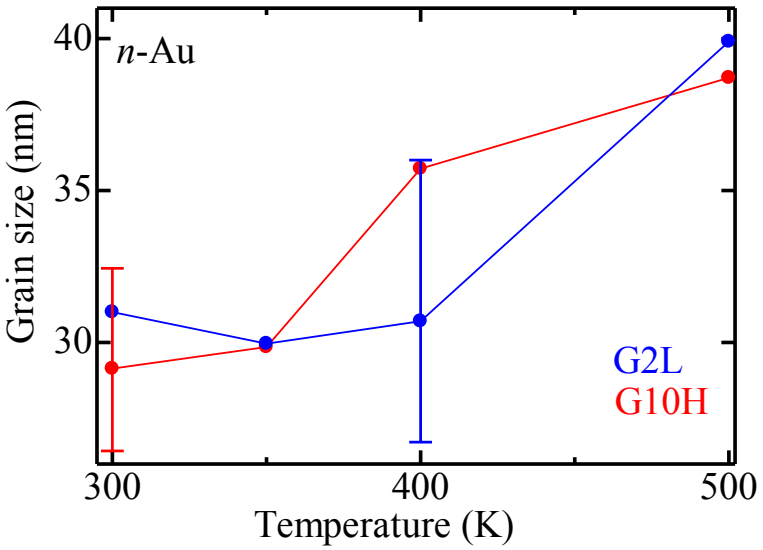

Fig. 3-1-11. The grain size of type-H *n*-Au (G10H, red) and type-L *n*-Au (G2L, blue) obtained after annealing at 350 K, 400 K and 500 K.

The microstructure of substrate-side of G2L was also studied by the electron back scatter diffraction (EBSD) technique. The EBSD measurement was performed by using MI4000L (Hitachi High-Technologies Corporation) at High Voltage Electron Microscope Laboratory, Institute of Materials and Systems for Sustainability, Nagoya University. Fig. 3-1-12 (a) shows the 2 dimensional EBSD map of G2L. The strong (111) preferred orientation was indicated from the EBSD map and it is in good agreement with the XRD analysis. However, some of grains were elongated along the vertical direction in the map and the grain sizes exceeded ~ 200 nm. Since the sample was kept at room temperature for one month before the measurement, the grain growth might be occurred. The pole figure in Fig. 3-1-12 (b) indicates that the orientations of the grains were distributed randomly along the specimen surface. In the distribution of the misorientation angle (Fig. 3-1-12 (c)), high angle grain boundaries with the misorientation angle larger than 15 degrees were dominant. Especially, the grain boundaries with the misorientation angle of 60 and 35 degrees were dominant. It suggests that some kind of ordered structures is existed in the grain boundaries normal to the specimen surface.

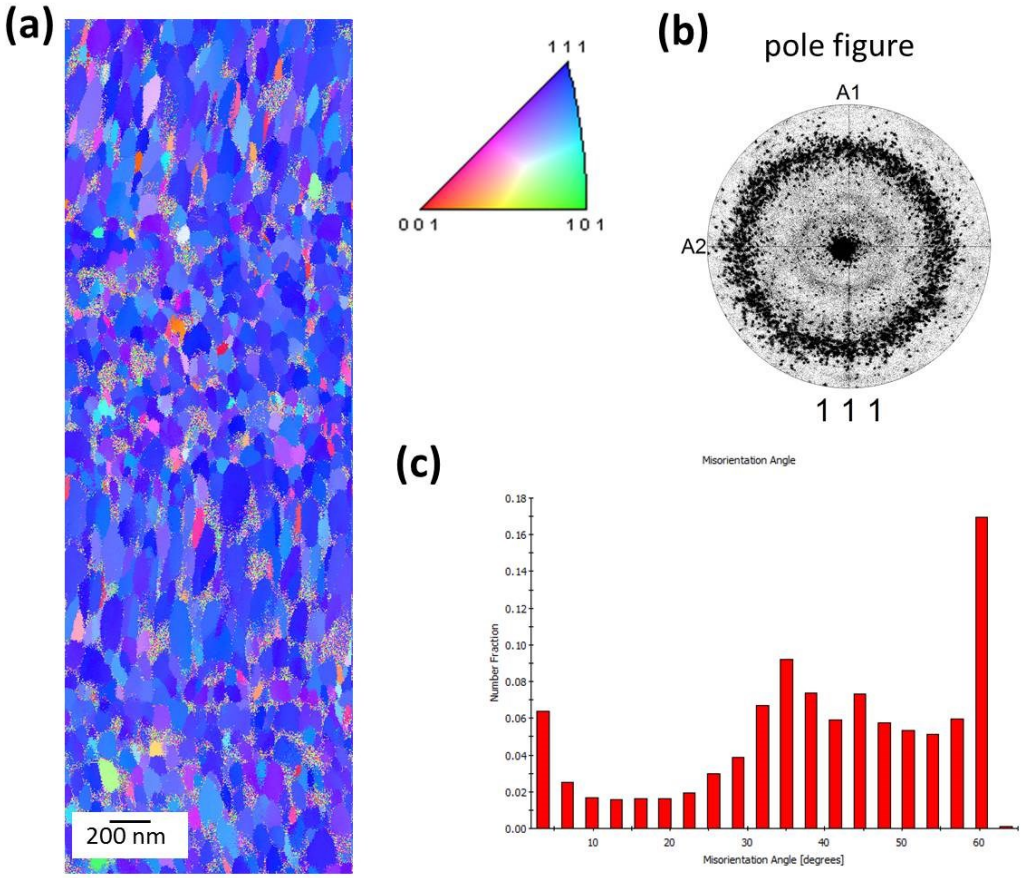

Fig. 3-1-12. (a) EBSD map of type-L *n*-Au (G2L), (b) pole figure and (c) distribution of grain boundaries on misorientation angle.

3.1.5 Lattice parameter as a function of grain size

As mentioned before, a lattice contraction was observed for *n*-Au and *n*-Ag prepared by gas deposition method. The lattice contraction as a function of grain size is displayed in Fig. 3-1-13, where the grain size and lattice parameter were estimated in the as-prepared state at room temperature. Lattice contraction and expansion were often reported for *n*-metals prepared by various methods and summarized in ref [57]. It was reported that at room temperature, the lattice parameter of *n*-Pd fabricated by IGCC method [58] was smaller than that of *p*-Pd and the amount increased with the decrease in the mean grain size (green dash line in Fig. 3-1-13). The lattice contraction of *n*-Pd was attributed to the grain boundary tension[58]. The similar lattice contraction was also reported for other *n*-metals, for example, $\Delta a/a_0 = -0.01\%$ for ball-milled *n*-Ni [9], *n*-Cu, *n*-Fe [57], and *n*-W[59].

As shown in the Fig. 3-1-13, the lattice contraction of *n*-Ag and *n*-Au is more larger than the lattice contraction reported for *n*-Pd and it appears to be difficult to explain by the grain boundary stress. In the case of *p*-metals, the decreases in lattice parameter by vacancies were reported for quenched *p*-Pt and *p*-Au [60]. Further, our previous study suggested that *n*-Au in the as-prepared state contained vacancies of about 0.15% from the recoveries of the lattice parameter and specimen length by annealing above 350 K [61]. It was reported that the lattice parameter of a Pd hydride showed a gradual decrease with time after hydrogenation and the contraction was attributed to the formation of vacancy-hydrogen clusters [62]. These reported results indicate that the large lattice contraction of *n*-metals is induced by the abundant vacancy-type defects in the crystallites. When lattice contraction is induced by the vacancy, the following relationship is expected between the vacancy concentration and the lattice parameter[62].

$$C_v = -(3\Delta a/a_0)/(v_V/\Omega),$$

where C_v is the concentration of vacancy-type defects, a_0 is the lattice parameter without vacancy, v_V is the apparent volume for the vacancy, and Ω is the atomic value. In the present study, v_V/Ω was assumed to be 0.85 and 0.76 according to the values for the vacancy in *p*-Au and *p*-Ag, respectively [63]. By calculation, the right-hand side axis in Fig. 3-1-13 is converted to C_v from the lattice contraction on the left-hand side axis. In the as-prepared state, C_v of *n*-Au was mainly from 0 to ~0.4% and C_v of *n*-Ag was mainly from 0 to ~0.2%. This different vacancy-type defect concentration is maybe due to different vacancy formation energy that 1.24 eV for *p*-Au and 0.82 eV for *p*-Ag [63].

It was reported that lattice parameters of *n*-metals were non-monotonically changed with decreasing the grain size from ~100 nm to ~10 nm [9, 57, 59]: contraction followed by expansion,

where the contraction is attributed to the grain boundary stress and the expansion to the excess free volume in grain boundary (as shown in Fig. 3-1-14) [57]. In Fig. 3-1-14, the contraction and expansion become much larger at the grain size below ~ 30 nm. For understanding the grain size dependence of lattice parameter in detail, the investigations for *n*-Ag or *n*-Au with the grain size of <~20 nm or >~40 nm are necessary.

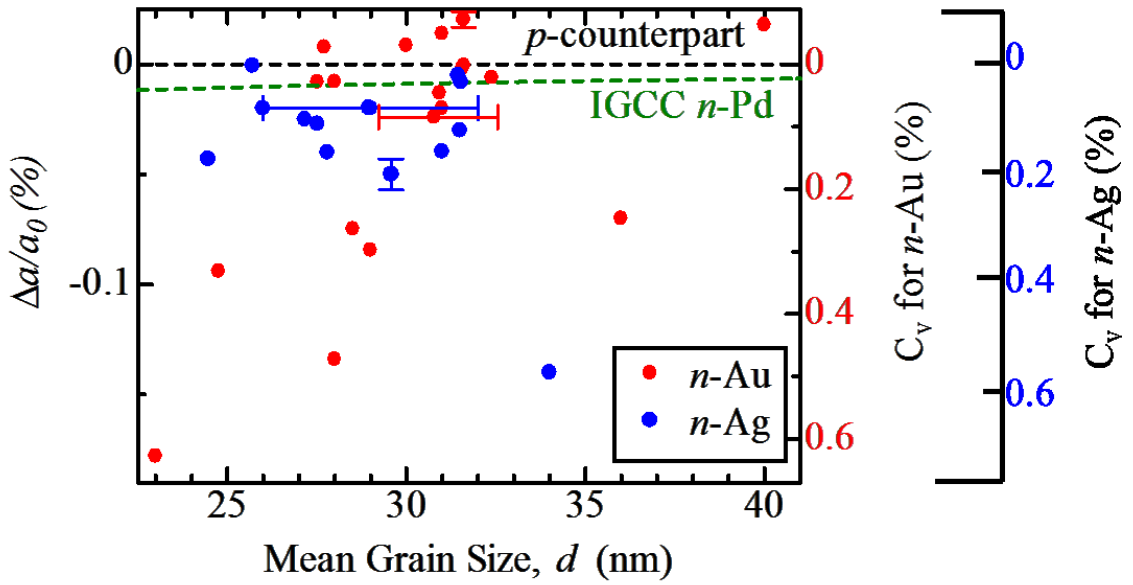

Fig. 3-1-13. Plot of lattice parameter as a function of grain size observed for *n*-Au (red dots) and *n*-Ag (blue dots), where a_0 is the lattice parameter of p-counterpart. The green dash line is the result reported for *n*-Pd [58]. The right-hand side axis indicates the defect concentration calculated from lattice contraction (for details, see text).

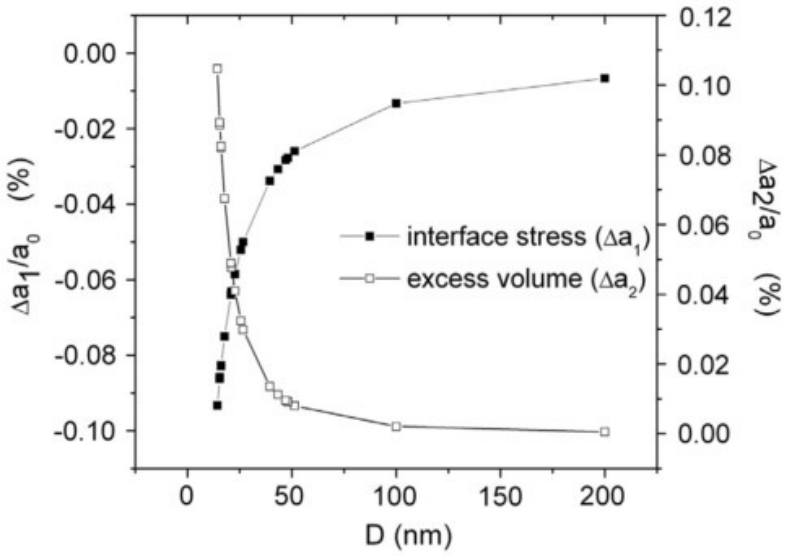

Fig. 3-1-14. Calculated relative changes of lattice parameter induced by interface (grain boundary) stress and excess volume in grain boundary as a function of grain size (details see ref [57]).

3.1.6 Grain growth by aging

As mentioned in experimental, *n*-Au samples were stored in the refrigerator at ~260K. However, the grain growth, texture change and recovery of lattice contraction were observed even at ~260 K for several months. In the case of type-H *n*-Ag, the grain growth and texture change were also observed even at room temperature.

n-Au

The grain growth of type-L *n*-Au was thermally activated above 350 K and the contracted lattice parameter recovered to the *p*-Au value [40]. Although grain growth in a few days like *n*-Ag was not observed for *n*-Au at room temperature, the recovery of the lattice parameter and grain growth were observed by keeping at ~260 K for more than several months. The time changes in lattice parameter, mean grain size, and microstrain induced by aging at 260 K are plotted in the Fig. 3-1-15(a), (b), and (c), respectively. Upon aging at 260 K, the contracted lattice parameter of G1L was relaxed to that of *p*-Au as shown in Fig. 3-1-15(a). Further, the grain growth was occurred simultaneously (Fig. 3-1-15(b)) and the microstrain seemed to be decreased (Fig. 3-1-15(c)). For G3L, due to large initial grain size, it just showed a slight increase of grain size and slight decrease of microstrain. In addition, the texture changed by time shown in Fig. 3-1-15(d), the (111) preferred orientation was maintained by the aging.

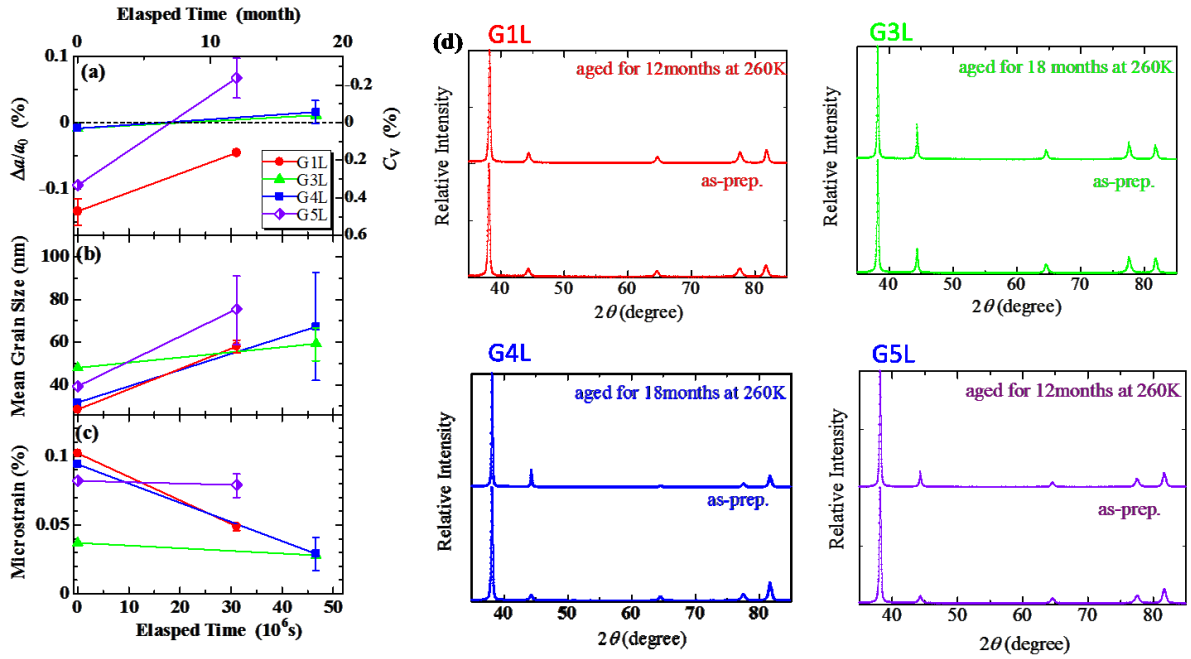

Fig. 3-1-15. Time developments of (a) normalized change in lattice parameter, (b) mean grain size (c) microstrain as well as (d) texture of *n*-Au by aging at 260 K. In Fig. 3-1-15(a), the right-hand-side axis is converted to the vacancy concentration from the lattice contraction.

When the lattice contraction is caused by the vacancies, the recovery of $\Delta a/a_0$ can be explained by the annealing out process of the vacancies. For the simplest model, we assume that the vacancies distributed uniformly in a crystallite diffuse out from the crystallite to the surrounding grain boundaries. Since the grain boundaries act as the sink, the vacancy concentration at the grain boundaries is assumed to be zero. For a spherical shape of the crystallite, the analytical solution for the mean vacancy concentration in the crystallite C_v can be expressed using the following equation [64].

$$C_V/C_{V0} = (6/\pi^2)\sum_{n=1}^{\infty} 1/n^2\, exp(-n^2\pi^2 Dt/R^2)$$

where R is the radius of the spherical crystallite, t is the elapsed time, and C_{V0} the initial C_V at t = 0, respectively. The diffusion constant of a vacancy is given as $D = D_0\exp(-E_m/k_BT)$ where D_0 is the pre-exponential factor, E_m is the activation energy for vacancy migration, and k_B is the Boltzmann's constant. The time development of the mean vacancy concentration was calculated by varying E_m. Then, the time change in C_V/C_{V0} estimated from $\Delta a/a_0$ in Fig. 3-1-15 (a) is compared with the time development of the vacancy concentration. If D_0 = 3×10^{-6} m^2/s reported for *p*-Au [65] and R = 14 nm are further assumed, the model calculation at E_m = 0.89, 0.95, 0.97, and 0.99 eV is performed and the expected time developments are displayed in Fig. 3-1-16. The comparison between the calculated curves and the observed data indicates that E_m = 0. 99 eV is probable (this is the upper bound because of the simultaneous grain growth during aging). This value appears to be similar or slightly larger than the migration energy reported for vacancies in *p*-Au of 0.89 eV [66]. So lattice recovery during aging at 260 K can be explained by the annealing out process of vacancies from the crystallites. It supports that *n*-Au with contracted lattice parameters contains abundant vacancies in the crystallites in the as-prepared state. These vacancies in the nanoparticles may be quenched during the deposition on the cooled substrate.

n-Ag

The grain growth in *n*-metals is mainly driven by excess stored energy in the grain or grain boundary regions[55]. There were several reports that the grain growth of *n*-metals occurred at room temperature. The grain size of *n*-Pd prepared by IGCC method was increased from 10 to 45 nm when it was kept at room temperature for 20 h [44, 67]. Furthermore, a rapid grain growth in ~ 24 h after the deposition was observed in *n*-Cu and *n*-Ag prepared by electrodeposition [68]. For *n*-Ag used in our study, a rapid grain growth at room temperature was observed in some type-H samples as shown in Fig. 3-1-17(a). The decrease in the macrostrain was also observed by the grain growth. At the meantime, the lattice parameter showed a non-monotonic change by time but appeared to increase after passing an enough time (Fig. 3-1-17(b)). The (111) preferred orientation was turned to the (200) preferred orientation by aging at room temperature (Fig. 3-1-17(c)). These texture changes were quite similar to those induced by annealing at elevated temperatures.

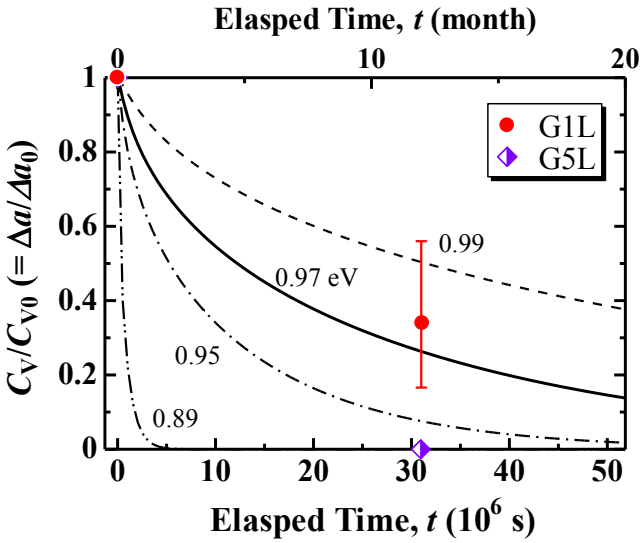

FIG. 3-1-16. Time development of normalized vacancy concentration C_v/C_{v0} during aging at 260 K, where C_{v0} (or Δa_0) denotes C_v (or Δa) at $t = 0$. It is noted that C_v (Δa) of specimen A at $t = 31.1\times10^6$ s is assumed to be zero because the value in Fig. 2(a) is negative (positive). The lines are calculated results with E_m = 0.95, 0.97, and 0.99 eV, respectively, where E_m is the activation energy of vacancy migration and a spherical grain with a diameter R = 14 nm is assumed. The result at E_m = 0.89 eV, the vacancy migration energy reported for *p*-Au, is also shown.

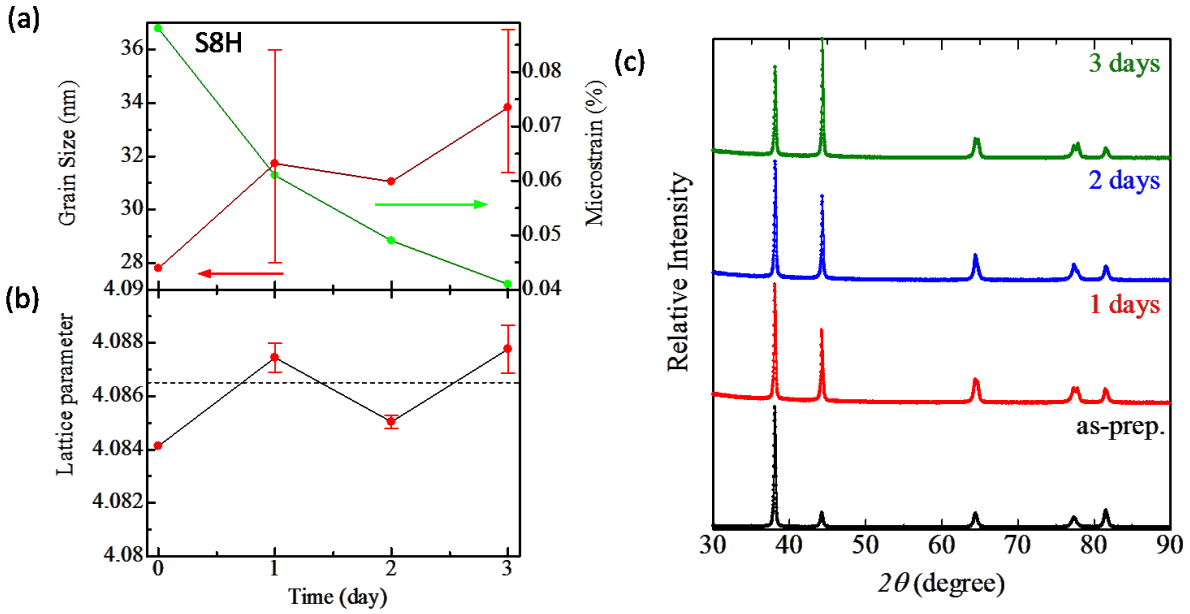

Fig. 3-1-17. (a) Time changes of the grain size and microstrain, (b) lattice parameter and (c) texture observed in type-H *n*-Ag (S8H).

3.1.7 Lattice parameter at low temperature

The characteristic changes in properties observed for *n*-Au and *n*-Ag will be discussed (see section 3.2 to 3.4). In order to study the relationship between the lattice parameter and properties changes from the crystallite state, we conducted low temperature XRD measurements for *n*-Au and *n*-Ag.

Fig. 3-1-18 shows the changes of lattice parameter of (a) *n*-Au and (b) *n*-Ag at low temperatures. The lattice parameters in Fig. 3-1-18 at 300 K were adjusted to the value that estimated from the XRD measurement with Cu-Kα radiation at 300 K. As shown in the Fig. 3-1-18 (a), with decreasing the temperature, the lattice parameters of type-H *n*-Au (deposition rate; G11H: 388 nm/s and G3L: 169 nm/s) at 300 K were slightly smaller than that of *p*-Au and became almost same to *p*-Au because of the smaller temperature coefficient. On the other hand, the lattice parameters of type-L *n*-Au with the deposition rate (G1L: 202 nm/s and G6L: 271 nm/s) were similarly smaller than that of *p*-Au for the temperature range investigated. Although result of G3L has lowest deposition rate, it shown a type-H characteristic. In the Fig. 3-1-18 (b), the similar variations of lattice parameter at low temperatures were observed for *n*-Ag. The lattice parameter of type-L (deposition rate: 80 nm/s) was always smaller than that of *p*-counterpart. The lattice parameter of type-H (deposition rate: 722 nm/s) was smaller than that of *p*-counterpart at around room temperature and became almost same to the value of *p*-Au because of the smaller temperature coefficient.

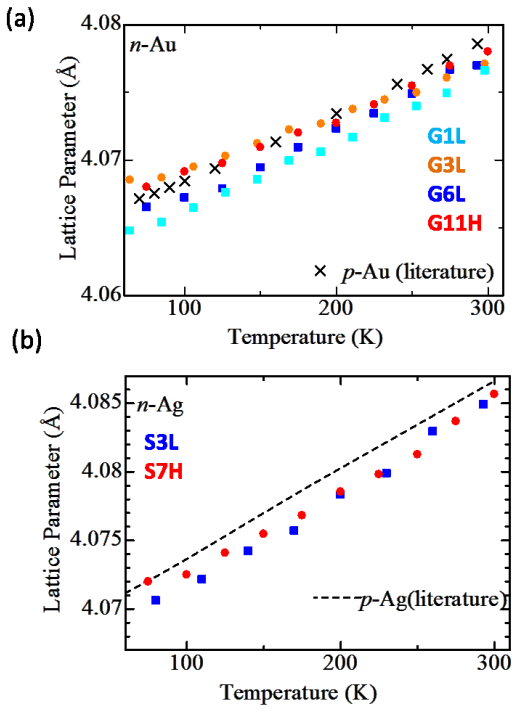

Fig. 3-1-18. (a) Lattice parameters of type-H *n*-Au (red and orange) and type-L *n*-Au (blue and light blue) as a function of temperature. (b) Lattice parameters of type-H *n*-Ag (red) and type-L *n*-Ag (blue) as a function of temperature.

3.2 Internal friction

As mentioned in 3.1, two types of *n*-metal samples were prepared by controlling the deposition rate; one is type-L samples prepared at lower deposition rate and with the better thermal stability and the other is type-H prepared at the higher deposition rate with lesser thermal stability. In the following sections, the results of the internal friction measurement are individually indicated according to the type of the samples.

3.2.1 Internal friction of type-L *n*-Ag

Fig. 3-2-1 demonstrates the temperature dependences of internal friction and resonant frequency for type-L *n*-Ag (S3L). In the figure, the results of *p*-Ag are also depicted. For *p*-Ag, the increase of internal friction started from ~200 K and the internal friction showed a rapid increase linearly with temperature from ~300 to 380 K. It was reported that due to the grain boundary relaxation, the internal friction peak of *p*-Ag was observed at around 430 K with the resonant frequency of about 1 Hz [69]. On the other hand, with increasing temperature, the internal friction of *n*-Ag gradually increased above ~120 K and turned to a rapid increase linearly with temperature above ~200 K.

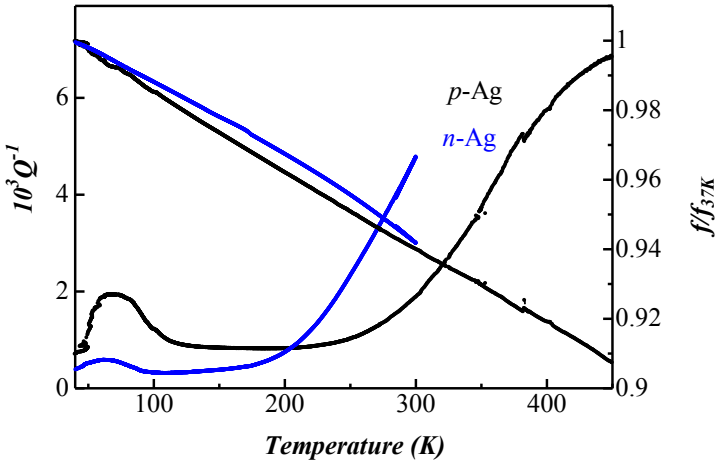

Fig. 3-2-1. Temperature changes in internal friction and resonant frequency of S3L (blue curves). The data of internal friction and resonant frequency (black curves) of *p*-Ag are also depicted. The resonant frequency is normalized by the value at 37 K in the figure (f_{37K} of *n*-Ag is ~300 Hz and that of *p*-Ag is ~1200 Hz).

To investigate the origin of the rapid increase in internal friction observed for *n*-Ag above 200 K, internal friction measurements were conducted above 300 K with increasing the maximum warm-up temperature. As mention in section 3.1.1, the nanostructure of type-L *n*-Ag is thermally stable below ~ 400 K. The changes in grain size and texture of type-L *n*-Ag (S1L) after annealing at elevated temperatures are shown in Fig. 3-2-3. Below 400 K, no obvious grain growth and texture change were observed for type-L *n*-Ag.

The changes in the internal friction spectra of type-L *n*-Ag (S4L) after warm-up to elevated temperatures are displayed in Fig. 3-2-2. The internal friction spectra of as-prepared and warm-up to 350 K are almost similar with each other. When the temperature was increased to 400 K, a slight decrease in internal friction and a slight increase in resonant frequency were observed. When the temperature was further increased to 500 K, the internal friction reached a maximum at around 450 K and then decreased rapidly at around 490 K. Corresponding to the change of internal friction, a sudden rise of resonant frequency at around 490 K was observed (Fig. 3-2-2(b)). The results in Fig. 3-2-3 show the grain growth by annealing above 400 K and the texture change from strong (111) preferred orientation to the random or (100) preferred orientations by annealing above ~450 K. These observations suggest that the rapid increase in internal friction above 200 K is due the grain boundaries in type-L *n*-Ag.

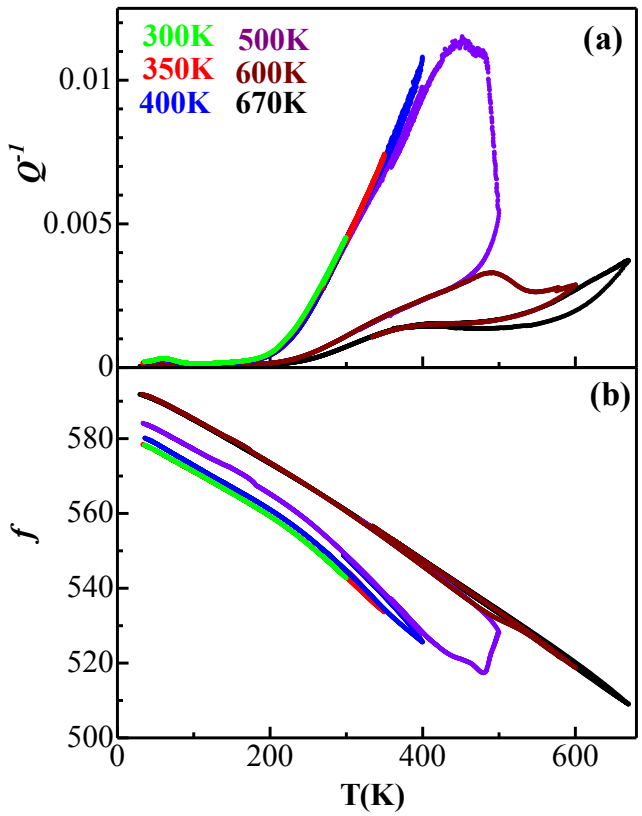

Fig.3-2-2. (a) Changes in internal friction (Q^{-1}) and (b) resonant frequency (f) of type-L *n*-Ag (S4L) observed during the heating up measurements with increasing the maximum heating-up temperature (the values are shown in (a)).

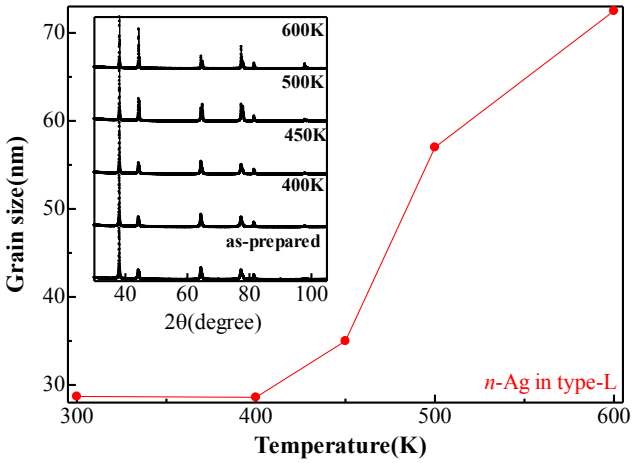

Fig.3-2-3. Change in the grain size of type-L *n*-Ag (S1L) by annealing at elevated temperatures for 30 min. The change in the XRD pattern after annealing is shown in the inset.

3.2.1.1 Activation energy for $Q_{>\sim 200K}^{-1}$ of type-L *n*-Ag

As already mentioned, the rapid increase in internal friction above ~200 K ($Q_{>\sim 200K}^{-1}$) is due to a certain anelastic process in the grain boundaries. The activation energy of $Q_{>\sim 200K}^{-1}$ can be estimated from its onset temperature and the corresponding frequency (see the inset in Fig. 3-2-4) by using the following equation;

$$Q_{GB}^{-1} = \frac{A}{2\pi f_0} \exp\left(-\frac{E_{GB}}{k_B T_0}\right) ,$$

where A is constant, f_0 is corresponding frequency, T_0 is the onset temperature and E is the activation energy. We conducted the internal friction measurement of same sample (S1L) with shortening the length from 8 mm to 6 mm. The results are shown in Fig. 3-2-4. The onset temperature for $Q_{>\sim 200K}^{-1}$ was determined from the intersection between extrapolation from the linearly-increasing part of $Q_{>\sim 200K}^{-1}$ and the background value of Q^{-1} (see the inset in Fig. 3-2-4). The frequency at onset temperature was taken as corresponding frequency. In the analysis, the effect of electrostatic force on frequency was considered from the DC bias voltage dependence in the resonant frequency (see section 2.3.1). Then $\ln(f_0)$ was plotted against the T_0^{-1} and the result is shown in Fig. 3-2-5. The activation energy estimated for $Q_{>\sim 200K}^{-1}$ of type-L n-Ag is about 0.35 eV.

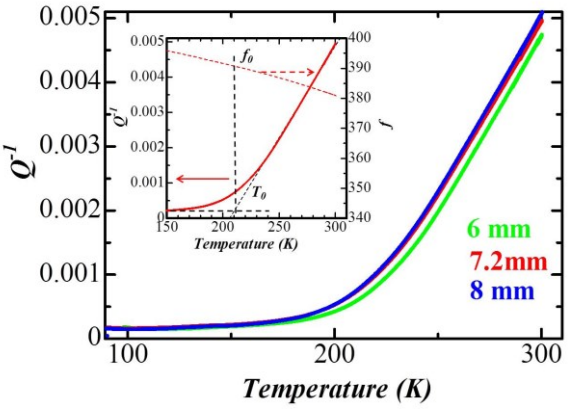

Fig. 3-2-4. Internal friction spectra of type-L n-Ag (S1L) with the different sample length. The value of T_0 was determined by the extrapolation of the linear increased part of $Q_{>\sim 200K}^{-1}$ as shown in the inset (see text for details).

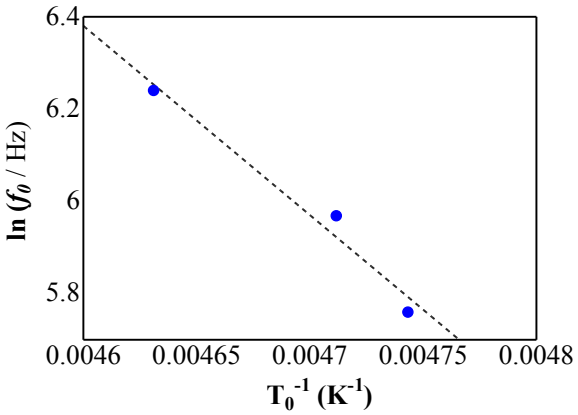

Fig. 3-2-5. Frequency f_0 dependence on T_0 for $Q_{>\sim 200K}^{-1}$ of type-L *n*-Ag (S1L).

3.2.2 Internal friction of type-H *n*-Ag

The internal friction measurement was also conducted for type-H *n*-Ag (S8H). The internal friction spectra are shown in Fig. 3-2-6. Similar to the results of type-L *n*-Ag, a rapid increase in internal friction was observed above ~200 K. However, the amount of $Q^{-1}_{>\sim 200K}$ is slightly smaller than that of type-L *n*-Ag. For example, internal friction of type-H *n*-Ag at 300 K (Fig. 3-2-6) was about 0.0032 in the as-prepared state and that of type-L *n*-Ag (Fig. 3-2-1) was about 0.005. As mentioned in section 3.1.6, the grain growth of type-H *n*-Ag was occurred even at room temperature. In Fig. 3-2-6, the internal friction and resonant frequency spectra observed after keeping for 3 days in room temperature are also shown. It was found that the grain size was increased from ~ 28 nm to ~34 nm accompanied by texture changed (details see Fig. 3-1-17). The decrease in $Q^{-1}_{>\sim 200K}$ by keeping at room temperature, as well as the smaller value of $Q^{-1}_{>\sim 200K}$ of type-H *n*-Ag than type-L *n*-Ag, is responsible to the fact that the grain growth of type-H *n*-Ag could proceed even at room temperature. In Fig. 3-2-6, the resonant frequency, in other words, the dynamic Yong's modulus showed a decrease by about 1.5 % by the grain growth after keeping 3 days at room temperature. The XRD measurement revealed that the (111) preferred orientation of type-H *n*-Ag changed to the (100) one by grain growth. It is noted that dynamic Young's modulus of Ag largely depends on the crystallographic directions; the largest is 118 GPa along the <111> direction and the lowest is 43.7 GPa along the <100> direction [70]. We surmise that the decrease in the resonant frequency by grain growth in Fig. 3-2-6 reflects the change in the preferred orientation along the reed direction.

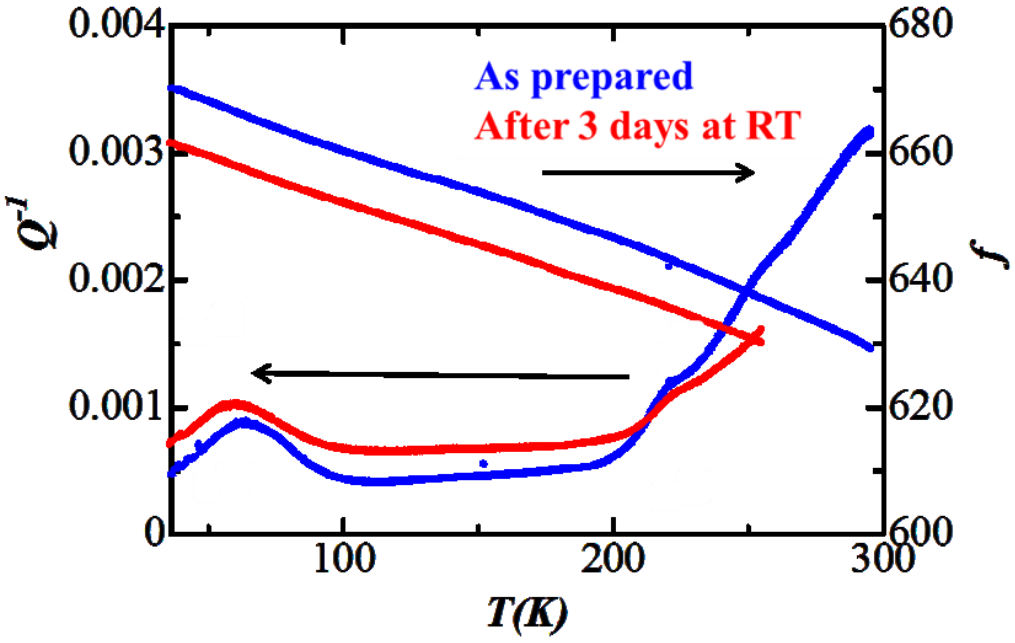

Fig. 3-2-6. Change in internal friction and resonant frequency spectra of type-H *n*-Ag (S8H) by keeping 3 days at room temperature.

3.2.3 Internal friction of type-L *n*-Au

Fig. 3-2-7 shows the resonant frequency (f) and internal friction (Q^{-1}) of type-L *n*-Au (G1L) as a function of temperature. In Fig. 3-2-7(a), $Q^{-1}_{>\sim 200K}$ observed for type-L *n*-Au in the as-prepared state similar to the results in section 3.2.1, 3.2.2 and our previous studies [37, 38, 71]. In Fig. 3-2-7 (a), the resonant frequency showed a rapid decrease corresponding to $Q^{-1}_{>\sim 200K}$ with the temperature increases above ~200 K. The temperature dependences in f and Q^{-1} were similarly observed by repeating the warm-up and cool-down measurements below 300 K. It was reported that the grain growth of *n*-Au started by annealing above 350 K. As mentioned before or from the previous studies [61, 72], $Q^{-1}_{>200K}$ is attributed to the anelastic process thermally activated in the grain boundaries regions above ~200 K. The rapid increase in internal friction, $Q^{-1}_{>\sim 200K}$, was commonly reported in FCC *n*-metals like *n*-Cu[72], *n*-Al[73], and *n*-Ag [74]. For *p*-crystalline, the origin of the grain boundary anelasticity was attributed to grain boundary sliding [75, 76]. Mari group studied the atomicstic process of grain boundary anelasticity by using molecular dynamics simulations and the experiments using bi-crystals. They explained that the origin of anelastic process was the sliding motion along the grain boundary at higher temperatures and migration motion vertical to the boundary plane at lower temperatures [77, 78]. For $Q^{-1}_{>\sim 200K}$ of type-L *n*-Au, the activation energy was reported to be ~0.39eV [79], this is slightly higher than that of type-L *n*-Ag estimated in 3.2.1.1.

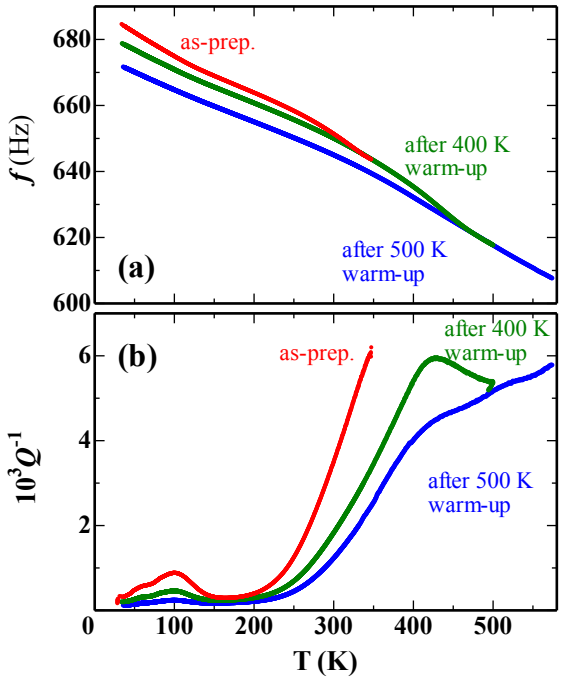

Fig. 3-2-7. Temperature changes in (a) resonant frequency and (b) internal friction observed for type-L *n*-Au (G1L) in the as-prepared state (red), and after heating up to 400 K (green) and 500 K (blue).

In Fig. 3-2-7(a), the resonant frequency of type-L *n*-Au was decreased by annealing. Similar to type-H *n*-Ag (3-2-2), the texture change from (111) preferred orientation to (200) preferred orientation by annealing was observed. The value of dynamic Young's modulus of Au along the <111>, <110> and <100> directions are 116, 81.3 and 41.3 GPa at 300K, respectively [70]. The decrease in f shown in Fig. 3-2-7(a) by heating suggests that the change of the (111) preferred orientation to (200) preferred orientation with the grain growth.

The internal friction of type-L and type-H was investigated in our previous study (see Fig. 1-8.). Result of type-H has a larger internal friction than type-L which is attributed to the higher grain boundary energy [37, 43]. In the present study, we only conducted the internal friction measurement of type-L *n*-Au.

3.2.4 Comparison of internal friction spectrum between type-L *n*-Ag and type-L *n*-Au

The internal friction spectra of type-L *n*-Ag (S4L) and type-L *n*-Au (G6L) are compared in Fig. 3-2-8. In the figure, the increase in internal friction started above ~ 120 K and ~ 180 K for *n*-Ag and *n*-Au, respectively. The fundamental process of the grain boundary anelasticity is governed by reversible local site exchange of atoms in the grain boundaries and the thermal activation data for the grain boundary diffusion may be helpful to discuss the atomistic process of $Q^{-1}_{>\sim 200K}$ [72]. However, the activation energy of grain boundary diffusion is rarely reported for *n*-metals. Here we refer the activation energy of grain boundary diffusion in *p*-metals as the reference. The activation energy of grain boundary diffusion for *p*-Ag (84.43 kJ/mol) was slightly lower than that of *p*-Au (110.6 kJ/mol) [80]. We surmise that the onset temperature of the increase in internal friction in type-L *n*-Ag lower than that of type-L *n*-Au reflects lower activation energy of the atomic motion in the grain boundaries of *n*-Ag.

In Fig. 3-2-8, a small peak was observed at ~80 K and ~105 K for *n*-Ag and *n*-Au, respectively. An internal friction peak was reported for *p*-Au at around 110 K and p-Ag at around 90 K, respectively. These peaks in the *p*-Ag and *p*-Au at low temperature are known as Bordoni peak and they are attributed to the kink-pair formation process of dislocations [81]. However, the existence of dislocations in the grains is still not clear for *n*-metals. For example, dislocations were not detected in *n*-Ag with grain size less than 100 nm prepared by IGCC method [54, 82]. On the other hand, the observation of dislocations was reported for *n*-Ni [83]. The small peaks of *n*-Ag and *n*-Au disappeared by annealing but increased by aging. The mechanism of this peak is still not clear and it is out of focus in present study.

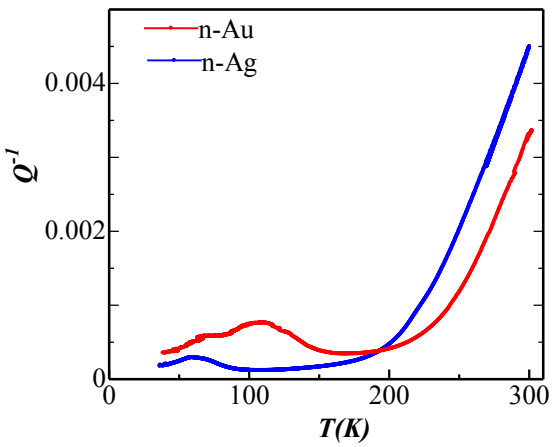

Fig. 3-2-8. Internal friction spectrum of type-L n-Ag (S4L, blue) and type-L n-Au (G6L, red) in the as-prepared state.

3.3 DSC

As mentioned in section 3.2, the internal friction gradually increased at ~ 120 K and ~180 K for *n*-Ag and *n*-Au, respectively, and a rapid increase linearly with temperature above ~200 K ($Q^{-1}_{>\sim 200K}$) was observed in both *n*-Ag and *n*-Au. It was indicated that some atomic motions was thermally activated in the grain boundary region. The thermal activation of the atomic motions may result in the change of the thermal property. Our previous study on the DSC measurement suggested that the heat capacity of *n*-Au slightly increased above ~200 K [40]. In the present study, we conducted more precious DSC measurements of *n*-Au and *n*-Ag to investigate the increase in the anelasticity above ~200 K from the relationship between the heat capacity and the anelastic property.

3.3.1 DSC of *n*-Au

Fig. 3-3-1(a) shows the heat flow curve of type-L *n*-Au (G4L) in as-prepare state, aged state and annealing state. In as-prepare state, the warm-up measurement from 140 to 300 K was repeated for 2 times. These two DSC curves were very similar to each other and showed a good reproducibility within the difference drawn by the small bar in the figure. Then, the sample was annealed at 923 K for 30 min. The grain size after the annealing was larger than 100 nm and the sample after annealing was regarded as *p*-Au in present study. The DSC curve of *n*-Au in the as-prepared state exhibited an endothermic trend above ~170 K as compared with that of *p*-Au. In Fig. 3-3-1(a), the result of sample in the aged state (stored at 260 K for 18 months; d= ~67 nm) is also depicted. The endothermic tendency of the aged sample was similar to that of as-prepared state, however, the endothermic deviation started at slightly higher than ~170 K. The deviations in endothermic heat flow from that of *p*-Au were calculated for *n*-Au in as-prepared state and the aged state and the results are depicted in Fig. 3-3-1(b). The difference in the specific heat from the *p*-Au value was calculated and listed in the left axis of the figure. The results in Fig. 3-3-1(b) clearly indicate that the specific heat of *n*-Au in the as-prepared state becomes larger than that of *p*-Au above ~ 170 K. It was reported that the specific heat of *n*-Cu and *n*-Pd was larger than that of *p*-counterpart from 150 K to 300 K [84]. For the aged *n*-Au sample, the increase in the specific heat was similarly observed but the onset temperature of the deviation appeared to be about 190 K, slightly shifted to higher temperature. The mean grain size of the aged sample was larger than that of as-prepared state but it remained in nano-range. Since the energetically-unstable grain boundaries are easily disappeared by aging, the slightly higher shift of the onset temperature indicates the disappearance of such unstable grain boundaries. If that is the case, the excess specific heat observed above 170 K is responsible for the grain boundaries. It is known that the metallic glass shows a step-like increase in the heat capacity at the glass transition temperature (T_g) during heating [85]. Further, internal friction of the metallic glass also shows a rapid increase above T_g. Therefore, the increased specific heat of *n*-Au from ~170K in our study may indicate that a glass-transition-like behavior was occurred in the grain boundaries.

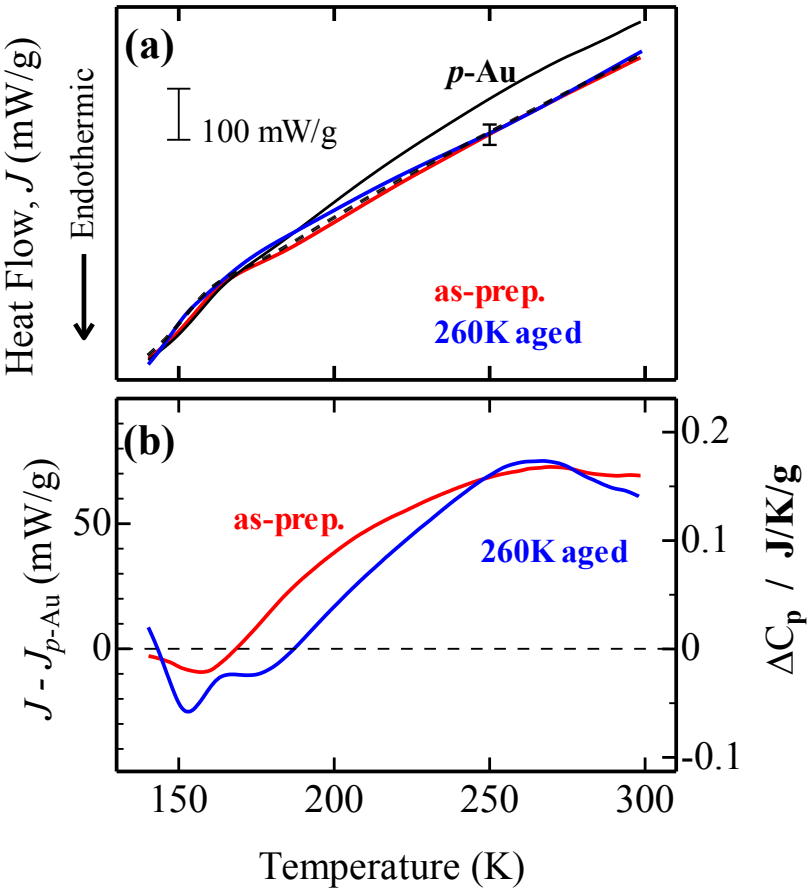

Fig. 3-3-1. (a) Heat flow curves of *n*-Au (G4L) in as-prepared state (red solid line for the first run, dash black line for the second run), aged state (blue solid line) and annealing state (black solid line, regarded as *p*-Au) measured by DSC. (b) Excess endothermic heat flow of *n*-Au compared with that of *p*-Au where the heat flow of *n*-Au in as-prepared state is subtracted by that of *p*-Au. The result of the aged state is also shown.

3.3.2 The DSC of *n*-Ag

In section 3.3.1, the excess endothermic heat flow compared with *p*-Au was observed for *n*-Au. We also conducted DSC measurements of *n*-Ag from ~140 K to 300 K by the repetition of heating and cooling process. The heat flow curves of *n*-Ag in as-prepared state (S5L) and the annealed state are depicted in Fig. 3-3-2 (a). Compared with the heat flow curve of the annealing state, an excess endothermic heat flow was observed in as-prepared state above ~150 K in the heating process. In order to discuss the excess heat flow from annealing state which is close to *p*-Ag, the heat flow of *n*-Ag after annealing was subtracted from that of *n*-Ag in the as-prepared state and the result is depicted in Fig. 3-3-2 (b). The subtracted heat flow curve indicated that the excess heat flow of *n*-Ag showed a maximum at ~240 K and then decreased above ~240 K. The heat flow curves were also measured during cooling from 300 to 140 K. The raw and subtracted curves are also shown in Fig. 3-3-2 (a) and (b), respectively. Similar to the results during heating, the specific heat of *n*-Ag was larger than that of *p*-Ag, however, the maximum in the subtracted curve during cooling is larger than that during heating above ~200 K and the peak temperature is higher.

The DSC measurement is a very powerful method to investigate the phase transition process of materials. But the DSC measurement of *n*-metals is relatively difficult. For *n*-metals with the average grain size of ~ 30 nm, the volume fraction of grain boundaries is about 10% under the assumption that the thickness of the grain boundary is 1 nm. As a consequence, the change in the heat flow due to the transition of the grain boundaries is weakened by the volume effect. In order to study the thermal property of *n*-metals more clearly, the following improvements are highly suggested in the future study; i. increasing the volume fraction of the grain boundary by refining the grain size, ii. increasing the weight of the sample, iii. using power-compensated DSC (more sensitive than heat-flux DSC used in the present study).

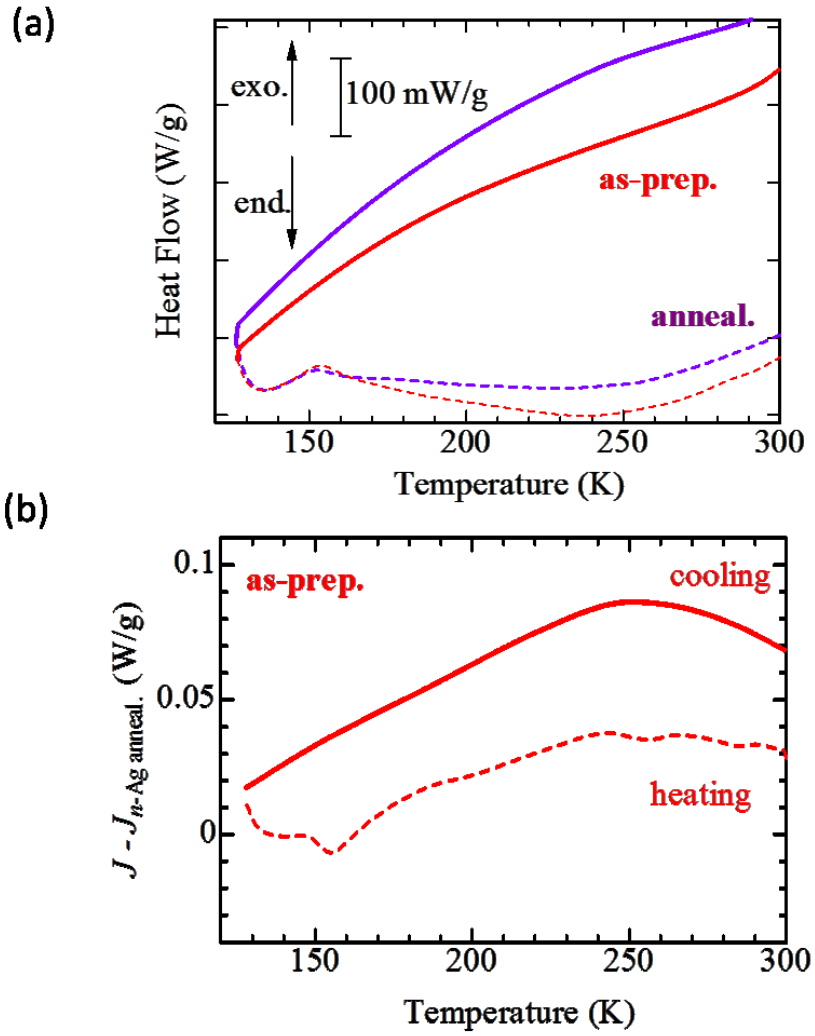

Fig. 3-3-2. (a) Heat flow curves of type-L *n*-Ag (S5L) in the as-prepared state (red) and annealed state (purple) measured by DSC during cooling (solid line) and heating (dash line). (b) The heat flow of *n*-Ag after annealing was subtracted from that of *n*-Ag in the as-prepared state.

3.4 Electrical resistivity measurement

Electrical resistivity is a very sensitive method for detecting the crystalline defects and structural changes in materials, as well as the internal friction and DSC measurements, the state change or phase transformation can be detected from the anomaly in the electrical resistivity.

3.4.1 Temperature change in electrical resistivity of type-L *n*-Au

The temperature change in electrical resistivity of type-L *n*-Au (G7L) in the as-prepared state is shown in Fig. 3-4-1(a). The results after annealing at 923 K for 30 min, aging at 260 K for 18 months and the temperature dependence of *p*-Au in literature [86] are also depicted in the figure for comparison. The mean grain sizes after annealing and aging were ~ 55 and ~74 nm, respectively. It is noted that a good reproducibility in the temperature dependence was achieved for each sample in the as-prepared, annealed and aged states for the repetition of warm-up and cool-down below 300 K. The electrical resistivity of *n*-Au in the as-prepared state was much higher than that of *p*-Au. In general, the electrical resistivity of *n*-metals such as *n*-Pd [4], *n*-Au [87] as well as *n*-Gd [88] was higher than that of *p*-counterpart. It was also reported that the electrical resistivity of the *n*-metals exhibited a grain size dependence. The high electrical resistivity of *n*-metals was attributed to the electron scattering by grain boundaries. Compared with the as-prepared state, the electrical resistivity of the annealed sample became smaller. The electrical resistivity of the aged sample showed the further decrease from that of the annealed sample. The decrease of the resistivity with the increase of mean grain size observed in Fig. 3-4-1(a) supports that the high resistivity of *n*-Au is induced by the electron scattering by the grain boundaries.

In the temperature range shown in Fig. 3-4-1(a), the electrical resistivity of *p*-Au increased linearly with temperature. It is well known that the resistivity of *p*-metals increases linearly with the temperature because of the electron scattering by thermally excited phonons [89]. From the careful observation of the temperature dependence, the electrical resistivity of *n*-Au did not increase linearly with temperature; above ~ 130 K, it showed a slight deviation from the linear increase at low temperatures. The temperature differentiations of the resistivity were calculated to investigate the temperature dependence in detail and the results are shown in Fig. 3-4-1(b). The result of the as-prepared state indicated that the slope below ~110 K was kept constant but slightly decreased with increasing temperature above ~110 K. The resistivity of the as-prepared state between ~ 115 and ~ 130 K in Fig. 3-4-1(a) were fitted by a linear function of temperature. The linear function estimated by fitting is shown by the dashed line in Fig. 3-4-1(a) and the deviation from the linear function is depicted in Fig. 3-4-1(c). The same procedures were also applied to the resistivity of the annealed and aged states. Figs. 3-4-1(a) and (c) indicate that the resistivity of *n*-Au showed a deviatory decrease from the linear function of temperature above ~130 K, the amount of the deviation decreased with the grain growth. The slight deviatory decrease in electrical resistivity

reflects some characteristic change in the grain boundary region.

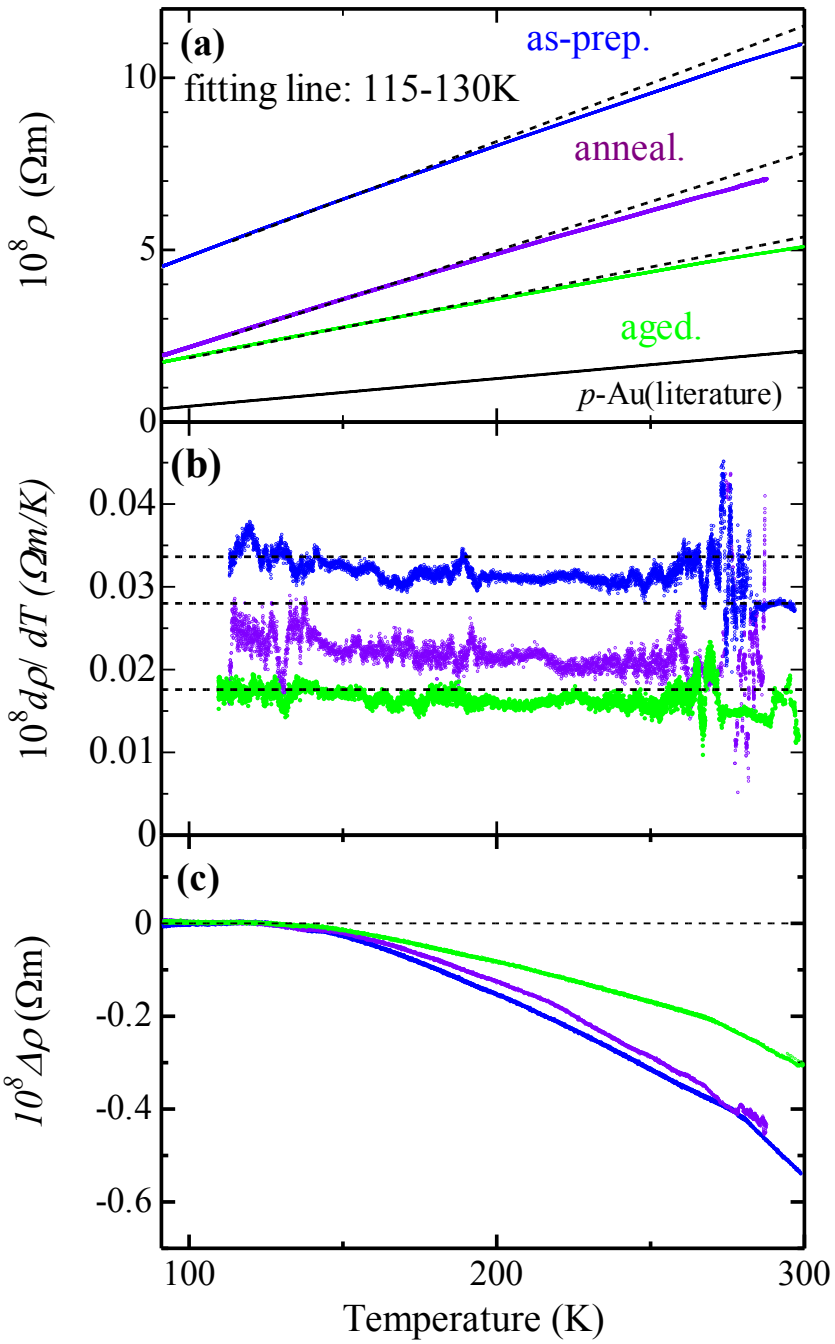

Fig. 3-4-1(a) Temperature change in electrical resistivity of type–L *n*-Au (G7L) in as-prepared state (blue), annealed state (purple) and aged state (green). (b) Temperature differentiation of electrical resistivity in (a). (c) Deviation of electrical resistivity from the linear function depicted by the dashed line in (a). In (a), the dashed lines are determined by linear fitting of the data at low temperatures where the temperature differentiation was constant in (b).

3.4.2 Comparison in resistivity between type-L *n*-Au and type-H *n*-Au

Fig. 3-4-2 (a) shows the temperature changes in electrical resistivity of G6L (blue), G8L (green) and G9H (red). As mentioned in 3.4.1, the electrical resistivity of type-L *n*-Au decreased with the increase of grain size by annealing or aging. In Fig. 3-4-2 (a), the electrical resistivity of G8L with smaller grain size of ~ 32 nm was slightly smaller than that of G6L with larger size of ~ 36 nm. It indicates that the electrical resistivity of *n*-metals is governed by not only the volume fraction but also the characteristics of grain boundaries, such as energy state and the geometrical distribution. It was reported that the electrical resistivity of *n*-Cu decreased by relaxation of the grain boundaries by annealing with keeping the grain size almost same [90]. In Fig. 3-4-2 (b), the temperature differentiations of electrical resistivity decrease from ~110K, although G8L has a large distribution as its low analytical capability.

The electrical resistivity of G9H was higher than that of *p*-Au but smaller than those of type-L *n*-Au in spite of the smallest grain size of ~ 31 nm and the highest deposition rate among the three samples. The results of internal friction indicated that the energy state of the grain boundaries in type-H *n*-Au was higher than that of type-L (See Fig. 1-8). Due to the relatively higher grain boundary energy, the electrical resistivity of type-H *n*-Au was expected to be higher than that of type-L *n*-Au. However, the value of the electrical resistivity of type-H was smaller than type-L. We found that the deviation of electrical resistivity from the linear increase with temperature was similarly observed for type-H *n*-Au as shown in Figs. 3-4-2 (a) and (c).

3.4.3 Electrical resistivity of *n*-Ag

Fig. 3-4-3 (a) exhibits the temperature changes in the electrical resistivity of type-H *n*-Ag (S7H) and type-L *n*-Ag (S6L). Similar to the results of *n*-Au, the electrical resistivity of *n*-Ag was higher than that of *p*-counterpart [86]. Similar to the case of *n*-Au in Fig. 3-4-2(a), the resistivity of type-H *n*-Ag was smaller than that of type-L *n*-Ag in spite of the relatively smaller grain size of type-H. Further, similar to the case of *n*-Au, the electrical resistivity of both type-L *n*-Ag and type-H *n*-Ag showed the deviatory decrease from the linearly increase with increase of temperature (Fig. 3-4-3 (a)). However, the detailed analysis shown in Fig. 3-4-3(c) indicated that the deviation appeared to start at ~100 K, which is lower than that of *n*-Au.

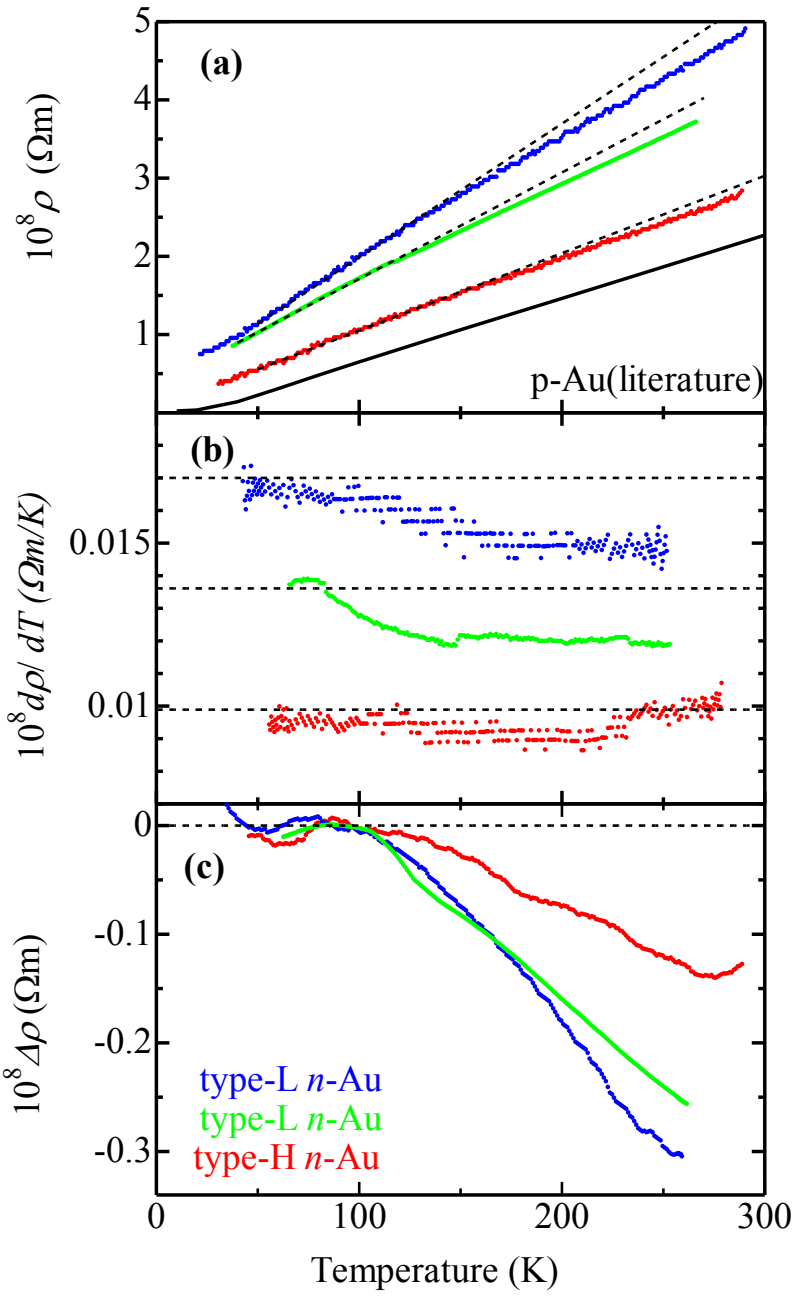

Fig. 3-4-2. (a) Temperature change in electrical resistivity of type–L *n*-Au (G6L, blue; G8L, green) and type-H *n*-Au (G9H, red). (b) Temperature differentiation of electrical resistivity in (a). (c) Deviation of electrical resistivity from the linear function depicted by dash line in (a). In (a), the dashed lines are determined by linear fitting of the data at low temperatures where the temperature differentiation was constant in (b).

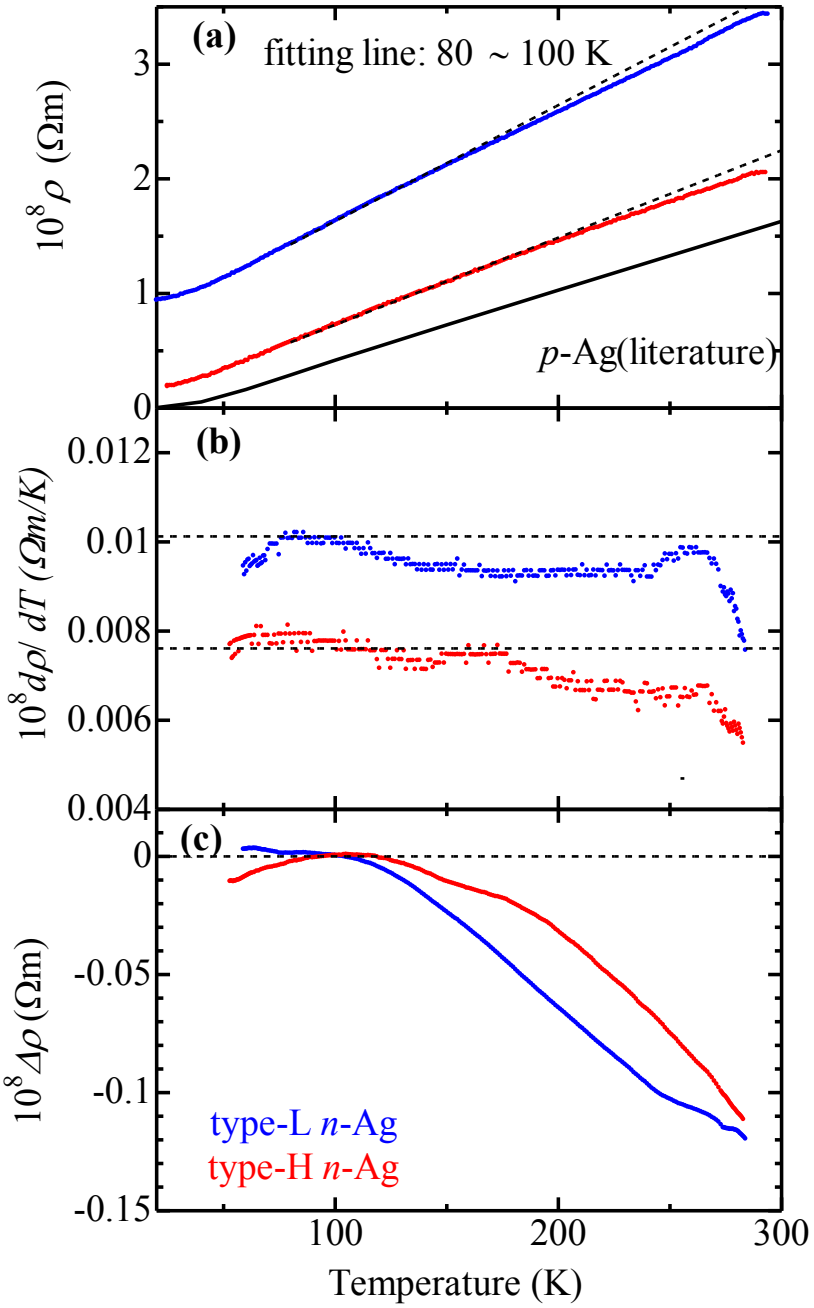

Fig. 3-4-3. (a) Temperature change in electrical resistivity of type–L *n*-Ag (S6L, blue) and type-H *n*-Ag (S7H, red). (b) Temperature differentiation of electrical resistivity in (a). (c) Deviation of electrical resistivity from the linear function depicted by dash line in (a). In (a), the dashed lines are determined by linear fitting of the data at low temperatures where the temperature differentiation was constant in (b).

Chapter 4 Discussion

4.1 Glass-transition like behavior of grain boundaries in FCC *n*-metal

As mentioned in sections 3.2, 3.3 and 3.4, characteristic changes in anelastic, thermal as well as electrical properties were observed for *n*-Au and *n*-Ag at low temperatures. These characteristic changes of *n*-Au and *n*-Ag were summarized in Fig. 4-1-1 and Fig. 4-1-2, respectively. The internal friction of *n*-Au and *n*-Ag started to increase at around 180 K and 120 K, respectively, and both *n*-Au and *n*-Ag showed a rapid increase linearly with temperature above ~200 K (Figs. 4-1-1(a) and 4-1-2(a), see 3.2 for details). The excess endothermic heat flow compared with the *p*-counterpart was found for *n*-Au above ~170 K and above ~150 K for *n*-Ag, respectively (Figs. 4-1-1(b) and 4-1-2(b), see 3.3 for details). The electrical resistivities of *n*-Au and *n*-Ag below room temperature were larger than those of *p*-counterpart, on the other hand, the slight deviatory decrease from the linear increase with temperature started above ~130 K for *n*-Au and above ~100 K for *n*-Ag, respectively (Figs. 4-1-1(c) and 4-1-2(c), see 3.4 for details). These characteristic changes were repetitively observed by cool-down or warm-up below room temperature. Furthermore, the quantities of these characteristic changes decreased with the progress of grain growth. It suggests that the grain boundary regions are responsible for these characteristic changes.

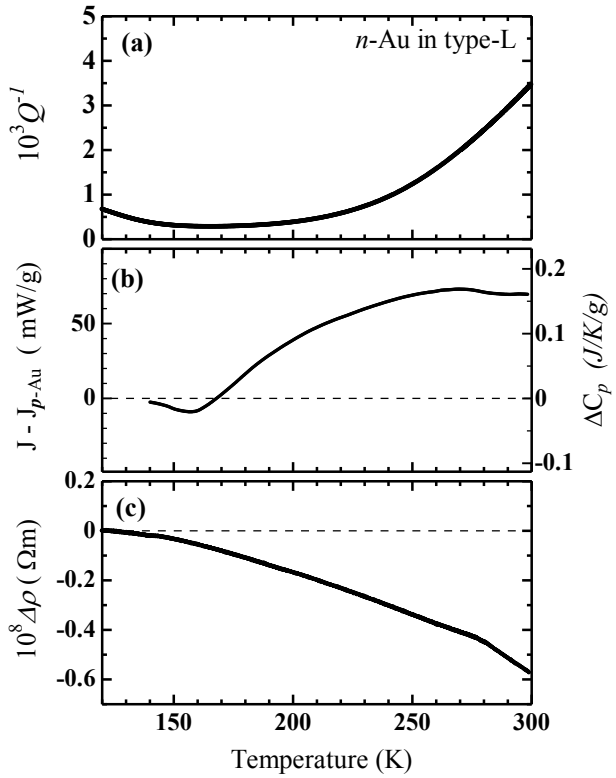

Fig. 4-1-1. (a) Internal friction (same to Fig. 3-2-7), (b) heat flow curve (same to Fig. 3-3-1) and (c) deviation of electrical resistivity from the linear increase with temperature (same to Fig. 3-4-1) observed for *n*-Au below room temperature.

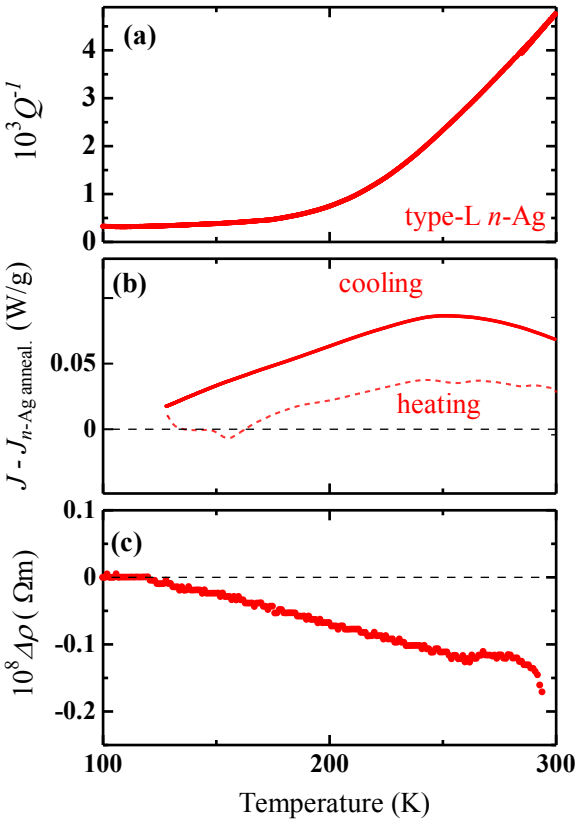

Fig. 4-1-2. Internal friction (same to Fig. 3-2-2), (b) heat flow curve (same to Fig. 3-3-2) and (c) deviation of electrical resistivity from the linear increase with temperature (same to Fig. 3-4-3) observed for *n*-Ag below room temperature.

As already mentioned in 3.3.1 or as shown in Fig. 4-1-3(a), the step-like increase in specific heat was reported for the metallic glasses at glass transition temperature (T_g). The increase in the specific heat indicates the state change from the glass solid to the supercooled liquid state. Further, the increase in the internal friction and the decrease in the electrical resistivity were also reported for metallic glass at around the T_g. Fig. 4-1-3 (a) shows the electrical resistivity and heat flow curve reported for $Pd_{40}Cu_{30}Ni_{10}P_{20}$ bulk metallic glass [85]. The electrical resistivity gradually decreased with the increase of temperature and the negative slope became steeper at T_g. This relatively negative temperature coefficient of resistivity below T_g is regard as an inherent variation of the electron transport at the glass transition in metallic glass [85, 91]. Such a decrease in the electrical resistivity of metallic glasses was attributed to changes in the structure factor by applying Ziman's model for pure liquid metals, and the phonon properties as well as configurational change at T_g [92]. The temperature change in internal friction reported for $Cu_{36}Zr_{48}Al_8Ag_8$ bulk metallic glass [93] is shown in Fig. 4-1-3 (b). For internal friction measurement of the metallic glass, the internal friction started the increase at T_g and reached the maximum value slightly above the crystallization temperature (this irreversible peak is known as the crystallization peak) [94]. The increase in internal friction and the decrease in dynamic modulus above T_g in Fig. 4-1-3 (b) reflect the phase

transition of the metallic glass from the solid state to the viscoelastic supercooled liquid state at T_g [93].

The characteristic changes in various properties observed for *n*-Au (Fig. 4-1-1) and *n*-Ag (Fig. 4-1-2) below room temperature are qualitatively similar to those of the above mentioned metallic glasses at around T_g. Since no long-range periodic arrangement of atoms is existed in the grain boundaries, one can expect that the grain boundaries of *n*-Au and *n*-Ag behave like the amorphous alloys. In the early studies, the "amorphous-cement-like" structure was reported for high angle grain boundaries of *n*-metal and *n*-Si [17, 29] from the computer simulations. Recently, a string-like collective atomic motion reported was for the grain boundary of *p*-materials at 900 K from MD simulation [24]. Since the string-like collective atomic motion is typical for glass forming liquid, the glass transition of the grain boundaries is pointed out. Similar string-like atomic motions were also reported for the grain boundaries of colloidal crystals with grain size of 600 nm by using a confocal microscopy and MD simulation [31]. Furthermore, shear softening of the grain boundary was reported for *n*-Pd during the deformation and a similarity to shear softening of shear transformation zones (SZT) in metallic glasses was pointed out [44]. From these reports and the present results, it is surmised that the grain boundaries in *p*- and *n*-materials possess glassy behaviors and show the glass-transition like change by temperature.

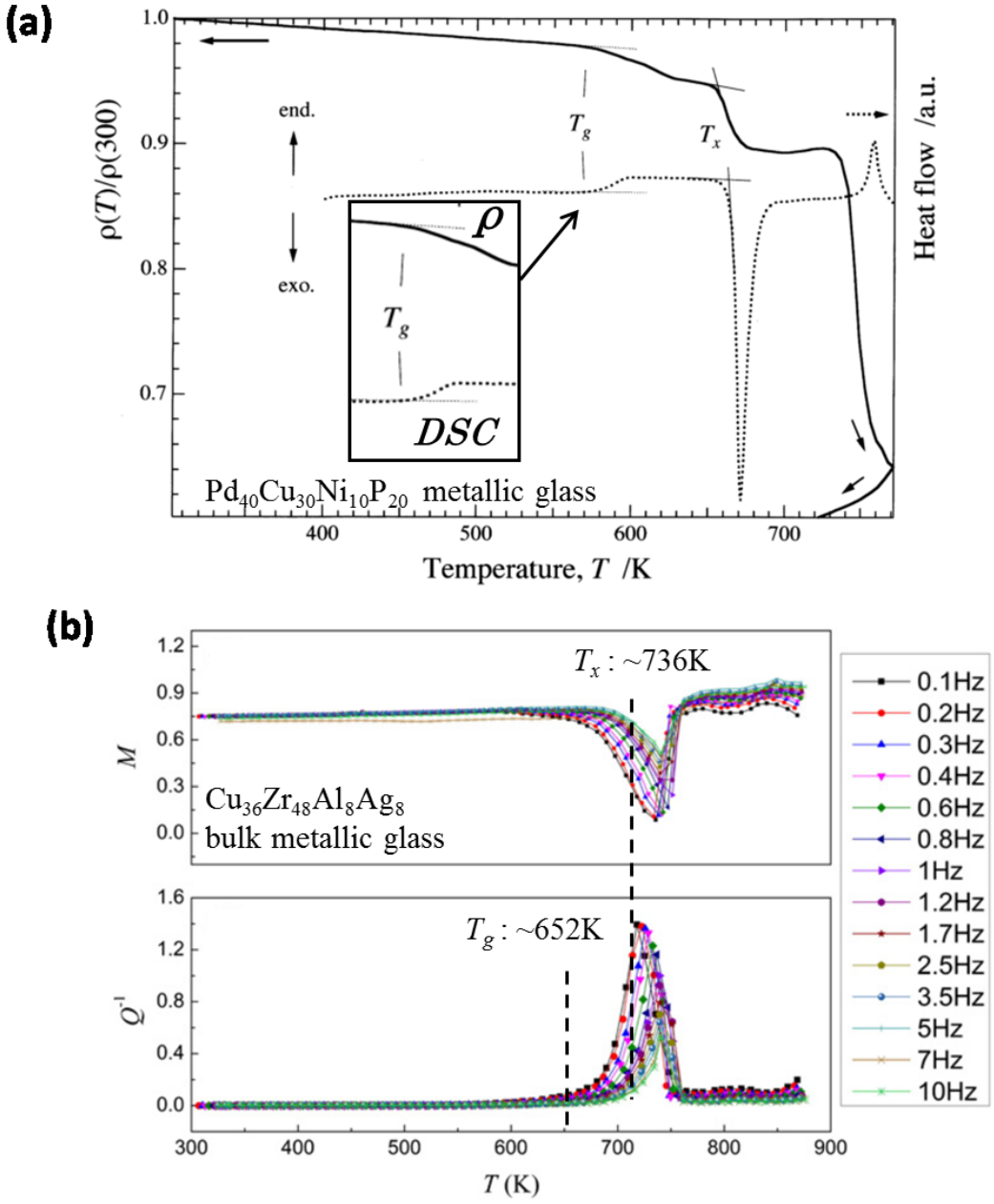

Fig.4-1-3 (a). Temperature dependence of electrical resistivity (solid line) and heat flow curve (dash line) reported for $Pd_{40}Cu_{30}Ni_{10}P_{20}$ metallic glass. The inset magnifies the changes of electrical resistivity and heat flow curve at around the glass transition temperature [85]. (b) Temperature dependences of relative modulus (M, upper panel) and (b) internal friction (Q^{-1}, lower panel) reported for $Cu_{36}Zr_{48}Al_8Ag_8$ bulk metallic glass. The measurements frequency was changed from 0.1 to 10 Hz and the measurements were performed at a heating rate of 0.0167 K/s [93]. The dashed lines indicate the glass transition temperature (T_g) and crystallization temperature (T_x).

The structural transitions of grain boundary by temperature were reported. Tang showed that an order-disorder transition in the first-order was induced in grain boundaries below the melting temperature [26]. A reversible first-order structural transformation at 1000K was reported for Σ 5(310) grain boundary of *p*-Cu from MD simulation [27]. These results suggest the possibility of the first-order structural transition in the grain boundaries. On the other hand, the gradual endothermic feature was observed in our DSC measurements (Fig. 4-1-1(b) and 4-1-2(b)) but no heat flow peaks of the first-order transition. It indicates that the second-order like transition is occurred in the grain boundaries of *n*-Au and *n*-Ag which is analogous to the glass transition of the metallic glasses. We surmise that the grain boundaries in n-metals turn from a "glassy" state to a "supercooled-liquid" state at a certain temperature, $T_{c\text{-}GB}$, as shown in Fig. 4-1-4. In the supercooled-liquid state above $T_{c\text{-}GB}$, the mobility of atoms in the grain boundaries become active and the *n*-metals show large anelasticity. On the other hand, in the glassy state below $T_{c\text{-}GB}$, the atomic motions in the grain boundaries are frozen like in glass solids and the *n*-metals become ideal elastic.

The onset temperatures of the characteristic temperature changes of the grain boundaries in *n*-Au and *n*-Ag were lower than ~200 K. For *n*-Au, the increase of internal friction started from ~180 K, the endothermic tendency started above ~170 K and the electrical resistivity slightly deviated from the linear temperature increased above ~150 K. For *n*-Ag, the increase of internal friction started above ~120 K, the endothermic tendency started above ~150 K and the electrical resistivity slightly decreased from ~100 K. On the other hand, the glass transition of metallic glasses usually occurs at high temperatures above room temperature. For example, T_g = ~ 670 K was reported for $Pd_{40}Cu_{30}Ni_{10}P_{20}$ metallic glass [85] and ~ 652 K for $Cu_{36}Zr_{48}Al_8Ag_8$ bulk metallic glass [93] as shown in Fig. 4-1-3. Also from the computer simulation results, the structural transitions of grain boundary above 1000K or near melting temperature were reported. It is known that the grain boundaries of *n*-metals are mechanically much strained. High strain energies are stored from the large atomic mismatch between the adjacent grains or from the large deformation induced during the fabrication [11]. As a consequent, the grain boundaries of *n*-metals are in energetically metastable state and the grain growth is induced at lower temperature; in some cases, the *n*-metals show the grain growth even at room temperature. It was reported that the activation energy for the atomic movement in the grain boundaries of Pd was decreased with the increase in the grain boundary energy [95]. In contrast, *n*-Au and type-L *n*-Ag in the present study were thermally stable and the rapid grain growth was observed by warm-up above 350 K. As mentioned in section 3.1, *n*-Au and *n*-Ag in the present study showed the strong (111) preferred orientation in the as-prepared state. It was suggested that the structural relaxation was induced at the interfaces during the deposition of the nanoparticles. The high energy state of the grain boundaries in *n*-metals might lead to the much lower onset temperatures of the characteristic changes in *n*-Au and *n*-Ag compared with T_g of the metallic glasses. The strong (111) preferred orientation seems to stabilize the nanocrystalline structure with such a high energy state of the grain boundaries. The

characteristic low temperature changes in *n*-Ag were quantitatively similar to those of *n*-Au. However, the temperature range for *n*-Ag was lower than that of *n*-Au. It reflects the smaller grain boundary diffusion energy of *p*-Ag (84.43 kJ/mol) than the value for *p*-Au (110.6 kJ/mol) [80].

In addition to *n*-Au and *n*-Ag, $Q^{-1}_{\sim 200K}$ was also reported for other FCC *n*-metals, such as *n*-Cu [72] and *n*-Al [73]. The investigations of electrical and thermal properties of these FCC *n*-metals gain further insights on the characteristic temperature changes of the grain boundaries in *n*-metals.

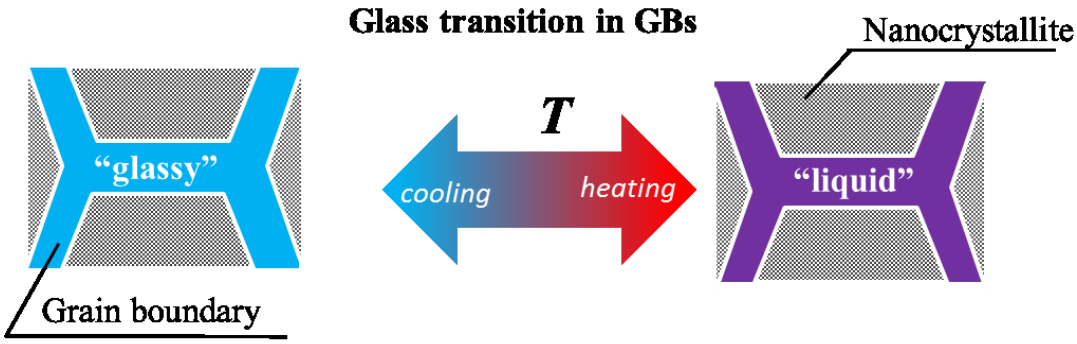

Fig. 4-1-4. Glass transition in grain boundaries of *n*-metals.

4.2 Effect of deposition rate on preferred orientation

For noble metals like Ag and Au, the surface (or interface) energy strongly depends on the plane direction and decreases in the order of the (110), (100) and (111) planes [52]. In the gas deposition method, it is expected that the nanocrystallites with different orientations are deposited on the substrate and a *n*-sample with a fully random texture is formed. However, the prepared *n*-Au and *n*-Ag showed strong (111) preferred orientation where the <111> direction of almost all the grains are normal to substrate. It suggests that the deposited nanocrystallites are rearranged on the sample surface in order to reduce the surface energy by aligning the (111) plane parallel to the surface. At the low deposition rates, the time for rearrangement of the nanocrystallites is enough and the (111) preferred orientation is well developed. So type-L samples show the strong (111) preferred orientation and better thermal stability. In contrast, at the high deposition rates, the rearrangement is impeded by next coming nanocrystallites so that the (111) preferred orientation is not progressed as that at the low deposition rates. The plane direction of some nanocrystallites remained as the deposited state or slightly changed but not fully aligned as the (111) preferred orientation. It is noted that the *n*-Ag sample prepared at the extreme high deposition rate showed the (200) preferred orientation. It is known that Young's modulus of Ag is lowest along the <100> direction and highest along the <111> direction. The competition between the interfacial energy and the strain energy may determine which texture of the (111) or (100) preferred orientations is attained for *n*-Au and *n*-Ag in the gas deposition method.

The annealing behaviors of *n*-Au and *n*-Ag were mentioned in section 3.1 (see Fig. 3-1-6 and Fig. 3-1-10). It is worth noting that the texture of type-L and type-H samples was changed from the (111) preferred orientation to (100) one by annealing. Further, the similar change of preferred orientation was also observed for the sample aged at 260 K (see 3.1.6). Such changes in the preferred orientation were also reported for other *n*-metals. For bulk *n*-Ni alloys (Ni-Fe and Ni-W) prepared by the electrodeposition method, the (111) preferred orientation turned to (100) one by annealing [96].

It was reported that not only the grain boundary migration but also the grain rotation played an important role on the grain growth from the MD simulation of FCC metals [97]. Further, our previous study suggested that the grain rotation was occurred during the creep test without the grain growth [34]. These results support that the grain rotation of the deposited crystallites can be occurred at the surface. The rearrangement process by the grain rotation during the deposition is schematically drawn in Fig. 4-2.

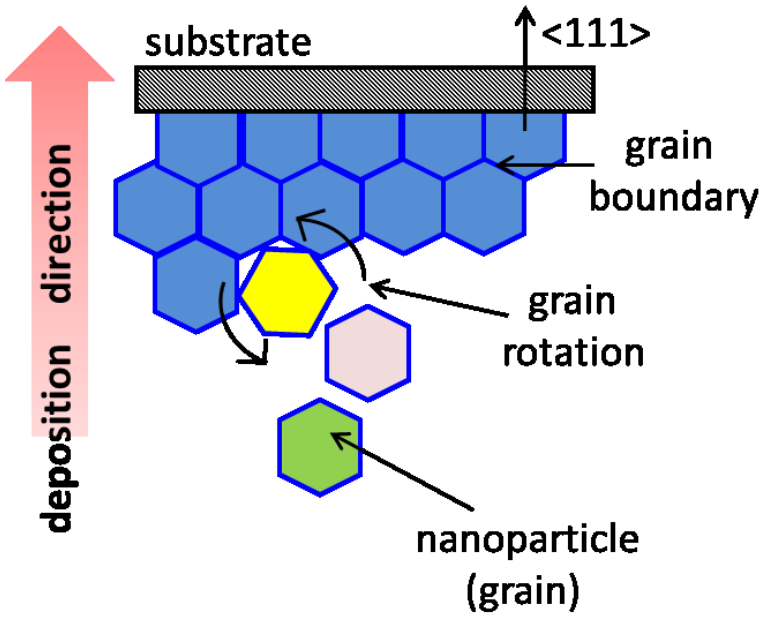

Fig. 4-2. Proposed model for the strong (111) preferred orientation formed by gas deposition method. Nanoparticles with different orientations (indicated as different colors) are deposited on the substrate. The grain deposited on the substrate can rotate as the energy of interface or grain boundaries become lower (in the figure, the (111) preferred orientation is the energetically favorable because of the lowest interface energy of the (111) plane).

4.3 Effect of deposition rate on grain boundary

As mentioned in Chapter. 2, two types of *n*-metal samples were prepared by gas deposition method with controlling the deposition rate. Their differences in various properties were described in Chapter. 3. These observed results are summarized in Table 4-1.

Table. 4-1. Comparison of thermal stability, internal friction and electrical resistivity between type-H and type-L samples.

	***n*-Au**		***n*-Ag**	
	type-H	type-L	type-H	type-L
GB energy	high	low	high	low
Thermal stability	low	high	low	high
internal friction	high	low	high*	low
electrical resistivity	low	high	low	high

*: the value was estimated according to the results of *n*-Au, the exact value was still not clear

The grain boundaries of type-H samples are in the higher energy state compared with those of type-L samples, because type-H samples are thermally unstable relative to type-L samples. It was reported that the grain growth of type-H *n*-Au started at ~350 K while for type-L *n*-Au at ~400 K [51]. Furthermore, the present study suggested that the grain growth of type-H *n*-Ag occurred even at room temperature. One of the grain growth process is the curvature-driven grain boundary migration which is typically occurred for high angle grain boundaries [97] and the excess energy in grain boundary regions is released [98]. For *n*-Au, it was reported that internal friction of type-H showed larger $Q^{-1}_{>200K}$ compared with type-L [37]. It is known that dynamic properties of the grain boundary, like grain boundary sliding, migration and diffusion, strongly depend on the grain boundary energy[30] and the structure (like misorientaiton angle)[99]. Large $Q^{-1}_{>200K}$ reflects that the grain boundaries are energetically unstable. It was reported that the plastic creep responses of *n*-Au were very similar between type-H and type-L, but the steady-state creep rate of type-H was larger than that of type-L compared at the same applied stress [43, 56]. It also support that the grain boundary energy in type-H is higher than that of type-L.

Since the grain boundary energy of type-H is higher than type-L, it is expected that the grain boundaries of type-H are “non-equilibrium” compared with those of type-L; the fraction of high angle grain boundaries and the concentration of the excess free volume are larger. It was reported

that electrical resistivity of ultrafine grained Al fabricated by high-pressure torsion was decreased by annealing. It was attributed to the grain boundaries relaxed from non-equilibrium state to equilibrium state without grain growth, where the resistivity of the non-equilibrium grain boundaries was at least 50% higher than that of thermally equilibrium grain boundaries in *p*-Al [100]. In addition, the electrical resistivity of *n*-Cu decreased by the relaxation of grain boundaries even without grain growth by annealing [90]. However, our results showed a contradiction with these results. In both *n*-Au and *n*-Ag, the electrical resistivity of type-L samples was higher than the value of type-H in spite of that the grain boundaries of type-L is thermally more stable than those of type-H. Most of the grains of *n*-Au and *n*-Ag prepared by the gas deposition method align as the (111) plane parallel to the sample surface (strong (111) preferred orientation). Along the directions of the sample surface, it was reported that the crystallographic direction of the grains was randomly distributed [43]. These observations indicate that the macroscopic electrical resistivity of *n*-Au and *n*-Ag much depends on texture such as the geometrical distribution of the grain boundaries.

It was reported that the geometry (like the plane orientation and mismatch angle) of the grain boundary played an important role on the character [101]. It is known that *n*-Au and *n*-Ag showed the strong (111) preferred orientation. Further, the surface or interface energy of the (111) plane is lowest for these noble metals. When two crystallites jointed on the (111) plane which are mirror images of each other, an energetically stable and coherent (111) twin boundary can be formed. The differences in the thermal stability and the preferred orientations after grain growth between type-L and type-H indicate that thermally stable grain boundaries and the high energy grain boundaries are differently configured in them. To elucidate the different properties observed between type-H and type-L, we propose a model for the geometrical distribution of the grain boundaries as illustrated in Fig. 4-3. For the simplicity, only grains with the <111> direction being normal to the sample surface and those with <100> one are depicted. Fig. 4-3 (a) shows the grain distribution of type-L in the as-prepared state. From the quite strong (111) preferred orientation, the grain boundaries parallel to the sample surface are mainly the energetically stable boundaries like the (111) twin boundary. Due to the sandwiched texture by the stable grain boundaries (as indicated by blue segments in Fig. 4-3(c)), type-L samples show high thermal stability. In contrast, the grain boundaries perpendicular to the sample surface (as indicated by red segments in Fig. 4-3 (c)) are considerably disordered and strained in order to achieve the quite strong (111) preferred orientation. Due to the two-dimensional like structure, type-L showed the normal grain growth as depicted in Fig. 4-3 (e). On the other hand, the (111) preferred orientation of type-H is not as strong as type-L and the crystallites of which (100) plane are parallel to the sample surface are existed (Fig. 4-3 (b)). The configuration of the stable or unstable grain boundaries are rather randomly distributed compared with type-L, as shown in Fig. 4-3 (d). As already mentioned, the rearrangement of the crystallites deposited on the surface is not enough progressed in type-H and the high energy and stable grain boundaries are rather randomly distributed in type-H (Fig. 4-3 (d)).

The crystallites with the <100> orientation are surrounded by the high energy grain boundaries and the preferential grain growth is assisted. Hence type-H showed abnormal grain growth with the (100) preferred orientation as shown in Fig. 4-3 (f).

Most of the grain boundaries perpendicular to the sample surface are high energy ones in type-L (Fig. 4-3 (c)) whereas the high energy and stable grain boundaries are distributed in the case of type-H (Fig. 4-3 (d)). It is expected that the scattering of the electrons passing the specimen length direction is larger for the case of type-L (Fig. 4-3 (c)) than that of type-H (Fig. 4-3 (d)). It is surmised that the higher electric resistivity was observed for type-L samples compared with type-H; the electron scattering is larger due to the anisotropic distribution of the high energy grain boundaries as shown in Fig. 4-3 (c). On the other hand, $Q_{>200K}^{-1}$ observed for type-H was larger than for type-L. The flexural vibration of the ribbon specimen was used for the present measurement and the tensile and compressive stresses were applied along the specimen length direction. It is expected that the sliding motion of grain boundaries are mainly induced along the specimen length direction in this geometry. Since the grain boundaries along the specimen surface in type-L are thermally more stable, smaller grain boundary anelasticity is expected for type-L. In future work, the grain boundaries distribution analysis from EBSD is highly suggested.

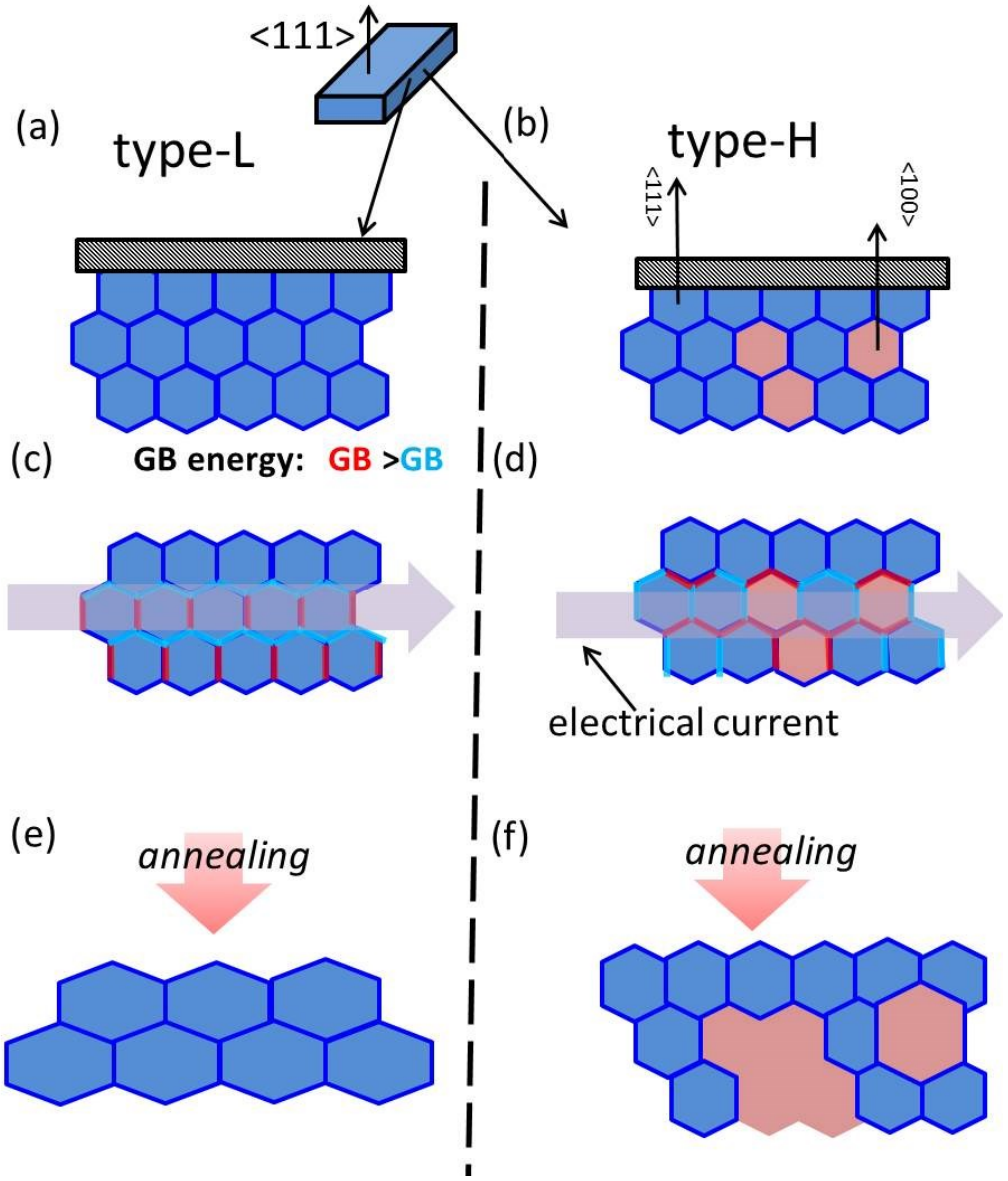

Fig. 4-3. Proposed model for the distributions of the grains and grain boundaries in (a) type-L and (b) type-H samples. The grains of which the <111> orientation is normal to the sample surface are indicated in blue and <100> ones in red. In the figures, high energy grain boundaries are indicated by red segments and low energy grain boundaries are indicated by blue segments. Changes in texture of type-L and type-H by annealing are shown in (e) and (f), respectively. The mauve arrows in the middle panel indicate the direction of the current at the electrical resistivity measurement.

4.4 Effect of deposition rate on crystallite

N-materials can be regarded as nanocrystallites adhered by the grain boundaries. As mentioned in previous section 4.1, the grain boundaries of *n*-Au and *n*-Ag show glass transition like behavior below 200 K. Further, the geometrical distribution of the high energy and stable grain boundaries is different between type-L and type-H, and it is governed by the deposition rate. Most researches paid attentions to the behaviors of the grain boundaries but not so much to the state of the crystallites. However, if the glass-transition like behavior is thermally induced at the grain boundaries, some changes are induced in the crystalline state of the grains. We revisit the results of the low temperature XRD measurement (see section 3.1.7) to pursue the influence of the change in the grain boundary state on the grains.

As mentioned in 3.1.7, the lattice parameters of *n*-Au and *n*-Ag showed monotonous temperature increases with increasing temperature for both type-L and type-H, and no anomaly was observed in the temperature range 100-200 K where the characteristic changes were observed in anelastic, thermal and electrical properties. However, the temperature coefficient of the lattice parameter was slightly smaller for type-H samples than for type-L samples. The lattice parameters of both type-L and type-H were smaller by ~0.01% than that of *p*-counterpart at room temperature. At around 40 K, the lattice parameter of type-L was smaller by ~0.01% than that of *p*-counterpart while that of type-H was almost same to the value of *p*-counterpart. These temperature changes in the lattice parameters are simplified and summarized in Fig. 4-4-1.

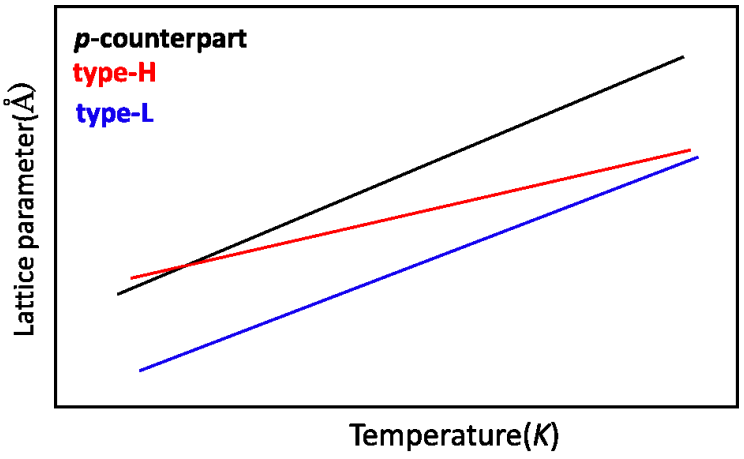

Fig. 4-4-1. Simplified temperature dependence in lattice parameter of *n*-metals (red line for type-H, blue line for type-L and black line for *p*-counterpart).

It was reported that the thermal expansion at the grain boundary regions was about 4 times larger than that of the grains [4]. The thermal expansion coefficient larger than *p*-counterpart was reported for *n*-BN [16] and *n*-Fe [17]. It was indicated that the vibrational kinetic energy of atoms at the grain boundaries was higher than that of the crystallite atoms. Since the energy state of the grain boundaries is higher for type-H than for type-L, the grain boundaries of type-H are expected

to have higher vibrational kinetic energy. However, type-H showed the thermal expansion coefficient lower than that of type-L or *p*-counterpart.

On the other hand, it was reported that lattice expansion was observed in the *n*-materials prepared in non-equilibrium method; the lattice expansion was attributed to the stress field induced by excess free-volume in non-equilibrium grain boundaries [57]. As already mentioned, the grain boundaries of type-H is in more "non-equilibrium" state than that of type-L. The non-equilibrium state of grain boundary was related with the excess free-volume and became more energetically unstable with the increase in the fraction of free-volume [102]. If grain boundaries of type-H contained more excess free-volume than those of type-L, the temperature change of lattice parameter of type-H is relatively smaller than type-L just like our results. Lattice parameter of type-H increased with decreasing the temperature, indicating that excess free-volume increased correspondingly. The vacancy-type defects in crystallite may play a role as "source" of the excess free-volume of grain boundaries: the vacancy-type defect migrated from crystallite to grain boundaries. However, it was hard to explain the reproducibility of the lattice parameter by warm-up and cool-down, because the migration of vacancy-type defects between grain boundaries and crystallite was not reversible.

For another possibility, the smaller thermal expansion of type-H may suggest a change in the atomic potential from the *p*-counterpart. The potential energy curves for type-H and *p*-counterpart are illustrated in Fig. 4-4-2 to explain the change in the thermal expansion. If the curvature near the potential minimum becomes shaper (red curve), the increase in mean distance by thermal agitation is smaller. It was reported that the lattice variation in the n-materials was affected by the processing method [57]. As shown in Fig. 4-4-2, the behavior of the temperature change in lattice parameter is different by the deposition rate for *n*-Ag and *n*-Au. However, the details of the effect of deposition rate on the lattice parameter and its temperature change are still not clarified and further investigations are needed.

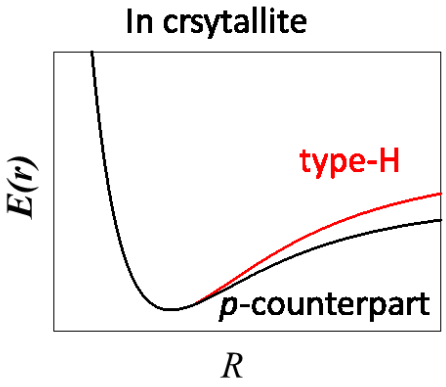

Fig. 4-4-2. Change in potential energy curve to explain the decrease in the thermal expansion.

Chapter 5 Conclusion

High density and high purity *n*-Au and *n*-Ag were prepared by the gas deposition method and the anelastic, electrical and thermal properties were measured to characterize the intrinsic behavior of *n*-metals. A rapid increase in internal friction, an excess endothermic heat flow and a decrease in electrical resistivity were observed below room temperature for both *n*-Au and *n*-Ag. These characteristics changes were similarly observed for repetition of the cool-down and warm-up measurements below room temperature. These changes were quite similar to those reported for metallic glasses at glass transition temperature. It is indicated that the glass transition like behavior is thermally activated in the grain boundaries of FCC *n*-metals. Our observed results support the glass-like behaviors of grain boundaries reported from computer simulations.

N-Au and *n*-Ag prepared by the gas deposition method exhibited slight different properties and texture and they were divided into two types by the deposition rate of nanoparticles; type-L and type-H prepared at the lower and higher deposition rates, respectively. For example, type-L *n*-metals showed the stronger (111) preferred orientation and higher thermal stability compared with type-H. It is suggested that the geometrical distribution of high energy and low energy (or thermally unstable and stable) grain boundaries are different between type-L and type-H resulted in the slight different texture and properties. Further, the origin of the difference in texture is attributed to the relaxation process of the nanoparticles at the deposition. The relaxation does not well proceed at the high deposition rate. Hence, relatively high energy or thermally unstable state is attained in type-H compared with type-L.

The results of the present study indicate that the grain boundaries of *n*-metals are not same as those of *p*-counterparts and the *n*-metals can possess characteristic properties owing to the unique grain boundary behaviors different from *p*-counterparts.

References

[1] D. Prokoshkina, V.A. Esin, G. Wilde, S.V. Divinski, Grain boundary width, energy and self-diffusion in nickel: Effect of material purity, Acta Mater. 61(14) (2013) 5188-5197.

[2] M.A. Tschopp, H.A. Murdoch, L.J. Kecskes, K.A. Darling, "Bulk" Nanocrystalline Metals: Review of the Current State of the Art and Future Opportunities for Copper and Copper Alloys, JOM 66(6) (2014) 1000-1019.

[3] E.N. Hahn, M.A. Meyers, Grain-size dependent mechanical behavior of nanocrystalline metals, Materials Science and Engineering: A 646 (2015) 101-134.

[4] H. Gleiter, Nanocrystalline materials, Prog. Mater Sci. 33(4) (1989) 223-315.

[5] M.A. Meyers, A. Mishra, D.J. Benson, Mechanical properties of nanocrystalline materials, Prog. Mater Sci. 51(4) (2006) 427-556.

[6] G.W. Nieman, J.R. Weertman, R.W. Siegel, Microhardness of nanocrystalline palladium and copper produced by inert-gas condensation, Scripta Metallurgica 23(12) (1989) 2013-2018.

[7] J.R. Weertman, Hall-Petch strengthening in nanocrystalline metals, Materials Science and Engineering: A 166(1) (1993) 161-167.

[8] S.Takeuchi, THE MECHANISM OF THE INVERSE HALL-PETCH RELATION OF NANOCRYSTALS, Scripta Mater. 44(8-9) (2001) 1483-1487.

[9] J. Sheng, G. Rane, U. Welzel, E.J. Mittemeijer, The lattice parameter of nanocrystalline Ni as function of crystallite size, Physica E: Low-dimensional Systems and Nanostructures 43(6) (2011) 1155-1161.

[10] R.Z. Valiev, R.K. Islamgaliev, I.V. Alexandrov, Bulk nanostructured materials from severe plastic deformation, Prog. Mater Sci. 45(2) (2000) 103-189.

[11] G.J. Tucker, D.L. McDowell, Non-equilibrium grain boundary structure and inelastic deformation using atomistic simulations, Int. J. Plast. 27(6) (2011) 841-857.

[12] G.A. Vetterick, J. Gruber, P.K. Suri, J.K. Baldwin, M.A. Kirk, P. Baldo, Y.Q. Wang, A. Misra, G.J. Tucker, M.L. Taheri, Achieving Radiation Tolerance through Non-Equilibrium Grain Boundary Structures, Sci Rep 7(1) (2017) 12275.

[13] K. Lu, Nanocrystalline metals crystallized from amorphous solids: Nanocrystallization, structure, and properties, Mat Sci Eng R 16(4) (1996) 161-221.

[14] S.A.M. Al-Bat'hi, Electrodeposition of Nanostructure Materials, in: M. Aliofkhazraei (Ed.), Electroplating of Nanostructures, InTech, Rijeka, 2015, pp. 3-25.

[15] L. Lu, Y. Shen, X. Chen, L. Qian, K. Lu, Ultrahigh Strength and High Electrical Conductivity in Copper, Science 304(5669) (2004) 422-426.

[16] P. Lejček, Grain Boundaries: Description, Structure and Thermodynamics, Grain Boundary Segregation in Metals, Springer Berlin Heidelberg, Berlin, Heidelberg, 2010, pp. 5-24.

[17] S.R. Phillpot, D. Wolf, H. Gleiter, A Structural Model for Grain-Boundaries in Nanocrystalline Materials, Scripta Metallurgica Et Materialia 33(8) (1995) 1245-1251.

[18] K. Inoue, M. Saito, C. Chen, M. Kotani, Y. Ikuhara, Mathematical analysis and STEM observations

of arrangement of structural units in <001> symmetrical tilt grain boundaries, Microscopy (Oxf) 65(6) (2016) 479-487.
[19] K. Inoue, B. Feng, N. Shibata, M. Kotani, Y. Ikuhara, Structure of <110>-tilt boundaries in cubic zirconia, Journal of Materials Science 52(8) (2017) 4278-4287.
[20] J. Han, V. Vitek, D.J. Srolovitz, The grain-boundary structural unit model redux, Acta Mater. 133 (2017) 186-199.
[21] 井上和俊, 斎藤光浩, 小谷元子, 幾原雄一, 整数論的手法による粒界原子構造予測, まてりあ 56(10) (2017) 589-596.
[22] P.R.M. van Beers, V.G. Kouznetsova, M.G.D. Geers, M.A. Tschopp, D.L. McDowell, A multiscale model of grain boundary structure and energy: From atomistics to a continuum description, Acta Mater. 82 (2015) 513-529.
[23] K. Lu, Stabilizing nanostructures in metals using grain and twin boundary architectures, Nat Rev Mater 1(5) (2016) 16019.
[24] H. Zhang, D.J. Srolovitz, J.F. Douglas, J.A. Warren, Grain boundaries exhibit the dynamics of glass-forming liquids, Proc Natl Acad Sci U S A 106(19) (2009) 7735-40.
[25] 八木信頼, “面心立方金属ナノ結晶の変形機構と結晶粒界層の研究”, 博士論文, 筑波大学, 2007.
[26] M. Tang, W.C. Carter, R.M. Cannon, Grain boundary order-disorder transitions, Journal of Materials Science 41(23) (2006) 7691-7695.
[27] T. Frolov, D.L. Olmsted, M. Asta, Y. Mishin, Structural phase transformations in metallic grain boundaries, Nature Communications 4 (2013) 1899.
[28] P. Keblinski, S.R. Phillpot, D. Wolf, H. Gleiter, Thermodynamic Criterion for the Stability of Amorphous Intergranular Films in Covalent Materials, Phys. Rev. Lett. 77(14) (1996) 2965-2968.
[29] P. Keblinski, S.R. Phillpot, D. Wolf, H. Gleiter, Amorphous structure of grain boundaries and grain junctions in nanocrystalline silicon by molecular-dynamics simulation, Acta Mater. 45(3) (1997) 987-998.
[30] D. Wolf, High-temperature structure and properties of grain boundaries: long-range vs. short-range structural effects, Curr. Opin. Solid State Mater. Sci. 5(5) (2001) 435-443.
[31] K.H. Nagamanasa, S. Gokhale, R. Ganapathy, A.K. Sood, Confined glassy dynamics at grain boundaries in colloidal crystals, Proc Natl Acad Sci U S A 108(28) (2011) 11323-6.
[32] T. Watanabe, Grain boundary engineering: historical perspective and future prospects, Journal of Materials Science 46(12) (2011) 4095-4115.
[33] J. Hu, Y.N. Shi, X. Sauvage, G. Sha, K. Lu, Grain boundary stability governs hardening and softening in extremely fine nanograined metals, Science 355(6331) (2017) 1292-1296.
[34] N. Yagi, A. Rikukawa, H. Mizubayashi, H. Tanimoto, Experimental tests of the elementary mechanism responsible for creep deformation in nanocrystalline gold, Physical Review B 74(14) (2006) 144105.
[35] R.L. Coble, A Model for Boundary Diffusion Controlled Creep in Polycrystalline Materials, J. Appl. Phys. 34(6) (1963) 1679-1682.
[36] T.S. Ke, Experimental Evidence of the Viscous Behavior of Grain Boundaries in Metals, Physical Review 71(8) (1947) 533-546.

[37] H. Tanimoto, S. Sakai, H. Mizubayashi, Anelasticity of nanocrystalline metals, Materials Science and Engineering: A 370(1–2) (2004) 135-141.
[38] S. Sakai, H. Tanimoto, H. Mizubayashi, Mechanical behavior of high-density nanocrystalline gold prepared by gas deposition method, Acta Mater. 47(1) (1998) 211-217.
[39] H. Tanimoto, K. Mutou, Y. Hosonuma, K. Yamamoto, H. Mizubayashi, Anelasticity study on interfaces of nanocrystalline Au and nanoporous Au, Materials Science and Engineering: A 521-522 (2009) 295-298.
[40] H. Tanimoto, Mechanical Spectroscopy of Nanocrystalline Metals and Nanometer-Thick Films: Characteristic Properties Originated in Nanostructures, Solid State Phenomena 184 (2012) 42-51.
[41] P.R. Cantwell, M. Tang, S.J. Dillon, J. Luo, G.S. Rohrer, M.P. Harmer, Grain boundary complexions, Acta Mater. 62 (2014) 1-48.
[42] 8 - Thermochemical data A2 - Gale, W.F, in: T.C. Totemeier (Ed.), Smithells Metals Reference Book (Eighth Edition), Butterworth-Heinemann, Oxford, 2004, pp. 8-1-8-58.
[43] 境誠司, "高密度金ナノ結晶の物性評価"　博士論文, 筑波大学, 2001.
[44] M. Grewer, J. Markmann, R. Karos, W. Arnold, R. Birringer, Shear softening of grain boundaries in nanocrystalline Pd, Acta Mater. 59(4) (2011) 1523-1529.
[45] H.P. Klug, L.E. Alexander, X-Ray Diffraction Procedures: For Polycrystalline and Amorphous Materials, 2nd ed., Wiley, New York, 1974.
[46] N.C. Halder, C.N.J. Wagner, Separation of particle size and lattice strain in integral breadth measurements, Acta Crystallographica 20(2) (1966) 312-313.
[47] 理科年表　平成 20 年,　丸善株式会社,　国立天文台　編.
[48] "転位論: その金属学への応用",日本金属学会, 丸善(東京)1971.
[49] M. S.Blanter., I. S.Golovin., H. Neuhäuser., H.-R. Sinning., Introduction to Internal Friction: Terms and Definitions, Internal Friction in Metallic Materials: A Handbook, Springer Berlin Heidelberg, Berlin, Heidelberg, 2007, pp. 1-10.
[50] J.D. Hanawalt, H.W. Rinn, L.K. Frevel, Chemical analysis by x-ray diffraction - Classification and use of x-ray diffraction patterns, Industrial and Engineering Chemistry-Analytical Edition 10(9) (1938) 0457-0512.
[51] S. Sakai, H. Tanimoto, K. Otsuka, T. Yamada, Y. Koda, E. Kita, H. Mizubayashi, Elastic behaviors of high density nanocrystalline gold prepared by gas deposition method, Scripta Mater. 45(11) (2001) 1313-1319.
[52] H.L. Skriver, N.M. Rosengaard, Surface energy and work function of elemental metals, Physical Review B 46(11) (1992) 7157-7168.
[53] J. Xu, J.S. Yin, E. Ma, Nanocrystalline Ag formed by low-temperature high-energy mechanical attrition, Nanostruct. Mater. 8(1) (1997) 91-100.
[54] Y.Z. Wang, P. Cui, X.J. Wu, J.B. Huang, B. Cai, Internal Friction of Nanocrystalline Silver, physica status solidi (a) 186(1) (2001) 99-104.
[55] H. Gleiter, Nanostructured materials: Basic concepts and microstructure, Acta Mater. 48(1) (2000) 1-29.

[56] S. Sakai, H. Tanimoto, E. Kita, H. Mizubayashi, Characteristic creep behavior of nanocrystalline metals found for high-density gold, Physical Review B 66(21) (2002) 214106.
[57] G.K. Rane, U. Welzel, S.R. Meka, E.J. Mittemeijer, Non-monotonic lattice parameter variation with crystallite size in nanocrystalline solids, Acta Mater. 61(12) (2013) 4524-4533.
[58] R. Birringer, M. Hoffmann, P. Zimmer, Interface stress in polycrystalline materials: the case of nanocrystalline Pd, Phys. Rev. Lett. 88(20) (2002) 206104.
[59] A.K. Srivastav, N. Chawake, B.S. Murty, Grain-size-dependent non-monotonic lattice parameter variation in nanocrystalline W: The role of non-equilibrium grain boundary structure, Scripta Mater. 98 (2015) 20-23.
[60] W. Hertz, W. Waidelich, H. Peisl, Lattice contraction due to quenching in vacancies in platinum and gold, Phys. Lett. A 43(3) (1973) 289-290.
[61] H. Tanimoto, S. Sakai, E. Kita, H. Mizubayashi, Characterization and Determination of Elastic Property of High-Density Nanocrystalline Gold Prepared by Gas-Deposition Method, MATERIALS TRANSACTIONS 44(1) (2003) 94-103.
[62] Y. Fukai, H. Sugimoto, Formation mechanism of defect metal hydrides containing superabundant vacancies, J. Phys.: Condens. Matter 19(43) (2007) 436201.
[63] P.A. Korzhavyi, I.A. Abrikosov, B. Johansson, A.V. Ruban, H.L. Skriver, First-principles calculations of the vacancy formation energy in transition and noble metals, Physical Review B 59(18) (1999) 11693-11703.
[64] J. Crank, The mathematics of diffusion, Clarendon Press1975.
[65] Landolt-Börnstein, Numerical Data and Functional Relationships in Science and Technology, New Series, Group III: Crystal and Solid State Physics Atomic Defects in Metals, Edited by H. Ullmaier (Springer-Verlag, 1991) Vol. 25 p. 224-228.
[66] A. Seeger, H. Mehrer, Interpretation of Self-Diffusion and Vacancy Properties in Gold, physica status solidi (b) 29(1) (1968) 231-243.
[67] M. Ames, J. Markmann, R. Karos, A. Michels, A. Tschöpe, R. Birringer, Unraveling the nature of room temperature grain growth in nanocrystalline materials, Acta Mater. 56(16) (2008) 4255-4266.
[68] K. Pantleon, M.A.J. Somers, Interpretation of microstructure evolution during self-annealing and thermal annealing of nanocrystalline electrodeposits—A comparative study, Materials Science and Engineering: A 528(1) (2010) 65-71.
[69] S. Pearson, L. Rotherham, Internal Friction and Grain Boundary Viscosity of Silver and Binary Silver Solid Solutions, T Am I Min Met Eng 206(8) (1956) 894-901.
[70] K-H.Hellweg, eds. Landolt-Bornstein, numerical data and functional relationships in Science and technology. Vol.11.Springer-verlag; 1979.p.11.
[71] T. Xi, T. Sato, R. Suzuki, H. Tanimoto, Glass-Transition-Like Behavior of Grain Boundaries in Nanocrystalline Gold, Materials Transactions 59(1) (2018) 47-52.
[72] N. Yagi, A. Ueki, H. Mizubayashi, H. Tanimoto, Anelasticity in FCC Nanocrystalline Metals, Journal of Metastable and Nanocrystalline Materials 24-25 (2005) 503-506.
[73] Y. Kabe, H. Tanimoto, H. Mizubayashi, Elasticity Study of Nanostructured Al and Al-Si(Cu) Films,

MATERIALS TRANSACTIONS 45(1) (2004) 119-124.
[74] H. Mizubayashi, J. Matsuno, H. Tanimoto, Young's modulus of silver films, Scripta Mater. 41(4) (1999) 443-448.
[75] A.S. Nowick, B.S. Berry, Anelastic relaxation in crystalline solids, Academic Press, New York, 1972.
[76] T.S. Ke, Stress Relaxation across Grain Boundaries in Metals, Physical Review 72(1) (1947) 41-46.
[77] A.K. Maier, D. Mari, I. Tkalcec, R. Schaller, GRAIN BOUNDARY RELAXATION IN Bi-CRYSTALS: MECHANICAL SPECTROSCOPY AND MOLECULAR DYNAMICS SIMULATIONS, Archives Of Metallurgy And Materials 60(1) (2015) 377-380.
[78] A.-K. Maier, D. Mari, I. Tkalcec, R. Schaller, Theoretical modelling of grain boundary anelastic relaxations, Acta Mater. 74 (2014) 132-140.
[79] 鈴木孝侑, "金ナノ結晶材料の特異物性と粒界・粒内状態" 修士論文, 筑波大学, 2015, pp. 1-50.
[80] I. Kaur, W. Gust, 12.2.1 Grain boundary self-diffusion in pure materials, in: H. Mehrer (Ed.), Diffusion in Solid Metals and Alloys, Springer Berlin Heidelberg, Berlin, Heidelberg, 1990, pp. 640-646.
[81] G. Fantozzi, C. Esnouf, W. Benoit, I.G. Ritchie, Internal friction and microdeformation due to the intrinsic properties of dislocations: The Bordoni relaxation, Prog. Mater Sci. 27(3) (1982) 311-451.
[82] S. Ichikawa, K.i. Miyazawa, H. Ichinose, K. Ito, The microstructure of deformed nanocrystalline Ag and Ag/Fe alloy, Nanostruct. Mater. 11(8) (1999) 1301-1311.
[83] X.-L. Wu, E. Ma, Dislocations in nanocrystalline grains, Appl. Phys. Lett. 88(23) (2006) 231911.
[84] J. Rupp, R. Birringer, Enhanced specific-heat-capacity (Cp) measurements (150-300 K) of nanometer-sized crystalline materials, Physical Review B 36(15) (1987) 7888-7890.
[85] O. Haruyama, H. Kimura, N. Nishiyama, A. Inoue, Behavior of electrical resistivity through glass transition in Pd40Cu30Ni10P20 metallic glass, Materials Science and Engineering: A 304–306 (2001) 740-742.
[86] D.R. Lide, CRC Handbook of Chemistry and Physics, 84th Edition, Taylor & Francis2003.
[87] J. Ederth, L.B. Kish, E. Olsson, C.G. Granqvist, Temperature dependent electrical resistivity in nanocrystalline gold films made by advanced gas deposition, J. Appl. Phys. 88(11) (2000) 6578-6582.
[88] H. Zeng, Y. Wu, J. Zhang, C. Kuang, M. Yue, S. Zhou, Grain size-dependent electrical resistivity of bulk nanocrystalline Gd metals, Progress in Natural Science: Materials International 23(1) (2013) 18-22.
[89] キッテル固体物理学入門第 8 版, 丸善 2005.
[90] L.H. Qian, Q.H. Lu, W.J. Kong, K. Lu, Electrical resistivity of fully-relaxed grain boundaries in nanocrystalline Cu, Scripta Mater. 50(11) (2004) 1407-1411.
[91] J. Guo, F. Zu, Z. Chen, S. Zheng, Y. Yuan, Exploration of a new method in determining the glass transition temperature of BMGs by electrical resistivity, Solid State Commun. 135(1) (2005) 103-107.
[92] D.P. Aji, G.P. Johari, Effects of configurational changes on electrical resistivity during glass-liquid transition of two bulk metal-alloy glasses, J. Chem. Phys. 141(22) (2014) 224508.
[93] L.-f. Wang, Q.-d. Zhang, Z.-y. Huang, X. Cui, F.-q. Zu, Study of the mechanism of the internal friction peak in a Cu36Zr48Al8Ag8 bulk metallic glass, J. Non-Cryst. Solids 406 (2014) 127-132.
[94] Anelastic Relaxation Mechanisms of Internal Friction, in: M.S. Blanter, I.S. Golovin, H. Neuhäuser, H.-R. Sinning (Eds.), Internal Friction in Metallic Materials: A Handbook, Springer Berlin Heidelberg,

Berlin, Heidelberg, 2007, pp. 11-119.
[95] P. Keblinski, D. Wolf, S.R. Phillpot, H. Gleiter, Self-diffusion in high-angle fcc metal grain boundaries by molecular dynamics simulation, Philos. Mag. A 79(11) (1999) 2735-2761.
[96] I. Matsui, M. Kanetake, H. Mori, Y. Takigawa, K. Higashi, Relationship between grain boundary relaxation strengthening and orientation in electrodeposited bulk nanocrystalline Ni alloys, Mater. Lett. 205 (2017) 211-214.
[97] A.J. Haslam, S.R. Phillpot, D. Wolf, D. Moldovan, H. Gleiter, Mechanisms of grain growth in nanocrystalline fcc metals by molecular-dynamics simulation, Materials Science and Engineering: A 318(1) (2001) 293-312.
[98] G.S. Rohrer, Grain boundary energy anisotropy: a review, Journal of Materials Science 46(18) (2011) 5881-5895.
[99] M. Yuasa, Y. Chino, M. Mabuchi, Molecular dynamics and first-principles study of grain boundary sliding in metals, Transactions of the Materials Research Society of Japan 39(1) (2014) 31-34.
[100] T.S. Orlova, A.M. Mavlyutov, A.S. Bondarenko, I.A. Kasatkin, M.Y. Murashkin, R.Z. Valiev, Influence of grain boundary state on electrical resistivity of ultrafine grained aluminium, Philosophical Magazine 96(23) (2016) 2429-2444.
[101] E.R. Homer, S. Patala, J.L. Priedeman, Grain Boundary Plane Orientation Fundamental Zones and Structure-Property Relationships, Scientific Reports 5 (2015) 15476.
[102] T. Uesugi, K. Higashi, First-principles calculation of grain boundary energy and grain boundary excess free volume in aluminum: role of grain boundary elastic energy, Journal of Materials Science 46(12) (2011) 4199-4205.

Acknowledgements

First and foremost, I would like to express my sincere gratitude to my supervisor Associate Professor Dr. Hisanori Tanimoto for his excellent guidance and encouragement during this 3 years study. Prof. Tanimoto is my favorite and respected professor. His endless enthusiasm and attitude towards science has inspired me a lot in doing research. His optimism and kindness towards life always encouraged and warmed me when I am confused or lack of confidence. I deeply appreciated all his contribution of time, advice and concern of me.

I am grateful to the members of my thesis committee: Professor Hee Young Kim (University of Tsukuba), Professor Eiji Kita (President of National Institute of Technology, Ibaraki College) and Associate Professor Tamotsu Koyano (University of Tsukuba). Thank for their beneficial suggestion helped me improved my thesis and presentation. Especially, I would like to thank Professor Eiji Kita for offering suggestions about gas deposition equipment.

I would like to thank Honorary Professor H. Mizubayashi (University of Tsukuba) for his valuable discussion, Professor S.Kuroda (University of Tsukuba) for electrical resistivity measurement, Professor S. Muto (Nagoya University) for electron microscope, Professor R.Kumai and Associate Professor H.Sagayama (KEK) for the low temperature XRD measurement, OPEN FACILITY (University of Tsukuba) for the DSC measurement and Cryogenics Division (University of Tsukuba) for offering the liquid He and liquid N_2 for experiments.

I would also like to thank every member in Tanimoto Lab for their kindness and accompany during my stay at Lab. As the only foreign student in the Lab, they are being very patient and kind. I learned a lot of Japanese and Japanese culture by talking with them. Especially, I would like to thank my research partners: Mr. Sato, Mr. Suzuki and Mr. Karube. I would like to thank Mr. Hashiguchi, who is same grade with me, the many days and nights we prepared PhD thesis together in Lab would be a precious memory for us.

Last but not the least, I would like to express my deep love to my dear family. Thank for all their great support and encouragement. My parents who maybe don't know better the difficulty of pursuing a PhD, but they gave me all their best support, encouragement and love in every stage of my study and life. I deeply appreciated my loving wife for her strong support and help during my every stage of this PhD.

Terigele Xi, February 2018

List of publications & Presentations

Publications:

1. Terigele Xi、Takahiro Sato、Ryoma Suzuki、Hisanori Tanimoto
   Glass-Transition-Like Behavior of Grain Boundaries in Nanocrsytalline Gold
   Materials Transactions vol.59(2018), No.1. pp.47-52.

2. Terigele Xi, Ryoma Suzuki and Hisanori Tanimoto
   Low-temperature anelastic property of nanocrystalline Ag fabricated by gas deposition method
   Materials Research (proceedings paper for ICIFMS-18), submitted

Oral presentations:

1. ○ Terigele Xi、Ryoma Suzuki、Hisanori Tanimoto
   Low-Temperature Anelastic Property of Nanocrystalline Ag Fabricated by Gas Deposition Method, 18th. International Conference on Internal Friction and Mechanical Spectroscopy (September 15, 2017. Foz do Iguaçu, Brazil)
2. ○ 席特日格楽、鈴木竜馬、谷本久典、水林博
   金及び銀ナノ結晶材の物性・粒界状態に及ぼす超微粒子堆積速度の影響
   日本金属学会秋期講演大会（2017 年 9 月 7 日、北海道大学）
3. ○ 席特日格楽、鈴木竜馬、谷本久典、水林博
   Characteristic Low-Temperature Properties of Nanocrystalline Ag Fabricated by Gas Deposition Method
   日本金属学会春期講演会（2017 年 3 月 15 日、首都大学東京南大沢キャンパス）
4. ○席特日格楽、鈴木竜馬、谷本久典、水林博
   Characteristic Low-Temperature Properties of Nanocrystalline Au and Abundant Vacancy-Type Defects
   日本金属学会秋期講演大会（2016 年 9 月 21 日、大阪大学豊中キャンパズ）
5. ○ Xi Terigele、Hisanori TANIMOTO、Takahiro SATO、Hiroshi MIZUBAYASHI
   Lattice Contraction of Nanocrystalline Au and Rapid Increase in Internal Friction above 200K
   日本金属学会春期講演会（2016 年 3 月 24 日、東京理科大学葛飾キャンパス）
6. ○佐藤隆洋、席特日格楽、谷本久典、水林博、熊井玲児、佐賀山基
   金ナノ結晶材の格子定数の低温温度変化と結晶子・粒界状態
   日本金属学会秋期講演大会（2015 年 9 月 16 日、九州大学）

○ for presenter